# Light Matter Interaction in Epsilon Near Zero Metal/Insulator Layered Nanocavities

Thesis by

**Milan Palei**

In Partial Fulfillment of the Requirements
for the Degree of
Doctor of Philosophy


Istituto Italiano di Tecnologia (IIT), Genova

UNIVERSITÀ DEGLI STUDI
DI GENOVA

Dipartimento di Chimica e Chimica Industriale (DCCI),
Universita Degli Studi Di Genova, Genova

2019

Supervised By:
Prof. Roman Krahne, Dr. Vincenzo Caligiuri, Dr. Stefan Kudera (IIT Genova)
Prof. Francesco Buatier de Mongeot (Dipartimento di Fisica, Universita Degli Studi Di Genova)

Dedicated to my parents
Mr. Kamalakanta Palei and Mrs. Bharati Bag,
who gave me confidence and supported me in my difficult phase of life
and my brother Dr. Shubhendu Palei,
who nurtured my interest in science
and guided me all along the way….

## Acknowledgement

The completion of this thesis wouldn't have been possible without support of many people. Among them, first I would like to thank my advisor Professor Roman Krahne, for his constant support all through my PhD. Three years for a PhD is never enough to achieve the target one set for in the beginning. His constant feedback and guidance made it possible to accomplish the target. Roman has been an astounding mentor, constantly challenging me and at the same time bringing up my scientific temper for which I will be ever grateful.

I have also been very fortunate to have co-tutors without whom I wouldn't able to complete my study. Dr. Stefan Kudera was co-tutoring me during first year of my PhD. Stefan has been very supportive and shared his experience on functionalizing colloidal nanocrystal which are basis for the work in chapter 8. Dr. Vincenzo Caligiuri, who has been co-tutoring me for last two years has been very supportive. Together with Vincenzo we started exploring the artificially engineer epsilon near zero nanocavities and investigate rich physics involved in it. Vincenzo's experience with spectroscopic ellipsometry and fluorescence spectroscopy has been very precious to solve many crucial problems. I am very thankful to him. I am also thankful to my co-advisor Professor Francesco Buatier de Mongeot from the Physics Department, University of Genoa. I had so many fruitful scientific discussions with Prof. Buatier. The results presented in chapter xx are the outcome of collaboration with the Buatier group. The Optoelectronics group has been very supportive and encouraging from very beginning of my PhD. Dr. Prachi Rastogi, who was my former colleague helped me by providing CdSe/CdS DIR samples, which has been used for investigating optical properties in ALD coated NCs film reported in chapter 8. I am obliged to my former colleague Dr. Mario Miscuglio. Mario has been very helpful by troubleshooting many of my problems related to nanofabrication and devices. I have learnt many things from him both related to my work as well as personal life. I also like to thank Dr. Davide Spirito, postdoc in our group who helped me to build optical set up and troubleshooting the problems. I am sincerely thankful to Dr. Sedat Dogan who was Post Doc in our group. Sedat had been very supportive and joyful individual to work with. I would also like to thank my lab mate Giulia Biffi and Fang Chen for their cooperation.

My PhD work wouldn't have been completed without support from technical support staff. I am specially obliged to the cleanroom staff Marco Leoncini, Fabio Moia, Eliana Rondanina and Alessandro Bosca. I am also grateful to Nanochemistry laboratory technical staff Gabriele La Rosa, Francesco De Donato, Simone Nitti, Gianmarino Pugliese. I do like to specially thank Marco Scotto for technically assisting me in training and helping me out whenever there was a need in the lab.

I have been honored to get opportunity to work in Molecular foundry, Berkeley Labs in summer 2018. I am especially thankful to Adam Schwartzberg for helping me with ALD and in-situ ellipsometry. I am also thankful to Alexander Weber-Bargioni, Edward Barnard, Stefano Cabrini and Tina McCoy for their help and support during my stay in Foundry.

At IIT, I had chance to interact with so many people including graduate students, Post Doc, Researcher, Team Leader and administrative staff. It has been a great learning from all of them. I would like to thank Liberato Manna, director of Nanochemistry facility for his excellent support. I would like to acknowledge Dipak Shinde, Nimai Mishra, Anitha Eswari, Zhiya Dang, Milena Arciniegas, Ahmed Abdelhady, Ali Hossain Khan, Jaya Kumar Panda, Sanjay Thorat, Muhammad Imran, Nikhil Puthiya for their scientific collaboration and useful discussion. I would also like to thank Beatriz Martin-Garcia for her unconditional help both in lab and as a friend.

My office mates and friends here in IIT have been really amazing. When I joined first time to IIT, Sandeep Keshavan, Subramanyam Goripati, Shovan Naskar made me feel welcome and always available for a chat or any other discussion. Subramanyam has been a constant source of inspiration and play a role like a big brother so far. I would also like to acknowledge my friend Waseem Raja, Abdul Basit, Preethi Bala Balakrishanan, Asmita Chavan, Vincenzo Aglieri for their help. My office mate Andrea Barbaglia, Helena Gavilan Rubio have been really nice and can't forget those long evening spent together in office and lab. I am also grateful to my previous flat mates Zeeshan Hamid (for Long discussion on political agenda) and Nityanand Bolshette (for making food ready especially when I am hungry and reached home at midnight from Lab).

I am also grateful to all the administrative staff who has made things easier for me. Specially I would like to thank Iulia Manolache Orlatan for her immense help in dealing with all kind of paper work. Anna Barbino from DCCI, University of Genoa has been very helpful regarding conferences and schools. I am also thankful to Professor Adriana Saccone (Coordinator for PhD School) from DCCI, University of Genoa for her support and smooth coordination.

Finally, and most importantly, I would like to thank my whole family. Words can't express my gratitude to them for their unconditional love and support which has been a constant source of motivation for me. Especially I am grateful to my parents for their support and believe in me, which are much precious for me for a long run. My brother, Shubhendu has been always supportive. I have no words in describing his effort in bringing up my scientific skills starting from my childhood days. I have been a great admirer of him. I would also like to thank my sister-in-law Subhashree , my uncle Mr. Abhimanyu, aunt Pushpanjali, Sebati, Rebati, my grandmom Sabitri and all other relative and friends for their love and support. I am grateful to my high school teacher Mr. Laxmidhar Giri for his constant love and caring. This thesis is dedicated to my family.

***Milan Palei***

***December, 2018***
***Genova-Italy***

## Abstract

Light-matter interaction has been a widely investigated phenomena enlarging the area of nanophotonics beyond the limit. This stand out to be the back bone for future generation optical devices. Light confinement and propagation in a small volume gives rise to several rich optical properties. This can be realized in different type of nanostructured materials. Metal(M)/Insulator(I) multilayer nanocavities are highly versatile systems for light confinement and wave guiding at nanoscale. Their physical behavior is discussed successfully by electromagnetic theory. However, it is still obscured about the nature of cavity modes in layered metal/insulator nanocavities. The reason why such cavity mode can be excited without having any momentum matching technique are yet to be investigated. We start with a quantum treatment of the MIM as a double barrier quantum well where the resonant modes are assisted by tunneling of photons. The lossless characteristics of these modes with zero wavevector condition are inherent to the epsilon-near-zero (ENZ) band. We further investigated the coupling between epsilon near zero assisted volume plasmons in MIMIM nanocavities where one MIM cavity placed above the other. Strong coupling has been demonstrated in this system by an anticrossing of the ENZ modes in the individual cavities, where the splitting depends strongly on the thickness of the central metal layer.

The properties of ENZ bulk plasmon modes for MIM and MIMIM systems are exploited to achieve both enhancement of spontaneous emission and decay rate of the perovskite nanocrystal film placed on the top of the nanocavity. However, the enhancement is within the limit of weak coupling regime. In order to achieve strong coupling between ENZ mode of cavity and emission mode of the fluorophore, one need to embed the fluorophore inside the cavity. But it has been realized that in such a case, long term stability of fluorophore by retaining its original optical properties are primary challenges. We studied the optical properties of nanocrystal layer that were overcoated with alumina by atomic layer deposition. This enabled us to effectively embed the NCs inside the dielectric layers of planar MIM and MIMIM nanocavities.

## Table of Contents

## List of Figures

## List of Tables

## List of Publications

Some results of this work have been published before the completion of the PhD thesis, in particular the work on the emission enhancement of perovskite nanocrystal films by MIMIM structures, and the passivation of nanocrystal films via atomic layer deposition of alumina.

1. **Palei, M.**; Caligiuri, V.; Kudera, S.; Krahne, R., Robust and Bright Photoluminescence from Colloidal Nanocrystal/Al2O3 Composite Films fabricated by Atomic Layer Deposition. ACS Applied Materials & Interfaces 2018, 10 (26), pp 22356–22362.

2. Caligiuri, V.; **Palei, M.**; Imran, M.; Manna, L.; Krahne, R., Planar Double-Epsilon-Near-Zero Cavities for Spontaneous Emission and Purcell Effect Enhancement. ACS Photonics 2018, 5 (6), pp 2287–2294.

3. Caligiuri, V.; **Palei, M.**; Biffi, G.; Artyukhin, S.; Krahne, R., A Semi-Classical View on Epsilon-Near-Zero Resonant Tunneling Modes in Metal/Insulator/Metal nanocavities. (Submitted)

# Chapter 1

## Introduction

### 1.1 Optics of Subwavelength Cavities:

Progress in the field of nanotechnology has facilitated the material manufacturing and structures with unique optical properties. In past few decades these materials have raised significant interest in the field of science and technology, because of their ability to control the propagation of electromagnetic waves. There are several ways to control the propagation, subwavelength dielectric films with spatial variation of refractive index across the film are one of them. This is called a gradient photonic barrier.[1] Understanding the physical processes associated with the propagation of electromagnetic waves in heterogeneous environment with variable refractive index at optical frequencies still remains a challenge.

During the last two decades, we have seen significant progress in optics of thin films as it is nourished by tunneling phenomena [2] , especially by tunneling of photons through metallic films.[3] This build the foundation for understanding tunneling phenomena in more complex structure such as metal/insulator multilayer cavities or nanopatterned surfaces. Multilayered metal/insulator structures with negative effective permittivity and permeability are called as metamaterial or left-handed material due to their left hand set of electric field, magnetic field and wave vector.[4] Tunneling of photons in such multilayered cavity is mainly described by frustrated total internal reflection.[5] Total internal reflection (TIR) occurs, when light comes from a optically dense medium to the second medium at large incident angle. This give rise to evanescent field which undergoes exponential decay in the interface of a second medium.[6] Subsequently by placing a third medium with sufficiently large refractive index one can store the propagating waves in a third medium, leading to non-vanishing transmittance. This phenomena is termed as photon tunneling, finds immense application in total reflectance spectroscopy[7] and scanning tunneling microscopy.[8] It is found that when a third medium is replaced by such left hand materials, photons tunnel through a greater distance.[9]

Recently a class of material with effective permittivity and/or permeability near zero have drawn significant interest. They find interesting application in a wide range of research problems, like squeezing electromagnetic energy through a very narrow channel [10], design of matched zero-index material and reshaping the radiation coming from the source. [11] Such materials with epsilon near zero (ENZ) can be found in nature. Some of the commonly available ENZ material are metals like gold and silver at optical frequency, doped semiconductor like indium tin oxide (ITO) and Aluminum zinc oxide (AZO) and some polar dielectric materials like SiC, behave as ENZ material

near their plasma frequency. However, due to low effective mass of electrons, the ENZ frequency is mostly pushed towards ultraviolet regime ($\omega_P \propto \frac{1}{\sqrt{m_e}}$). Moreover, the large effective mass of the ions shifts the ENZ wavelength more towards IR. Hence very few materials available that shows ENZ wavelength in visible. It has been recently demonstrated that one can even design ENZ metamaterial at desired frequency by embedding suitable fillers in a host medium.[12] Here we design silver (Ag)/alumina ($Al_2O_3$) multilayers of subwavelength thickness to tune the ENZ wavelength at desirable optical frequency. The resonant tunneling phenomena at ENZ frequency have been studied for MIM and MIMIM. As a consequence, strong optical anisotropy has been demonstrated.

Further, we also demonstrate the long-range radiating behavior of ENZ mode. In order to exploit this property, MIM and MIMIM are coupled to quantum emitters. We choose colloidal nanocrystal as an emitter, due to their excellent optical properties, where the optical properties as for example the light emission wavelength, direction and polarization can be controlled via the nanocrystal size, shape and composition. This is primarily important when it comes to tune the emission of emitters to the ENZ resonance of MIM and MIMIM. In this thesis, we investigate the coupling between bulk plasmon polariton (BPP) mode at ENZ wavelength and the exciton of the colloidal nanocrystal when they interact with each other. Depending on the energy exchange between two oscillators the coupling can be either weak or strong. The weak coupling also known as Purcell effect has been demonstrated by putting the emitters on the top of the cavity. Similarly, by embedding the nanocrystals inside the cavity we ultimately enhance the energy exchange between the oscillator which has been seen as splitting in photoluminescence spectra, a direct signature of strong coupling. Moreover, we have also investigated plasmon-exciton coupling for other nanostructure, for example polarization dependent plasmon enhanced fluorescence has been studied in an anisotropic gold nanostructure coupled to monolayer of colloidal quantum dots (Appendix A).

## 1.2 Scope of the Thesis:

This thesis is devoted to experimental demonstration of light matter interaction in a near-zero-index planar nanocavity and their coupling with excitons of semiconductor nanocrystals.

In chapter 2 we give brief introduction to colloidal nanocrystal and their fundamental optical properties. Photophysical properties of core-shell type and perovskite nanocrystal are discussed in brief. Surface plasmons are introduced in the proximity of metal/dielectric interface. Further we discuss surface plasmon polaritons in multilayer system comprising metal and insulator layers. After this, epsilon-near-zero materials are discussed followed by brief introduction of resonant tunneling phenomena, and exciton plasmon coupling is briefly introduced. As fluorescence spectroscopy is one of the fundamental tools to measure such coupling phenomena, we introduce fluorescent spectroscopy of quantum dots.

A detailed description of the experimental techniques, film fabrication processes and characterization are presented in chapter 3. We start with discussing important steps involved in getting a uniform and homogeneous spin coated NCs film, followed by characterization of the film by optical and electron microscopy and profilometer for information on film thickness. We further discuss ALD processes on colloidal NCs film. Two standard ALD process, thermal and plasma ALD, are discussed in brief followed by the example of deposition of alumina by ALD. Thermal ALD of alumina on colloidal nanocrystal is discussed in detail. Being a precise nanofabrication tool for depositing oxides with sub nanometer precision, this chapter introduces the technical importance of ALD for fabricating planar nanocavities where it is possible to precisely control the cavity thickness. Detailed fabrication steps involved for making MIM and MIMIM multilayer nanocavities are also discussed.

In chapter 4 we give brief introduction to ellipsometry and its application for characterizing colloidal nanocrystal and multilayer nanocavities. We give special emphasis on analyzing absorbing samples like metals by ellipsometry. Moreover, a detailed description is given on analyzing multilayer metal/insulator nanocavities and their corresponding optical constants, which are prerequisite for designing near-zero-index nanocavity.

A detailed description of the experimental techniques, film fabrication processes and characterization are presented in chapter 5. We start with discussing important steps involved in getting a uniform and homogeneous spin coated NCs film, followed by characterization of the film by optical and electron microscopy and profilometer for information on film thickness. We further discuss ALD processes on colloidal NCs film. Detailed fabrication steps involved for making MIM and MIMIM multilayer nanocavities are discussed.

Chapter 5 aims at designing near-zero-index planar metal/insulator nanocavities and investigation of light matter interaction. Epsilon-Near-Zero nature of such a multilayer cavity is analyzed both by theory and experiments. We find excellent agreement between Scattering Matrix Method (SMM) based simulation and experimental observation of modes MIM and MIMIM. Resonant tunneling phenomena are described in a quantum framework which gives fundamental insight in to tunneling of photons in a double barrier quantum well that corresponds to the MIM system. Moreover, based on this we design a refractive index sensor based on metal/insulator/metal nanocavities. Strong coupling as a demonstration of anticrossing of low and high energy resonant mode are shown for MIMIM.

Chapter 6 focuses on coupling between ENZ mode for MIM and MIMIM with fluorophores placed on the top. Surface Plasmon Coupled Emission (SPCE) and Surface Plasmon Enhanced

Absorption (SPEA) are demonstrated for MIMIM nanoresonator, which introduces Purcell effect and spontaneous emission enhancement.

When it comes to integrate colloidal nanocrystal in to an optical nanocavities, long term stability is a crucial factor. We improve the stability of nanocrystal films by coating them with thin layer of oxide by atomic layer deposition. Chapter 7 describes in detail, how ALD works on colloidal nanocrystal films, and studies their corresponding optical properties.

At the end we describe how strong coupling between resonant mode at ENZ and excitons from nanocrystal can be achieved by simply embedding the nanocrystal in a planar nanocavity. In chapter 8, we demonstrate energy exchange between ENZ resonance and emission band of NCs can be achieved when the emitters are embedded inside the nanocavites. We managed to achieve the resonance matching conditions between MIM and MIMIM resonances with the emission of the QDs layer which is confirmed by spectroscopic ellipsometry.

Chapter 9 gives a summary and outlook for the thesis.

# Chapter 2

## 2.1. Colloidal Nanocrystals for Photonic and Plasmonic Devices:

Colloidal Nanocrystals are known for their excellent optical properties, where the light emission wavelength, direction and polarization can be controlled via the nanocrystal size, shape and composition. Owing to this tunable optical and material properties of these systems, one can find many potential applications including light emitting diodes[13], continuous lasing[14], components for quantum computing, solar cells and other photo voltaic devices.[15] Due to the scalable optical and material properties with easy processability, colloidal nanocrystals find immense potential for device applications. Moreover, colloidal quantum dots are largely specified as a gain material due to their ultra-high quantum yield (close to unity), large transition dipole moments, good photostability and ability to make homogenous dense film without affecting the self-quenching effects that observed in organic dyes. In present thesis, we have extensively used colloidal nanocrystals due to their unique optical properties like large absorption band and narrow emission. For example, in chapter 7, we take advantage of large absorption band and narrow emission of $CsPbBr_3$ colloidal nanocrystals by coupling them to the ENZ mode of MIM and MIMIM cavity. Colloidal nanocrystals can be easily processed and integrated to photonic and plasmonic structures thanks to their solubility in different solvents. Large monodisperse nature of colloidal quantum dots in different solvent allows to obtain monolayer continuous film over any plasmonic rough surface. Appendix A highlights deposition of monolayer Langmuir Blodgett quantum dots on nanostructured gold surface. Further, the colloidal nanocrystals can be easily passivated by thin layer of dielectric oxides by atomic layer deposition which stabilizes their photoluminescence properties over a long time. Such surface coating is highly essential for integrating nanocrystals inside photonic and plasmonic nanocavities as shown in chapter 9 of this thesis. We describe here some of the fundamental optical properties of colloidal quantum dot.

## 2.2 Band-Edge Quantum Size Levels:

Semiconductor crystals those are smaller than the bulk exciton Bohr radius, the energy spectrum and the wave functions of the exciton (electron-hole) pairs can be predicted by using independent quantization rule for both electron and holes motion, which is also called as strong confinement.[16] The exact quantization of electron and hole confinement energies and wavefunctions can be found in the framework of multiband effective mass approximation.[17] For spherically shaped NCs of cubic lattice structure, the degeneracy of electron and hole in the ground state are different. The first electron quantum size level($1S_e$) is doubly degenerate with respect to spin orientation whereas the first hole of the quantum sized level ($1S_{3/2}$) is fourfold degenerate with respect to angular momentum wave vector. The energy and wave function of these quantum sized object is given by

For electrons

$$E_{1s} = \frac{h^2}{8m_e a^2} \tag{2.1}$$

$$\psi_\alpha(r) = \xi(r)|S\alpha\rangle = \sqrt{\frac{2}{a}}\frac{Sin\left(\frac{\pi r}{a}\right)}{r} Y_{00}(\Omega)|S\alpha\rangle \tag{2.2}$$

Where $m_e$ is the electron effective mass, a is nanocrystal radius, $Y_{lm}(\Omega)$ are the spherical harmonic functions, $|S\alpha\rangle$ is the Bloch wave function of the conduction band, $\alpha$ is the projection of electron spin, $s_z = +(-)1/2$. Similarly, hole having fourfold degenerate valence band, the energy level and wavefunction can be written as

$$E_{\frac{3}{2}}(\beta) = \frac{h^2\varphi^2(\beta)}{8\pi^2 m_{hh} a^2} \tag{2.3}$$

$$\psi_M(r) = 2\sum_{l=0,2} R_l(r)(-1)^{M-3/2} \sum_{m+\mu=M} \begin{pmatrix} \frac{3}{2} & l & \frac{3}{2} \\ \mu & m & -M \end{pmatrix} Y_{lm}(\Omega) u_\mu \tag{2.4}$$

Where $\beta = m_{lh}/m_{hh}$ is the ratio between light to heavy hole effective masses, $u_\mu$ are the Bloch functions of the four-fold degenerate valence band.

For spherical dots like CdSe, PbS, CdS; the exciton ground state ($1S_{3/2}\,1S_e$) is eightfold degenerate. However, the degeneracy is lifted by shape and anisotropy of the internal crystal structure along with the electron-hole exchange interaction. Both NCs size and shape largely control the energy splitting and transition oscillator strength of the split-off states along with their odering.[16] This is particularly important while coupling the NCs to the plasmonics or photonic platform. Taking in to account of the oscillator strength of each split-off state, the effective energy exchange between fluorophore emission and plasmonic resonances can be determine in a hybrid system.

## 2.3 Relaxation Processes in Semiconductor Nanocrystals:

When light incident on quantum confined semiconductor nanocrystals systems, the electron from ground state move to the excited state. The excited state is very unstable, hence the excitons from the excited state relaxes. This relaxation process can be followed by different pathways like radiative and nonradiative ways. The photoexcitation process can create both single or multiexcitons in a nanocrystal depending on several nonlinearities and incident intensity. Followed by optical absorption, the exciton may be excited into many states associated with either vibration or fine structure mainly caused by exchange and crystal field effects[18]. The excitons can nonradiatively relaxes through these states before recombining or returning to the ground states as shown in figure 2.1d. In a molecular system, the relaxation happens through internal conversion due to high frequency vibrational modes. For example, in CdSe nanocrystal the observed intraband relaxation is very fast in the order of sub picoseconds timescales.[19] This can be explained by Auger recombination, where the fast intraband process is mediated by transfer of energy from the electron to hole.[20] Depending on whether the hole is more massive than the electron or vice versa the energy level separation and ultra-fast relaxation process are explained.

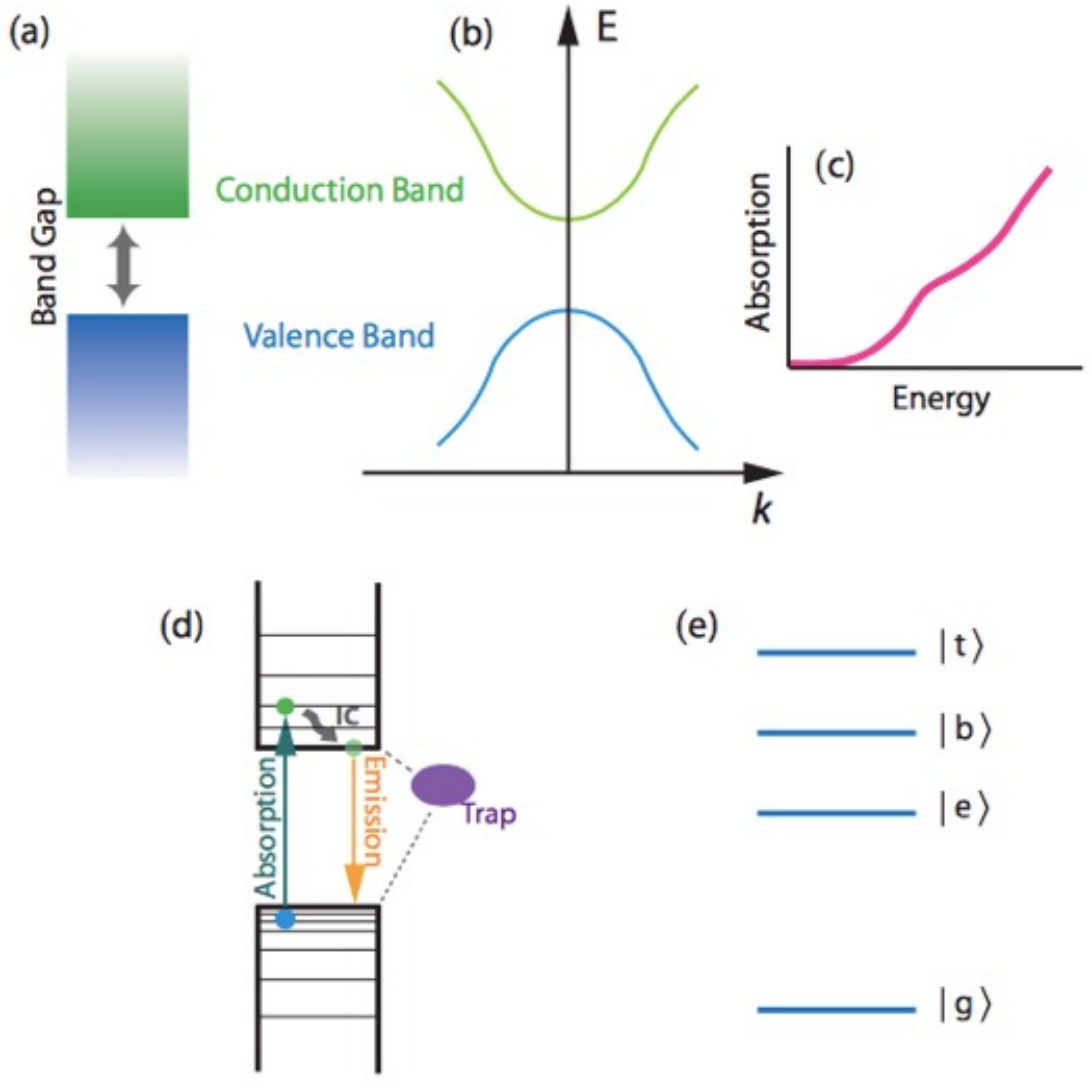


Figure 2.1 Represents photophysical properties of semiconductors both in bulk and quantum confined. (a), (b), (c) corresponds to the bulk system followed by lower panel (d) and (e) representing confined semiconductor nanocrystals. (a) shows the delocalized orbitals and continuous levels of conductions and valence bands separated by the band gap in real space (b) represents in reciprocal space (c) the continuous and step like increase of bandgap followed by continuous absorption of high energy states (d) represents an electron and hole scheme of energy level for quantum confined semiconductor nanocrystal (e) shows the excitonic basis representation of quantum confined semiconductor nanocrystal, where g, e, b, and t are the ground, exciton, biexciton and triexciton states (reproduced with permission from Huxter et. al.[18])

## 2.4 Liner Polarization Memory Effect:

The linearly polarized selectively excites NCs with the hexagonal axis preferentially parallel to the polarization wave vector of incident light when the excitation frequency is in resonance with the bright excited state i.e. F=0. Bawendi et. al. first described such kind of effect in nanocrystals PL emission.[21] In a randomly oriented sample of nanocrystal, the polarization memory effect is mainly

due to the selective excitation of some of the NCs that have special orientation of the hexagonal axis relative to the polarization direction of the exciting light. Hence, the polarization dependent photoluminescence properties of NCs is mainly determined by the polarization properties of ground state and NCs orientations.

## 2.5 Multiexciton in Semiconductor Nanocrystals:

The shape, size and composition of the semiconductor nanocrystals gives rise to quantized multifold of electronic states called as excitons. Moreover, nanocrystals can also support multiple excitations per particle under normal condition. These multiexcitons largely control many optoelectrical properties of the nanocrystals like from lasers, light-emitting diode, photon sources and photovoltaics. The simplest multiexciton is the biexciton which is a four-particle complex system consisting of two electrons and two holes.[22] The quantum confinement effect in semiconductor nanocrystals binds both excitons and multiexcitons as compared to their bulk counterpart. The presence of biexciton also can determine the optical gain threshold for semiconductor nanocrystals. It has been realized that the formation of multiexcitons in semiconductor nanocrystals pave away many difficulties for performance of optoelectronics device.

## 2.6. Core-Shell Type Nanocrystals:

Core-shell type quantum dots exhibit interesting properties which make them special for both experimental and theoretical point of view. Overcoating the nanocrystalline with higher band gap inorganic material has been known to improve the photoluminescence quantum yields by passivating the surface which suppresses the non-radiative recombination centers. Surface passivation make nanocrystal more robust and tolerant for their use in solid state devices. In core/shell type quantum dots, absorption and emission spectra can be well controlled by tuning both the size of the core and thickness of the shell layer. Most commonly used core-shell type of nanocrystals are CdS on CdSe, ZnS on CdSe, ZnSe on CdSe, CdS on PbS. The optical absorption of the core/shell nanocrystals can be tuned by changing the size of the core. For example, in PbS/CdS core/shell quantum dots, the first excitonic peak in absorption spectra can be spanned in a broad range by varying the size of the PbS core and the thickness of the CdS shell[23]. Here we will discuss two main type of core-shell nanocrystal used in this thesis.

### 2.6.1. CdSe/ZnS Dots-in-Dots

For most of the optoelectronic applications it is found that core-only QD are not the ideal materials, as they suffer photo-induced oxidation. [24] It has been reported that by coating high band gap shell on CdSe core form a type-I core-shell structure which significantly improve the photostability. [25] The ZnS shell not only passivate the traps on the surface[26] but also insulates the holes of the core and hence reduce the photodegradation.[27]

Figure 2.2a shows schematics of CdSe/ZnS core-shell nanostructure. As shown in figure 2.2b the energy bandgap for ZnS shell is higher than the CdSe shell which favors their application in photovoltaics. The emission of the heterostructure is determined by the size of the core. Excellent stability of CdSe/ZnS core-shell nanoparticles with tunable emission broaden their application in various field like bioimaging, optoelectronics, sensing and many more. Moreover, there has been a significant use of CdSe/ZnS core-shell type nanocrystals in photonic and plasmonic devices.[28-29]

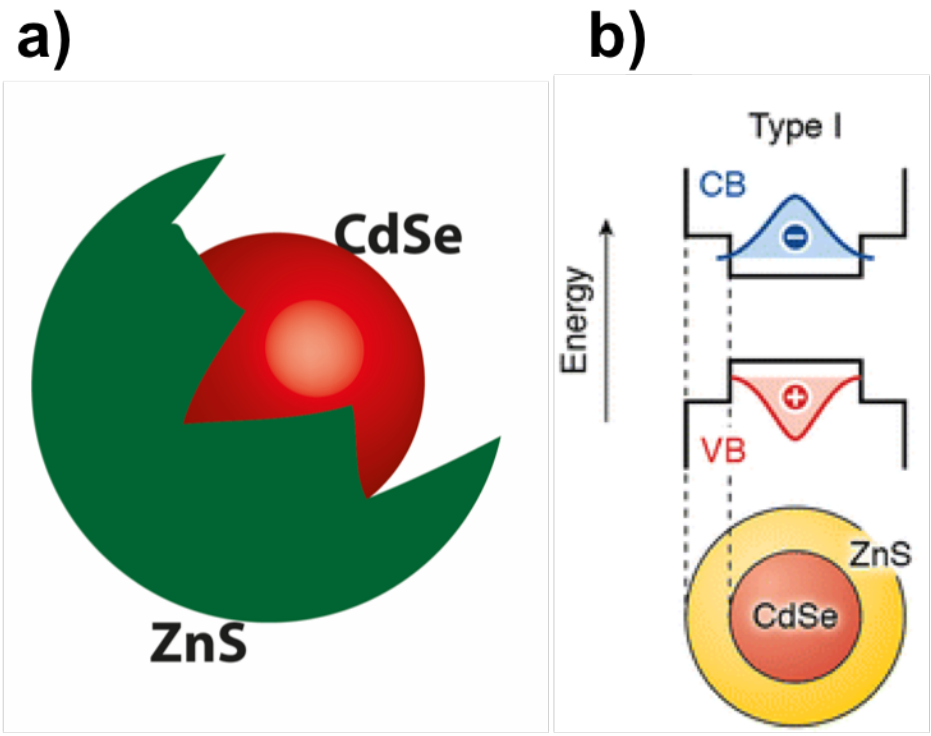


Figure 2.2 a) Schematics of CdSe/ZnS core-shell structure b) Energy band alignment for CdSe/ZnS core-shell heterostructure (reproduced with permission from Rabouw et. al.[30])

### 2.6.2 CdSe/CdS Dot-in-Rod

Figure 2.3a shows schematics of CdSe/CdS Dot-in-Rod nanocrystal,[31] where a high energy band gap CdS shell (rod type) encapsulate the CdSe core. Energy band diagram for this heterostructure are shown in figure 2.3b. The hole in this type of structure is known to be localized at the CdSe core due to the large valence band offsets between CdSe and CdS. On the other hand, the conduction band offsets are quite small in the bulk and thus the electron can delocalize into the shell, depending on the size of the core, leading to a possible transition from type-I to a quasi-type-II. When both electron and hole are confined to the core they are categorized as type-I band and on the other hand when only hole are confined to the core but not the electron, are termed as quasi-type-II band. In general, where both the electron and hole are confined to the same region, the

nanostructure show remarkable bright and stable fluorescence. Moreover, the elongated shell (rod type) on CdSe core strengthen linear polarization in comparison to the nearly spherical core-shell geometry.[32-33]

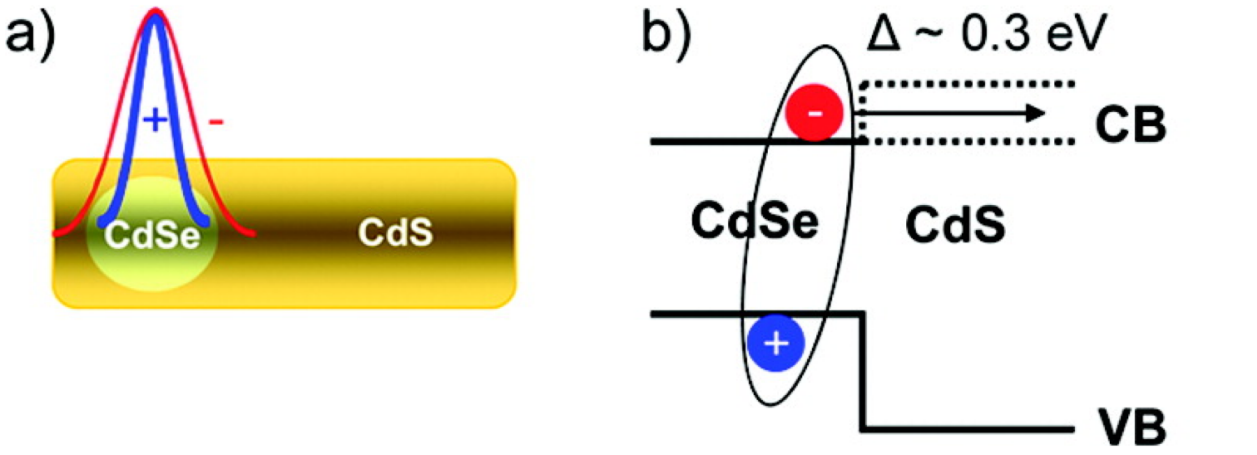


Figure 2.3 a) Schematics of CdSe/CdS Dot-in-Rod heterostructure b) Energy band alignment for CdSe/CdS Dot-in-Rod (reproduced with permission from Raino et. al.[34])

### 2.6.3. $CsPbBr_3$ Perovskite Nanocrystal:

Lead halide perovskites (LHP) have emerged as the highly promising material in the field of colloidal semiconductor nanocrystal due to their novel optical and electronic properties.[35] Out of all the perovskites that possesses remarkable photo response and transport properties, the one without organic ions are promising as they are quite stable at elevated temperature. Such thermal stabilities are essential for devices that needs elevated temperature like LED, which produces considerable Joule heating at higher open circuit voltage.

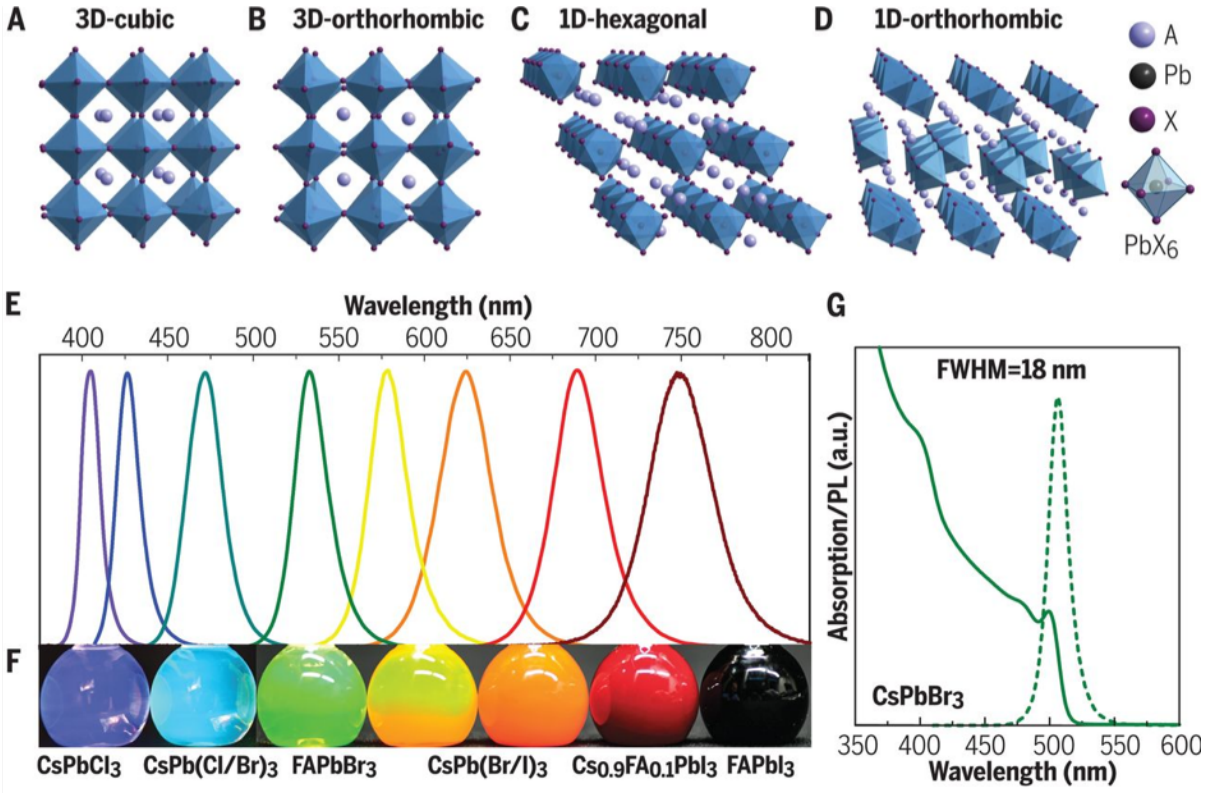


Figure 2.4 (A,B,C,D) Schematics of crystal structure of 3D lead bromide based perovskites compared to the 1D nonperovskite polymorphs E) Survey of PL spectra F) image of as synthesized crystal solution under UV light G) absorption and PL spectra of 8nm $CsPbBr_3$ nanocrystal (reproduced with permission from Kovalenko et.al.) [36]

Out of all-inorganic LHP, $CsPbBr_3$ has been broadly studied due to their excellent optical properties and scalable emission in green.[37] Figure 2.4 shows crystal structure and optical properties of most common lead bromide-based perovskites studied recently. Apart from promising optical and electronic properties, $CsPbBr_3$ possesses broad band absorbance features. Broadband nature in absorbance is particularly interesting for plasmonic community where one is interested to couple the resonant mode of a plasmonic cavity to the absorbance of an emitter to have maximum energy transfer between them. This is also termed as surface plasmon enhanced absorption (SPEA).

## 2.7 Surface Plasmons:

Longitudinal charge density fluctuation at the interface between the metal and dielectric is known as surface plasmons. [38] Surface plasmons can be excited by light with adequate momentum matching, and exhibit much shorter wavelength then the photon in free space, and hence enable to miniaturize the photonic technology. Surface plasmon can be categorized into two

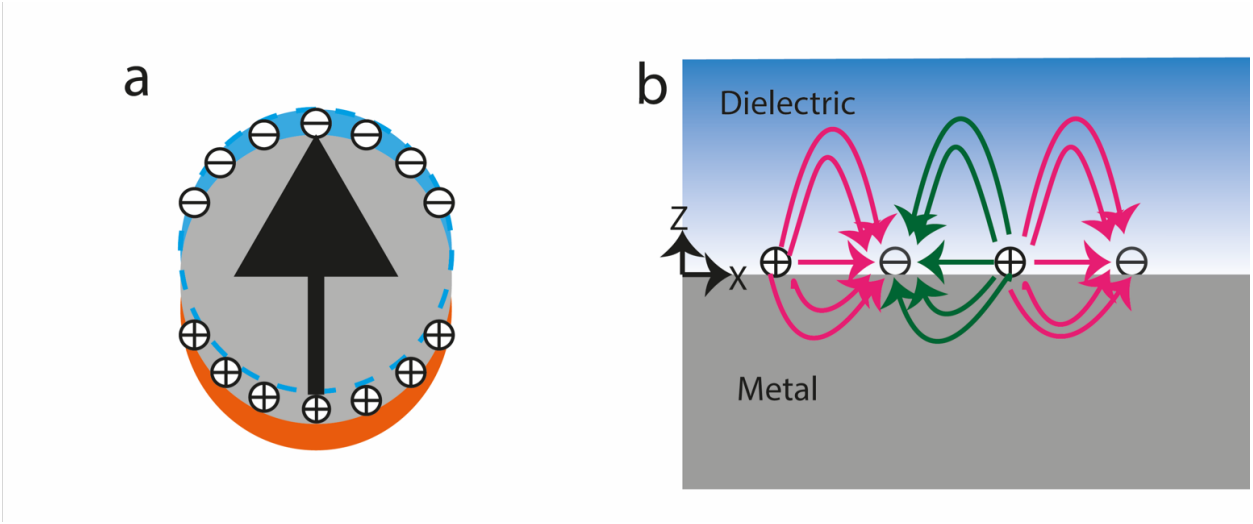


Figure 2.5 (a) Shows plasmons in a particle. Electromagnetic field causes distortion in the electron cloud of a particle, where negative charge leaves behind positive charge of the particle. The as formed electron cloud oscillates at dipole plasmon frequency (b) surface plasmon at the interface of metal and dielectric where an incident field excites charge compression waves which propagates in the interface between metal and dielectric

main types: localized surface plasmons (LSPs), and propagating surface plasmon polaritons (SPPs). A typical example of localized surface plasmon (LSPs) is based on a nanoparticle as shown in figure 2.5a. The incident electromagnetic wave causes a coherent oscillation of the electron cloud which results in a time dependent polarization of the particle (Figure 2.5a). A restoring force arises from the Coulomb attraction between the displaced electrons and the positively charged nuclei, and the electron cloud performs a resonant oscillation.[39] Plasmonic nanoparticles find application in many field such as surface enhanced Raman spectroscopy[40-41] , hyperthermia treatment[42], for enhancing the absorption in solar cells[43] , and light controlled drug release.[44]

## 2.8 Surface Plasmon Polaritons at Metal/Insulator Interfaces:

Surface plasmon polaritons are electromagnetic excitations that propagate at the interface of a dielectric and a conductor. [45] These excitations are evanescently confined in a perpendicular direction to the interface. They arise as a result of coupling of electromagnetic field to the electron plasma in a conductor. Figure 2.5b shows schematically the SPP propagation at the interface of a metal and dielectric. In order to investigate the physical properties of surface plasmon polariton wave, one needs to apply Maxwell's equations for a metal/dielectric interface. In the absence of external charge and current densities, Maxwell's equation can be combined and written as

$$\nabla \times \nabla \times E = -\mu_0 \frac{\partial^2 D}{\partial t^2} \tag{2.5}$$

Equation 2.5 can further be simplified using the identity $\nabla \times \nabla \times E = \nabla(\nabla \mathrm{E}) - \nabla^2 E$ and $\nabla(\varepsilon \mathrm{E}) = \varepsilon(\nabla \mathrm{E}) + \mathrm{E}(\nabla \varepsilon)$. Using the approximation $\nabla . \mathrm{D} = 0$ for absence of any external stimuli, equation 2.5 can be rewritten as

$$\nabla\left(-\frac{1}{\varepsilon} E . \nabla \varepsilon\right) - \nabla^2 E = -\mu_0 \varepsilon_0 \varepsilon \frac{\partial^2 E}{\partial t^2} \tag{2.6}$$

For small variation of dielectric profile $\varepsilon(\mathrm{r})$ in space with in one optical wavelength, equation 2.6 simplifies to

$$\nabla^2 E - \frac{\varepsilon}{c^2} \frac{\partial^2 E}{\partial t^2} = 0 \tag{2.7}$$

Equation 2.7 can be solved in two steps. First, we assume that the time dependent nature of the electric field is given by $\mathrm{E}(\mathrm{r}, \mathrm{t}) = \mathrm{E}(\mathrm{r}) \mathrm{e}^{-\mathrm{i}\omega \mathrm{t}}$ . Inserting this into (2.7) gives

$$\nabla^2 E + k_0^2 \varepsilon E = 0 \tag{2.8}$$

Where $k_0 = \frac{\omega}{c}$ is the wave vector of the propagating wave in vacuum. Equation 2.8 is known as Helmholtz equation.

In order to solve the above equation, we assume it as a one-dimensional problem where the wave propagates along x-direction and shows no spatial variation in y. Hence $\varepsilon = \varepsilon(z)$, applying this to the surface where z=0, the propagation wave can be written as $E(x, y, z) = E(z) e^{i\beta x}$, where $\beta = k_x$ is the propagation constant. By putting the value of $E(x, y, z)$ in equation 2.8, we obtain

$$\frac{\partial^2 E(z)}{\partial z^2} + (k_0^2 \varepsilon - \beta^2) E = 0 \tag{2.9}$$

Equation 2.9 is the fundamental equation for electromagnetic wave in a waveguide and an extended discussion can be found in Yariv et. al.[46] We now need to find different expression for various field components of E and H. This can be achieved by applying the curl equation with proper boundary conditions as described in detail by Maier et.al. [47]

One can express the representing equation for both TM and TE modes, which are given as

For TM modes

$$\frac{\partial^2 H_y}{\partial z^2} + (k_0^2 \varepsilon - \beta^2) H_y = 0 \tag{2.10}$$

And for TE modes

$$\frac{\partial^2 E_y}{\partial y^2} + (k_0^2 \varepsilon - \beta^2) E_y = 0 \tag{2.11}$$

With this equation in mind, now we can go for description for surface plasmon polaritons.

## 2.9 Surface Plasmon Polaritons (SPPs) at Metal/Dielectric Single Interface:

The simplest geometry as a model for SPPs mode is the single interface between a dielectric material, non-absorbing half space ($z > 0$) with positive real dielectric function $\varepsilon_2(\omega)$ and an adjacent conducting half space ($z < 0$) with negative real dielectric function $\varepsilon_1(\omega)$. The metallic characteristics appear in a material when $Re(\varepsilon_1) < 0$. It has been seen that most of the metallic conditions are fulfilled at frequencies below the plasma frequency of the metal ($\omega_p$). We are interested in finding the solution for a propagating wave confined at the interface, which decays in z-direction.

The TM solution at the interface can be explicitly derived by solving the field equation in both half spaces defined by the plane, and applying the continuity condition at the interface; we get

$$\frac{k_2}{k_1} = -\frac{\varepsilon_2}{\varepsilon_1} \tag{2.12}$$

All the approximations made to derive the expression as represented in equation 2.12 demand $Re(\varepsilon_1) < 0$ only if $\varepsilon_2 > 0$, i.e. an interface between a conductor and an insulator. The expression for $H_y$ as shown in equation 2.10 yields

$$k_1^2 = \beta^2 - k_0^2\varepsilon_1 \tag{2.13}$$

$$k_2^2 = \beta^2 - k_0^2\varepsilon_2 \tag{2.14}$$

Combining equation 2.12, 2.3 and 2.14, we get

$$\beta = k_0\sqrt{\frac{\varepsilon_1\varepsilon_2}{\varepsilon_1 + \varepsilon_2}} \tag{2.15}$$

Equation 2.15 gives the dispersion relation of an SPP wave travelling at the interface of a conductor and an insulator. Before giving any physical insight of equation 2.15, we need to find the similar solution for TE waves. Applying the proper boundary conditions to equation 2.11, we get

$$A_1(k_1 + k_2) = 0 \tag{2.16}$$

Since confinement to the surface needs to satisfy $Re(k_1), Re(k_2) > 0$ the equation 2.16 is valid only when $A_1 = 0$ which also makes $A_2 = 0$. Thus, no surface modes exists for TE polarization, which demonstrates that SPP modes only exists for TM polarization.

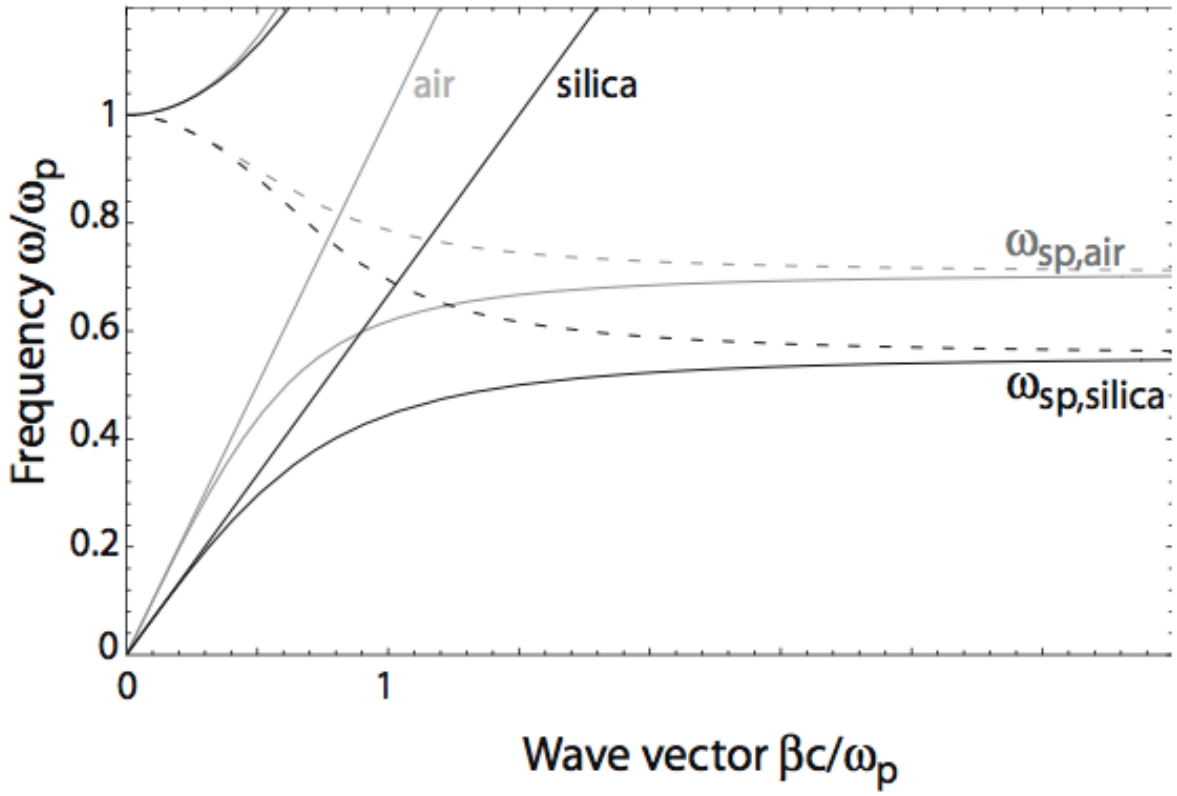


Figure 2.6. Dispersion relation of SPPs at the interface between a Drude metal and air/light line (gray curve) and silica (black curve) (reproduced with permission from book of Stefan A. Maier[45])

Figure 2.6 shows the plot of equation 2.15 for a metal with negligible damping which is described by a real Drude dielectric function, i.e. $\varepsilon_2 = 1$ for air and $\varepsilon_2 = 2.25$ for fused silica. In the above plot, $\omega$ is normalized to the plasma frequency $\omega_p$. Due to bound nature of the SPP mode, the dispersion curve for metal/air and metal/silver always lie on the right side of the light line in the corresponding dielectric medium. Therefore, to excite SPPs mode, one need proper phase matching techniques like grating or prism coupling. The behavior of the dispersion relation in for small wave and large wave vectors are different. For large wave vectors, the frequency of SPPs approaches to that of a characteristic's frequency of a surface plasmon given by

$$\omega_{sp} = \frac{\omega_p}{\sqrt{1+\varepsilon_2}} \tag{2.17}$$

This can be realized by inserting the free-electron dielectric wavefunction in to equation 2.11.

## 2.10 Multilayer Systems:

In multilayer systems of conducting and dielectric stacks, each single interface confines SPPs mode. When the separation between adjacent interfaces is comparable or smaller than the decay length of the interface mode, the two SPPs mode interact and give rise coupled modes. In order to

exploit this coupling, we will discuss two simple systems, where the first one is made of a metal layer of finite thickness sandwiched between two infinite dielectric cladding layers named as Insulator/Metal/Insulator (IMI) system. Where for the second configuration, a thin dielectric layer is sandwiched between two metal cladding layer , which we call Metal/Insulator/Metal (MIM) system. We are only interested in lowest order bound mode which is given by TM modes that are non-oscillatory in the z-direction, i.e. perpendicular to the surface. For $z > a$, the field components are given by

$$H_y = Ae^{i\beta x}e^{-k_3 z} \tag{2.18a}$$

$$E_x = iA\frac{1}{\omega\varepsilon_0\varepsilon_3}k_3 e^{i\beta x}e^{-k_3 z} \tag{2.18b}$$

$$E_z = -A\frac{1}{\omega\varepsilon_0\varepsilon_3}k_3 e^{i\beta x}e^{-k_3 z} \tag{2.18c}$$

Similarly, for $z < -a$,

$$H_y = Be^{i\beta x}e^{k_2 z} \tag{2.19a}$$

$$E_x = iB\frac{1}{\omega\varepsilon_0\varepsilon_2}k_2 e^{i\beta x}e^{-k_2 z} \tag{2.19b}$$

$$E_z = -B\frac{\beta}{\omega\varepsilon_0\varepsilon_3}e^{i\beta x}e^{k_2 z} \tag{2.19c}$$

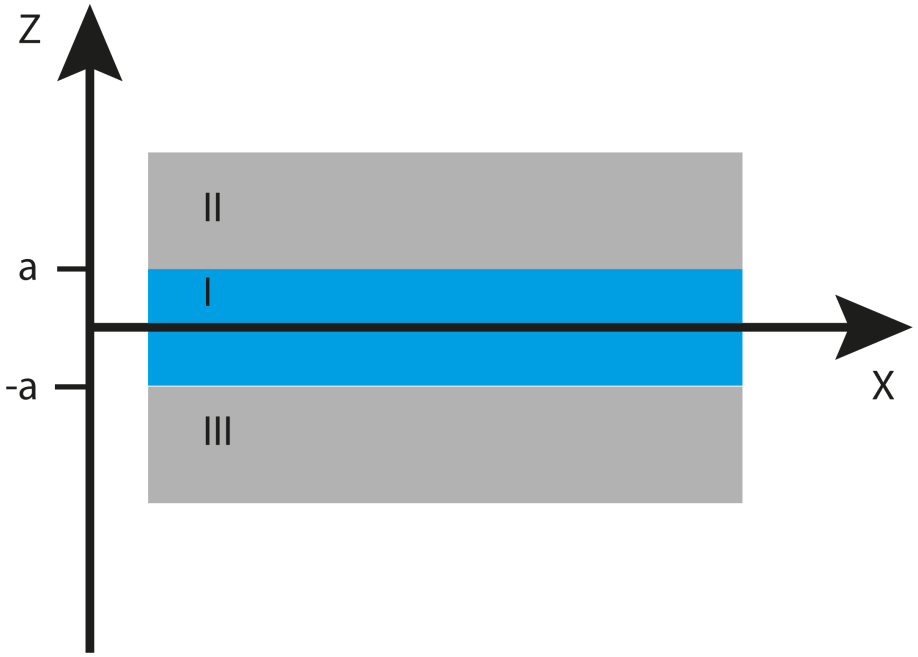


Figure 2.7 Schematics of a three-layer system where a thin layer metal layer is sandwiched between two dielectric layers

The field decays exponentially in the dielectric claddings II and III. For simplifying the above expression, we assume the component of wave vector perpendicular to the interfaces as $k_i \equiv k_{z,i}$ , the core region $-a < z < a$, the modes are localized at the both interfaces

$$H_y = Ce^{i\beta x}e^{k_1 z} + De^{i\beta x}e^{-k_1 z} \tag{2.20a}$$

$$E_x = -iC\frac{1}{\omega\varepsilon_0\varepsilon_1}k_1 e^{i\beta x}e^{k_1 z} + iD\frac{1}{\omega\varepsilon_0\varepsilon_1}k_1 e^{i\beta x}e^{-k_1 z} \tag{2.20b}$$

$$E_z = C\frac{\beta}{\omega\varepsilon_0\varepsilon_1}e^{i\beta x}e^{k_1 z} + D\frac{\beta}{\omega\varepsilon_0\varepsilon_1}e^{i\beta x}e^{-k_1 z} \tag{2.20c}$$

Applying continuity of $H_y$ and $E_x$ at $z = a$ gives rise to

$$Ae^{-k_3 a} = Ce^{k_1 a} + De^{-k_1 a} \tag{2.21a}$$

$$\frac{A}{\varepsilon_3}k_3 e^{-k_3 a} = -\frac{C}{\varepsilon_1}k_1 e^{k_1 a} + \frac{D}{\varepsilon_1}k_1 e^{-k_1 a} \tag{2.21b}$$

At $z = -a$;

$$Be^{-k_2 a} = Ce^{-k_1 a} + De^{k_1 a} \tag{2.22a}$$

$$-\frac{B}{\varepsilon_2}k_2 e^{-k_2 a} = -\frac{C}{\varepsilon_1}k_1 e^{-k_1 a} + \frac{D}{\varepsilon_1}k_1 e^{k_1 a} \tag{2.22b}$$

$H_y$ has to satisfy the wave equation 2.6 in three separate regions, which gives rise to

$$k_i^2 = \beta^2 - k_0^2\varepsilon_i \tag{2.23}$$

Solving the above system of linear equation results in a dispersion relation

$$e^{-4k_1 a} = \frac{k_1/\varepsilon_1 + k_2/\varepsilon_2}{k_1/\varepsilon_1 - k_2/\varepsilon_2}\,\frac{k_1/\varepsilon_1 + k_3/\varepsilon_3}{k_1/\varepsilon_1 - k_3/\varepsilon_3} \tag{2.24}$$

For infinite thickness of the conducting layer, where $a \to \infty$, the above equation reduces to two uncoupled mode as given by relation 2.12. Considering the case where layer II and III are equal in terms of dielectric response i.e. $\varepsilon_2 = \varepsilon_3$ and $k_2 = k_3$, the above dispersion relation can be reduced to

$$tanhk_1 a = -\frac{k_2\varepsilon_1}{k_1\varepsilon_2} \tag{2.25a}$$

$$tanhk_1 a = -\frac{k_1\varepsilon_2}{k_2\varepsilon_1} \tag{2.25b}$$

The above dispersion relation can be both applied to IMI and MIM systems. However, we are more interested in the MIM system. In MIM system, $\varepsilon_2 = \varepsilon_2(\omega)$ set as a dielectric function of the metal and $\varepsilon_1$ is the dielectric constant of the insulating core in equation 2.25a and 2.25b. The dispersion relation for MIM contains even and odd modes. The odd mode is quite interesting from energy confinement point of view as it is the fundamental modes of the system and does not show

any cut-off for vanishing core thickness.[48] The complete family of the modes in such MIM system is much enriched. The analysis of the modes for MIM plasmonic slot waveguide is given in detail by Dionne et. al..[49] Moreover, the coupling between SPP modes at both core/cladding interfaces changes significantly when the dielectric constant of the cladding layer changes.

## 2.11 Epsilon Near Zero (ENZ) Mode:

Metallic films that are much thinner than the skin depth can support surface plasmon modes whose dispersion relation approaches the plasma frequency, which give rise to so called epsilon near zero (ENZ) modes.[50] ENZ modes are confined and their dispersion relation lies on the right side of the light line, therefore they can be excited by means of Kretschmann geometry[51] or grating couplers. The long range surface properties of these modes were recently shown for the thin-film regime.[52] However ,a clear theoretical description of these modes and their existence in various domain was missing until the fundamental work of Campione et. al. [50]

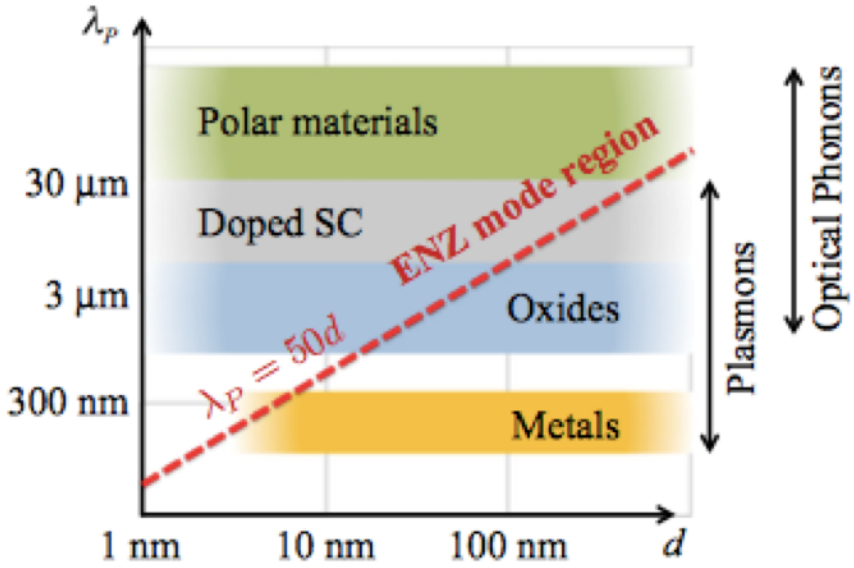


Figure 2.8 Classification of some of the most important material systems that may show ENZ modes (reproduced with permission from Campione et. al. [50]).

Figure 2.8 shows that ENZ modes can be observed in many oxides, doped semiconductor and polar materials, but are hard to demonstrate in metals due to mismatch between the plasma wavelength ($\lambda_p$ ) and thicknesses that can be achieved experimentally. However, for thin metals below the skin depth, ENZ modes can be excited as indicated by the red dotted line in figure 2.8.

As we can see from figure 2.8, it is difficult to find naturally available ENZ materials that have a broad range of ENZ resonances. There is a large gap between metals and dielectrics for example. It is challenging to tune the ENZ resonance in visible or NIR regime either with doping or with

selecting different class of material. Recently, it has been shown that apart from naturally available epsilon near zero (ENZ) mode materials, which we discussed above, it is also possible to engineer materials that show tunable ENZ resonances at visible wavelengths. [53-54]

## 2.12. Exciton Plasmon Coupling:

Excitons are bound state electron-hole pairs that exists in semiconductors, insulators and some liquids as well, which can transfer energy without transporting electric charge.[55-56] The decay of the excitons is largely controlled by the overlap of the wavefunction of the electrons and holes, which also determines their lifetime. The interaction between excitons and plasmons has been investigated both experimentally and theoretically.[57-58] Most studies are related to surface plasmon (SP) coupled exciton hybrid structure. SP can be easily coupled to excitons to form hybrid mode due to their large oscillator strength. Based on the coupling strength, one distinguishes between strong or weak coupling. In the strong coupling regime, the coherent coupling between localized surface plasmon and excitons overcomes the losses and generates mixed states of light that manifest an anticrossing. [59] Such hybrid modes can be seen as new quasi particles called s plexcitons, which have different properties from the constituting exciton and plasmon. However, up to now most of the plexciton coupling phenomena have been studied in the framework of surface plasmons, where the surface plasmon polariton (SPP) or Localized surface plasmon (LSP) interacts with exciton. Recently it has been demonstrated that strong coupling can be seen when planar HMM coupled to ENZ mode of doped semiconductor.[60] However, the coupling between ENZ modes in metal and excitons in semiconductor are yet to be explored.

## 2.13. Fluorescence Spectroscopy:

When a molecule absorbs light, an electron from ground state is promoted to excited state. The excited state may be a singlet state or a triplet state. The molecule stays for very short time in the excited state. The depopulation of the excited state can occur in several ways as shown in figure 2.8.

I. The molecule in the excited state can lose its energy in non-radiative way by giving its energy to another absorbing neighboring species or by collision with another species.
II. When an excited state triplet overlaps with excited state singlet, the molecule can cross-over to triplet state. This cross-over process is known as Inter-System Crossing (figure 2.9). In this condition if a molecule return to the ground state from the single state ($T_1 \rightarrow S_0$) by emitting light, the process is called as Phosphorescence.
III. In certain cases, the molecule partially dissipates its energy by undergoing structural changes and relaxed to lowest vibrational level of the excited state. The process is known as vibrational relaxation. However, if the molecule is rigid, it is simply not able to relax vibrationally to the ground state, this enable the molecule to relax to the ground state ($S_1 \rightarrow S_0$) by emitting light, the process is known as Fluorescence (figure 2.9).

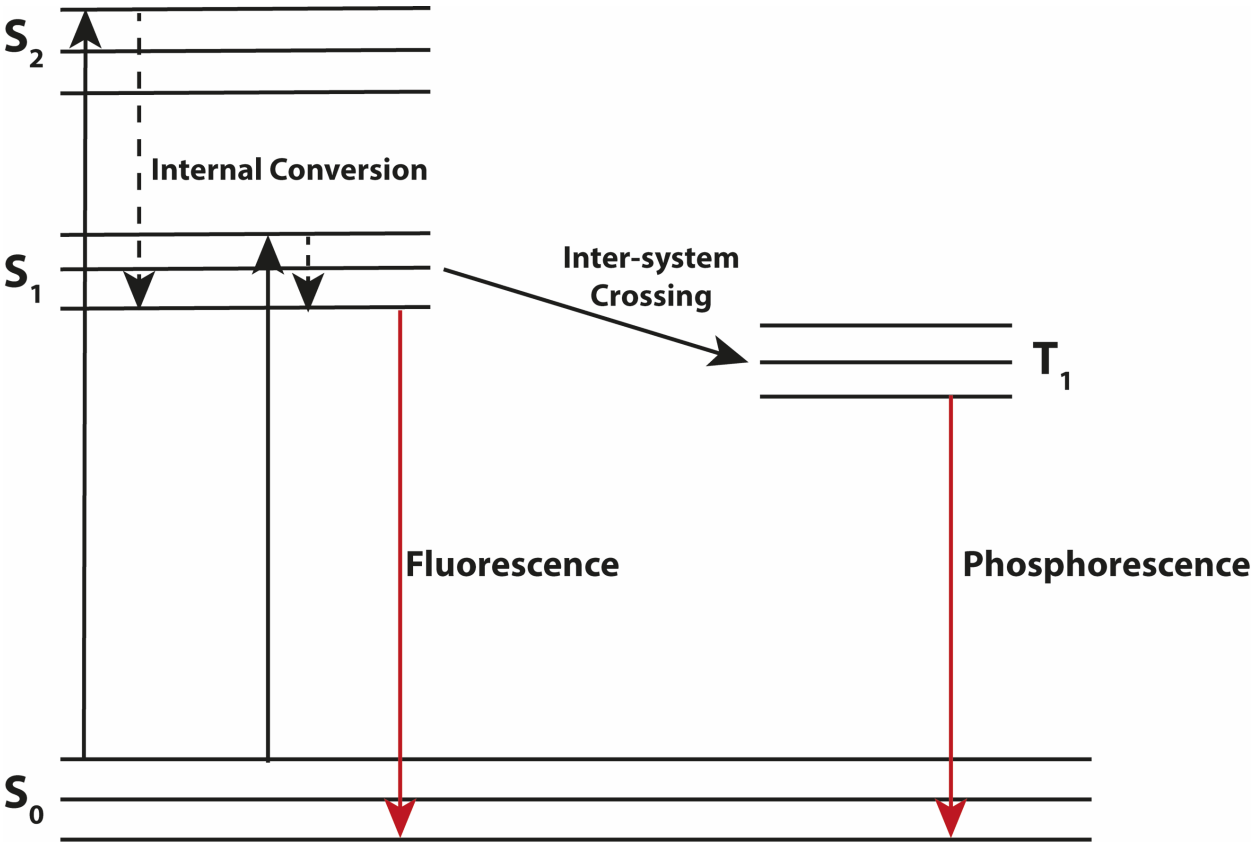

Figure 2.9 Schematics of Jablonski Diagram

## 2.14. Characteristics of Fluorescence Emission:

Some of the most relevant fluorescence characteristic are mentioned below.

### 2.14.1 Stokes Shift:

From Jablonski diagram (figure 2.9) one can infer that the energy of the emission is typically less than that of absorption. Fluorescence generally occurs at lower energy or longer wavelength than the absorption. This phenomenon was first observed by Sir G. G. Stokes in 1852 at the University of Cambridge. [61] Energy loss between excitation and emission are observed in all type of fluorescent molecules both in solution and solid films. One of the common causes of such a Stokes shift is due to fast decay into lowest vibrational level of $S_1$. Moreover, fluorophores also decay to higher vibration state of $S_0$ which results in further loss in excitation energy through thermalization of excess vibrational energy (figure 2.9). In addition to these effect, Stokes shift are also mediated by solvent effects[62], excited state reaction, energy transfer[63], complex formation.

## 2.15. Fluorescence Lifetime and Quantum Yield:

Fluorescence lifetime and quantum yield are very important characteristics of a fluorophore. Quantum yield is determined by number of emitted photons relative to number of absorbed photons. Lifetime contains information about the time available for a fluorophore in order to interact with the surrounding environment, or with other molecules which control its emission properties.

The physical meaning of lifetime and quantum yield are interpreted in terms of Jablonski diagram in figure 2.10. In this case, we simplified the relaxation process in the excited state by focusing on

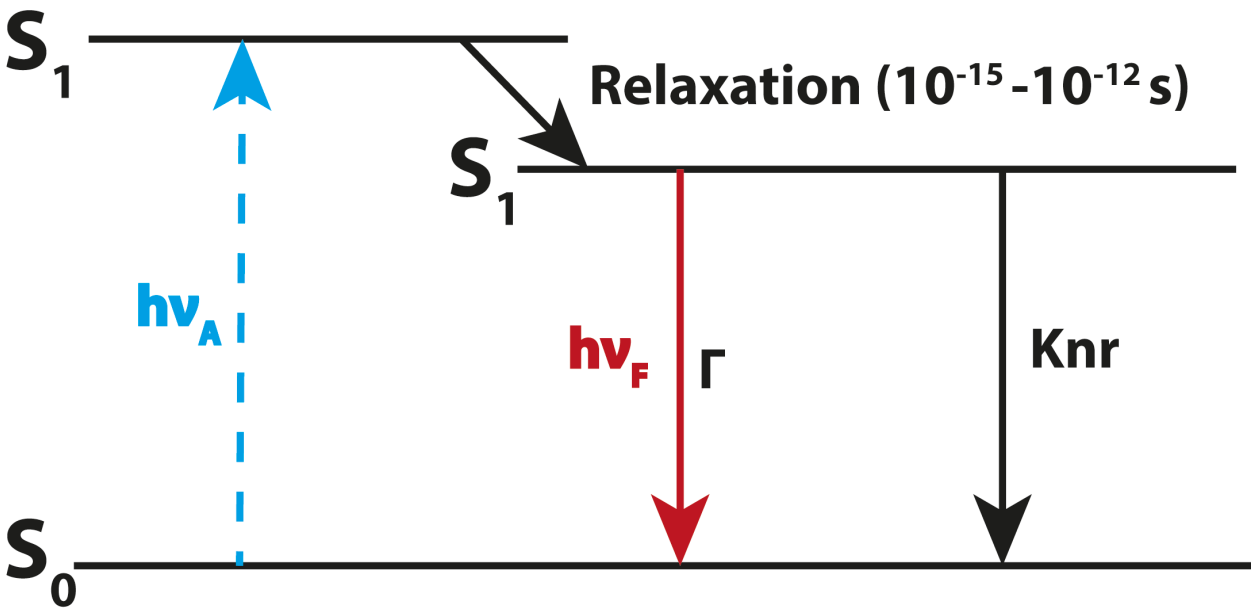


Figure 2.10. A simplified Jablonski diagram to demonstrate the physical meaning of lifetime and quantum yield

the processes involved to relax to ground state from the excited $S_1$ state. Hence, we are more interested in the emissive rate of the fluorophore ($\Gamma$) and its non-radiative decay to $S_0$ (Knr). Depopulation of the excited state occurs by both $\Gamma$ and Knr. Moreover, one can represent quantum yield as number of photons that relaxed to ground state via the radiative channel:

$$QY = \frac{\Gamma}{\Gamma + \mathrm{Knr}} \tag{2.26}$$

From equation 2.26, the QY can approach unity if the non-radiative rate is much smaller than the radiative counter part i.e. $\mathrm{Knr} < \Gamma$. However, the energy yield in fluorescence is always less than unity due to the Stokes shift. The nonradiative decay processes can be of several types. Here, we represent Knr as overall non-radiative rate constant. The excited state lifetime is defined as average

time the molecule spend in the excited state before it relaxes to the ground state. For the fluorophore represented in figure 2.10 the lifetime is given by

$$\tau = \frac{1}{\Gamma + \mathrm{Knr}} \tag{2.27}$$

Fluorescent emission is a statistical process and the lifetime is estimated as the average time spent in the excited state for an exponential decay. For an emitter having a single exponential decay 63% of the emitted photons decayed before $t = \tau$ and remaining 37% decay after i.e. $t > \tau$. Most of the decay process follow multi-exponential decays that can be considered as a sum of individual single exponentials.

$$I(t) = \sum_{i=1}^{n} \alpha_i \exp\left(-\frac{t}{\tau_i}\right) \tag{2.28}$$

In the above expression $\tau_i$ are the decay times, $\alpha_i$ are the amplitude at time t=0 and n is number of decay channels. For multi-exponential decays, one can estimate the average lifetime of the decay process as

$$\tau_{avg} = \frac{\sum_{i=1}^{n} \alpha_i \tau_i^2}{\sum_{i=1}^{n} \alpha_i \tau_i} \tag{2.29}$$

$\tau_{avg}$ is the average lifetime of decay process.

## 2.16. Chapter Summary:

In summary, we have introduced some important properties of colloidal nanocrystals. Core-shell nanocrystals was given special emphasis due to their relevance for light emission. We discussed two fundamental CdSe based core-shell NCs i.e. CdSe/ZnS DIDs and CdSe/CdS DIRs. Optical properties such as strong excitonic confinement are prerequisite for their application in photonic devices and coupling to plasmons. We also discussed in brief the optical properties of perovskite nanocrystal. After that we introduced plasmons in general, with special discussion of surface plasmons and their properties. Then the properties of evanescent waves in the metal/dielectric interfaces were discussed. We further extended this discussion for metal/insulator/metal cases and emphasized special eigen modes for such systems. Moreover, we discussed about epsilon near zero materials and their scope in brief. With the knowledge of ENZ modes supporting radiative bulk plasmon polariton (BPP) modes, we further discussed their coupling to fluorophore both in weak and strong coupling regime. Finally, we introduced fluorescence spectroscopy as a fundamental tools for probing the optical properties of light emitters, discussing both time dependent and independent phenomena.

# Chapter 3

# Experimental Techniques, Film Fabrication and Characterization

## 3.1 Colloidal Nanocrystal Film Fabrication:

### 3.1.1. Substrate Preparation:

Glass substrates of size 1.6×1.3 $cm^2$ are dipped in a base solution made of hydrogen peroxide ($H_2O_2$) and Liquid Ammonia (33% Dil. $NH_4OH$) in 1:1 ratio. They are treated at 60°C for 1 hr. Soon after the solution is cooled down and substrates are washed in Deionized water (DI) followed by drying with dry nitrogen flow.

### 3.1.2. Spin Coating:

**CdSe/CdS Dot-in-Rod and CdSe/ZnS Dot-in-Dot Spin Coating:**
Well dispersed nanocrystal solutions of DIDs and DIRs are used in toluene. The concentration of the solution is kept at 5mg/mL. 50μL of solution are spin casted on a glass substrate at 3000 rpm for 60 seconds.

**$CsPbBr_3$ Spin Coating:**
$CsPbBr_3$ nanocrystal solutions (dispersed in toluene) of concentration 7.5mg/mL are spin coated on glass, MIM and MIMIM substrates at 2000 rpm for 60 seconds.

## 3.2. Characterization of Spin-coated Nanocrystal Film:

### 3.2.1. Film Thickness Measurement:

Thickness of the nanocrystal films are measured with Dektak profilometer. The spincoated nanocrystal films resulted in a thickness of 33± 3 nm and 25±2 nm for DIR and DID film respectively. Whereas for cesium lead bromide($CsPbBr_3$), the film thickness was 50± 5 nm.

### 3.2.2. Microscopic Analysis:

The spincoated nanocrystal films are first analyzed by optical microscopy, and then with an electron microscope. Figure 3.1a shows optical microscopic image of a spincoated nanocrystal film. The spincoated DIR film appears homogenous, and the good contrast implies a low amount

of organic residues on the film surface. Both DIR and DID film look quite homogenous without any voids as can be seen from figure 3.1b and 3.2c. We use different types of nanocrystal for various applications, exploiting their tunable emission properties. This needs optimization of the spincoating parameters for the different nanocrystal solutions. For example, in order to study Purcell effect enhancement, we deposited a thin layer of NCs film on MIM and MIMIM substrates. Figure 3.1d shows electron micrograph image of $CsPbBr_3$ nanocrystal film spincoated on a MIMIM plasmonic substrate. The film looks continuous and uniform with low amount of voids.

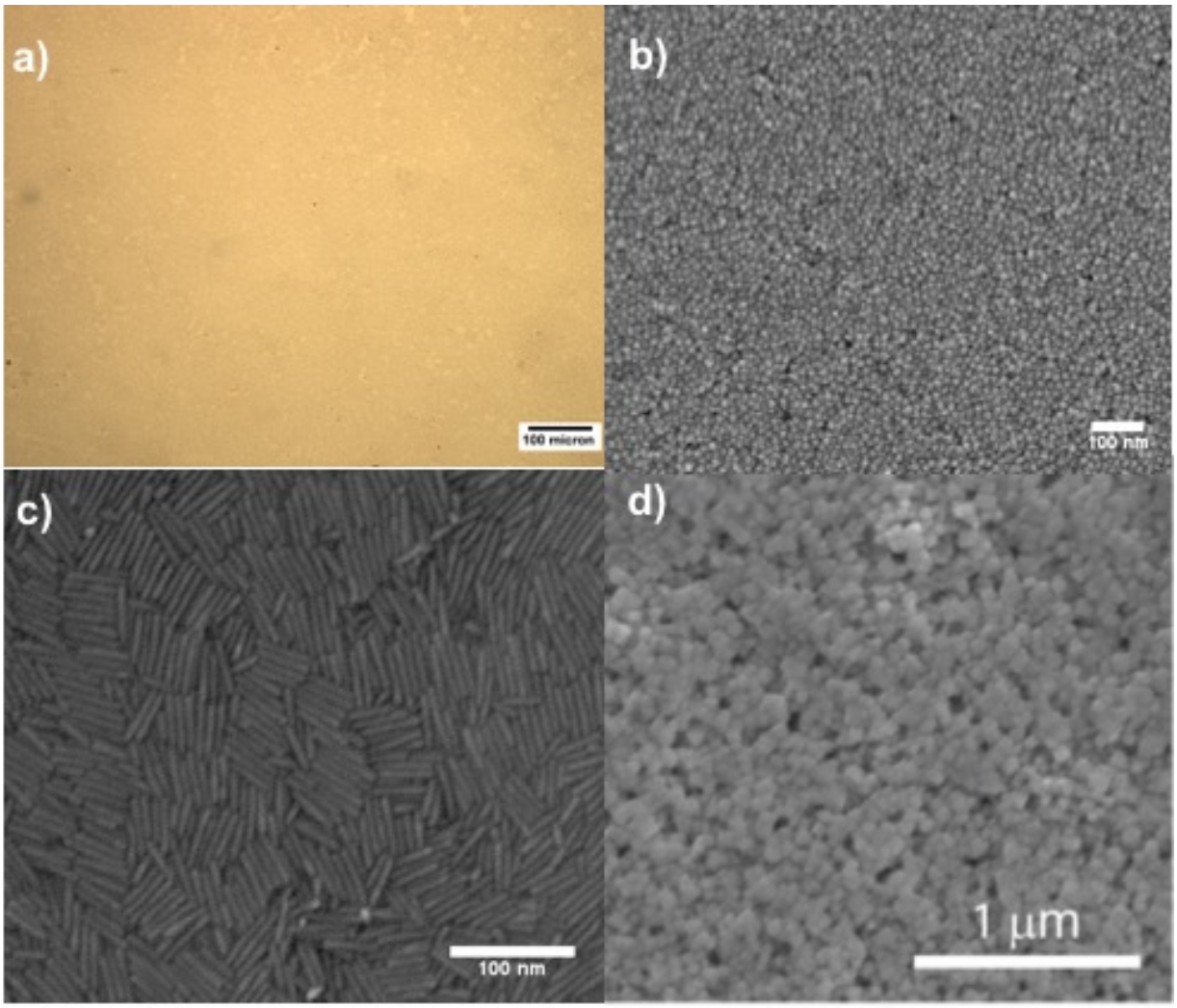


Figure 3.1 a) Optical microscopic image of spin coated DIR film at 3000 rpm (b,c) scanning electron micrograph for spin coated DID and DIR film d) scanning electron micrograph of spin coated $CsPbBr_3$ nanocrystal at 2000 rpm

## 3.3. Atomic Layer Deposition

**Atomic layer deposition** (ALD) is a thin film deposition technique that is based on the sequential use of a gas phase chemical processes. ALD is considered a subclass of chemical vapor deposition. The critical difference between a CVD process and an ALD process is that: in CVD process gases

flow continuously into the chamber which results in undesired byproducts at the end of the reaction, whereas in ALD only one gas at the time is inserted inside the chamber[64]. This allows ALD as a fundamental tool to deposit high quality materials with extremely high precision on layer thickness. ALD has found wide application in semiconductor industry, particularly in gate dielectric materials of few nanometers in CMOS technology e.g. Intel processor starting with high-k 5nm of $HfO_2$ as a dielectric material by ALD[65]. ALD can produce layers of few nanometer thickness with no porosity and can be grown at much lower temperature in comparison to CVD process. The ease of fabrication and deposition of wide range of oxides with atomic precision on almost all kind of substrates brings its importance to semiconductor and optoelectronics research and industry.

## 3.4 Working Principle

One could define ALD as a process which produces films by sequential use of self-terminating gas-solid reactions. In ALD, the reactants or precursors are injected in alternating pulses into the reaction chamber. Vapors of one reactant at a time are purged as a pulse in to the ALD chamber which allows to adsorb them on the surface of the substrate. With optimized conditions, one monolayer of each precursors adsorbs onto the surface, with a self-limiting adsorption process. The non-absorbed precursor molecules are removed by purging with inert gases.

**3.4.1 Basic Characteristics:** A typical ALD process undergoes some of the very common steps that are enlisted below

- Self-terminating reaction of the first reactant (Reactant A)
- Purging with inert gases to remove the un-reactant gases and byproducts
- Self-terminating reaction of the second reactant (Reactant B)
- Purging with inert gases

This makes one ALD cycle. Ideally after one reaction or ALD cycle one can get one monolayer of the compound. In order to get thicker films, a number of deposition cycles are needed.

### 3.4.2 Thermal ALD

As discussed above, ALD is closely related to CVD process with self-limiting access of precursors in the chamber. It based on binary reactions such as $A + B \rightarrow Product$. In case of CVD, all the reactants A and B in this case are present in the chamber at the same time. Whereas for ALD, the substrate is exposed to the A and B reactants individually, and the final product film is formed with a stepwise fashion. Therefore, an ALD process is composed of binary reactions repeated over time and can be represented as an ABABAB sequence. There are many binary reactions for ALD. For example, $TiO_2$ and ZnO are one of such kind, as shown below with its reaction enthalpies

TiO2 ALD: $TiCl_4 + 2H_2O \rightarrow TiO_2 + 4HCl$ (3.1)

$\Delta H = -16\ kCal$

ZnO ALD: $Zn(CH_2CH_3)_2 + H_2O \rightarrow ZnO + 2C_2H_6$ (3.2)

$\Delta H = -70\ kCal$

Such ALD processes have a growth per AB cycle close to 0.4 Angstrom from 150° to 600° for $TiO_2$ ALD[66] and 2.2-2.5 A° for ZnO ALD[67-68]. These ALD reactions are negative heat reactions and are quite robust in nature. These reactions are spontaneous and occur throughout a set of temperature range and are named as thermal, because they can be performed without plasma or radical assistance. The most common binary system of metal oxides is $Al_2O_3$, $TiO_2$, ZnO, $ZrO_2$, $HfO_2$ and $TaO_2$ with other common metal nitrides are TiN, TaN, $W_2N$. Also, there are some thermal ALD process available for sulfides like $MoS_2$, $W_2S$.

### 3.4.3 Plasma or Radical Enhanced ALD

There is also need for depositing single elements of metals or semiconductors using ALD along with the binary compounds. However, with thermal ALD it's very difficult to deposit single element. Fortunately, one can deposit single element using plasma or radical enhanced ALD[69]. The radicals used in this process are hydrogen radicals, which are generated by a plasma source or even by a hot tungsten filament. The schematics of plasma enhanced ALD are illustrated below.

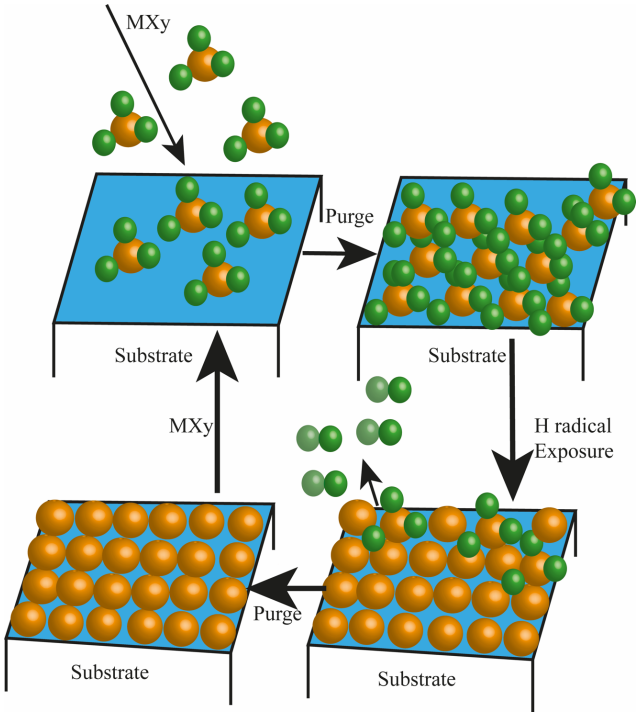


Fig3.2 Schematic diagram of hydrogen radical enhanced ALD using a metal reactant and hydrogen radicals

Ti and Ta are two very common materials that are widely studied for ALD by using hydrogen radical assisted plasma[70-71]. Here we will discuss plasma ALD processes for Ti using $H_2$ plasma.

$$Ti^{*} + TiCl_5 \rightarrow TiTiCl_5{}^{*} \quad (3.3)$$

$$TiCl_5{}^{*} + 5H\cdot \rightarrow Ti + 5HCl \quad (3.4)$$

As shown above, first $TiCl_5$ is exposed to the surface and subsequently hydrogen radicals remove the chlorine atoms and leave native Ti on the substrate with byproducts. However, there are certain limitations with radical enhanced ALD processes as the films are not conformal with high aspect ratio structures like e.g. trenches of few hundreds of nanometers[71]. ALD of single element semiconductors like Ge and Si can be deposited by means of radical enhanced ALD methods[72-74].

## 3.5 $Al_2O_3$ ALD as a Standard Model

$Al_2O_3$ deposition by ALD is a standard process used these days. $Al_2O_3$ ALD is usually performed using TMA and water as precursors[75]. Hence it is also called thermal ALD of alumina as we have discussed above.

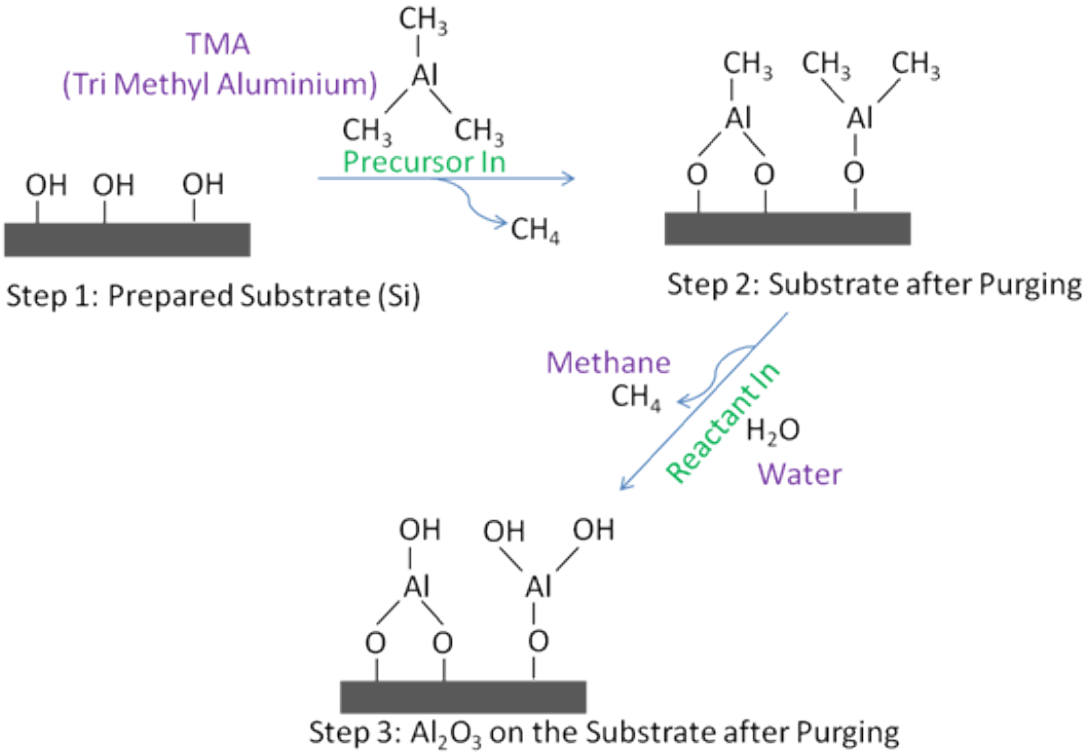


Fig 3.3 ALD of $Al_2O_3$ on a Si substrate, which is a self-terminating chemisorption of TMA of the substrate followed by ligand exchange (Image taken from dileepnanotech.com)

The overall chemical reaction occurring during alumina deposition by ALD is given by[76]

$$2Al(CH_3)_3 + 3H_2O \rightarrow Al_2O_3 + 3CH_4 \qquad (3.5)$$
$$\Delta H = -374\ kcal$$

As one can see, the enthalpy for the above reaction is very high compared to other thermal or plasma recipes in ALD. Deposition of alumina by ALD on Si substrates is shown in Figure 3.3. ALD of alumina on a silicon substrate is started with adsorption of TMA molecule on -OH terminated substrate as shown by step-2 in figure 3.3. This is called the half cycle of ALD of alumina where the methyl group (-Me) on the top shows steric hindrance behavior and prevents further adsorption of TMA molecules on the surface. Soon after this, argon gas is purged, which removes the extra amount of unreacted methyl group present in the chamber. This completes one monolayer of $-(Me)_2Al$ molecules on the surface before the next precursors enter the chamber. Then water is introduced in a pulse, which leads to a ligand exchange between -OH group and $-CH_3$ group of molecules and retains the surface as shown in step 3 of figure 3.3. Finally, a monolayer of aluminum oxide is formed on the surface. ALD of alumina depends largely on the initial state of the substrate (as in this case the substrate is coated with -OH), hence the process is self-terminating in nature. This might cause uncontrolled/random growth on the surface. This makes it necessary to observe the actual amount of material grown per cycle, which is also called as growth per cycle, "gpc", which is largely influenced by experimental conditions such as temperature and pressure in the chamber during deposition.

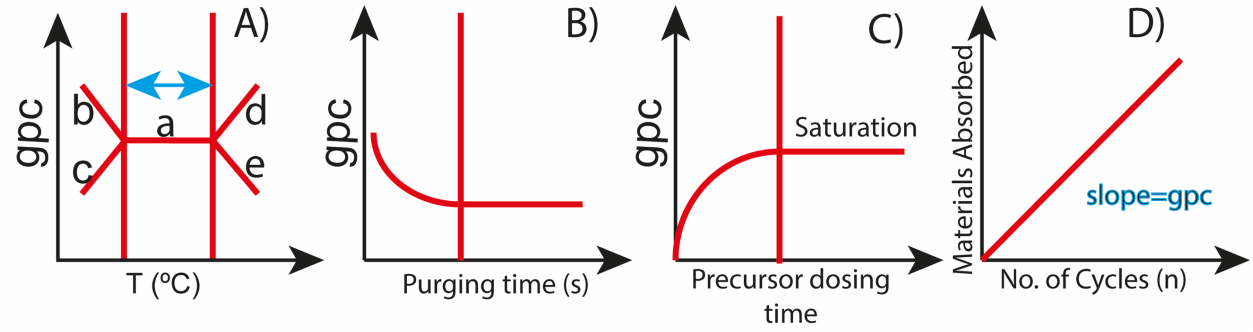


Fig. 3.4 A) variation of gpc with substrate(table) temperature (a) ALD window (b) condensation at low temperature (c) incomplete reaction at low temperature (d) decomposition of the precursors at higher temperature (e) desorption at higher temperature. B) change of gpc with purging time. C) gpc with precursor dosing time D) outcome of A, B,C results in a uniform growth over ALD cycle hence materials adsorbed are linear with ALD cycle[77]

Figure 3.4 depicts the overall variation of growth per cycle (gpc) with various parameters such as temperature, purging time and precursor pulse time for ALD of alumina. This is particularly important to define the conditions that will give rise to constant or uniform deposition rates. Figure 3.4 A) shows that for a certain temperature window the growth per cycle (gpc) is constant, which is also called the ALD window. The left side of the ALD window shows both increase and decrease of gpc at low temperature. At low temperature the reaction is not completed with the given pulse time and hence with increase of temperature the reaction rate tends to increase. This result

increases the growth per cycle (gpc) as shown in the lower branch. However, the upper branch shows a decrease in gpc with increasing temperature, which is due to the fact that adsorption and condensation of precursors occur without reacting with each other. Similarly, for the upper right side of the ALD window, the growth per cycle increases by increasing the temperature. This is due to dissociation of the ALD precursors at higher temperature, which results in more product species and the whole process resembles more CVD. On the contrary, there can also be a desorption process that occurs when the temperature of the chamber is relatively high. This results in slowing down gpc as shown by lower right part of Figure 3.4B. Gpc is also dependent on purging time. With no purging of inert gases, gpc is quite high and reduces exponentially with increase in argon purge, as it takes away the excess amount of precursors. With further increase of purging time, the gpc reaches a constant and stable value. Gpc also changes with change in precursor dosing time (amount of precursor). With more precursor in to the chamber the substrate reaches a saturation regime above which no more precursors react as shown by Figure 3.4C. With control on temperature, pressure with precursor purging time, one can optimize the amount of material adsorbed to the substrate, which varies linearly with the number of ALD cycles as shown in Figure 3.4D.

## 3.6 ALD on Colloidal Nanocrystal Films:

Colloidal semiconductor nanocrystals (NCs) can be excellent light emitters or absorbers where the optical properties as for example the light emission wavelength, direction and polarization can be controlled via the nanocrystal size, shape and composition[78-81]. This makes them very efficient materials for light emitting, lasing and other photovoltaics devices application[26, 82]. However, typically they don't show long term stability in films under ambient conditions. Surface oxidation, direct exposure of toxic materials to the surrounding environment, effects of moisture and heat are the main drawback, when it comes to working with such crystals under ambient conditions. Hence, it is desired to have a surface passivation, or insulating layer coating, over the nanocrystal layers. One way is to coat the nanocrystal films with thin layer of oxides by atomic layer deposition. There are several works on ALD on colloidal nanocrystals. Chapter 7 illustrates how ALD works on colloidal nanocrystal films and and presents a detailed investigation of its photophysical properties. Here, we will only focus on general technical part of ALD on colloidal nanocrystal films.

### 3.6.1 Plasma or Thermal ALD?

As we have discussed above, for plasma processes, radicals of particular gases are produced. The high energy plasma is found to be harmful for the ligands on the surface of the nanocrystals.[83] It can carbonize the organic ligands that passivate the nanocrystal surface, thereby reducing the photo physical properties of NCs. Hence, thermal ALD at low temperatures is preferred. Thermal ALD uses water pulses as a precursor, which is a source for oxygen for any oxide based dielectric material. Temperature of the substrate also plays a major role while working with colloidal NCs. Some of the particles are not stable at high temperature and hence a low temperature thermal ALD

is desired for such cases. Figure 3.5 illustrates the ALD on nanocrystal films, which first fills the voids, and then overcoats the film.

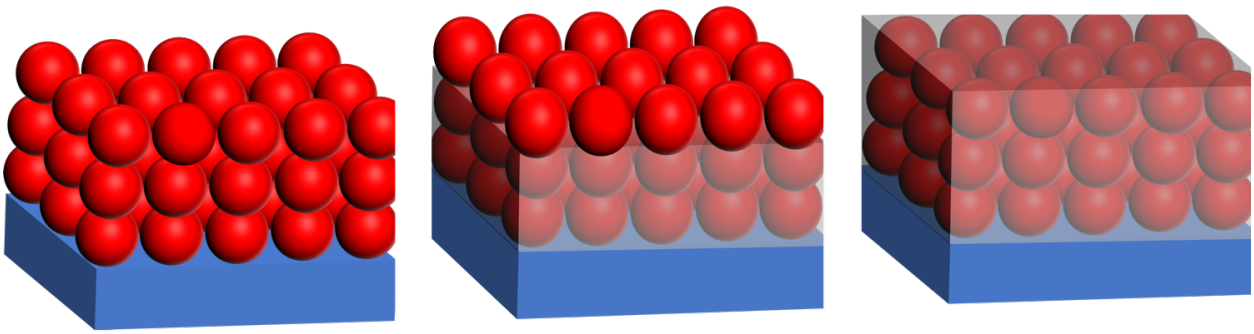


Figure 3.5 shows the process of ALD on spin-coated colloidal NCs. As we can see, the whole process goes with first infilling of NC films, followed by over-coating.

## 3.7 Atomic Layer Deposition (ALD) of $Al_2O_3$:

### 3.7.1. ALD Coating on Colloidal DID and DIR:

Atomic layer deposition was carried out in a Flexal ALD system from Oxford Instruments. The stage temperature for the process was kept constant at 110 °C. Pressure inside the chamber while purging precursors was kept at 80mTorr. The sequential purging of precursors results a deposition rate of 0.09 nm/cycle. Tri-methylaluminate (TMA) and $H_2O$ were used as precursors, and we performed a pre-heating step for 300 s before stating the ALD cycles. Each cycle consisted of a $H_2O$/purge/TMA/purge with a pulse durations of 0.075/6/0.033/2 seconds, respectively. The ALD coated NCs film are further characterized by SEM.

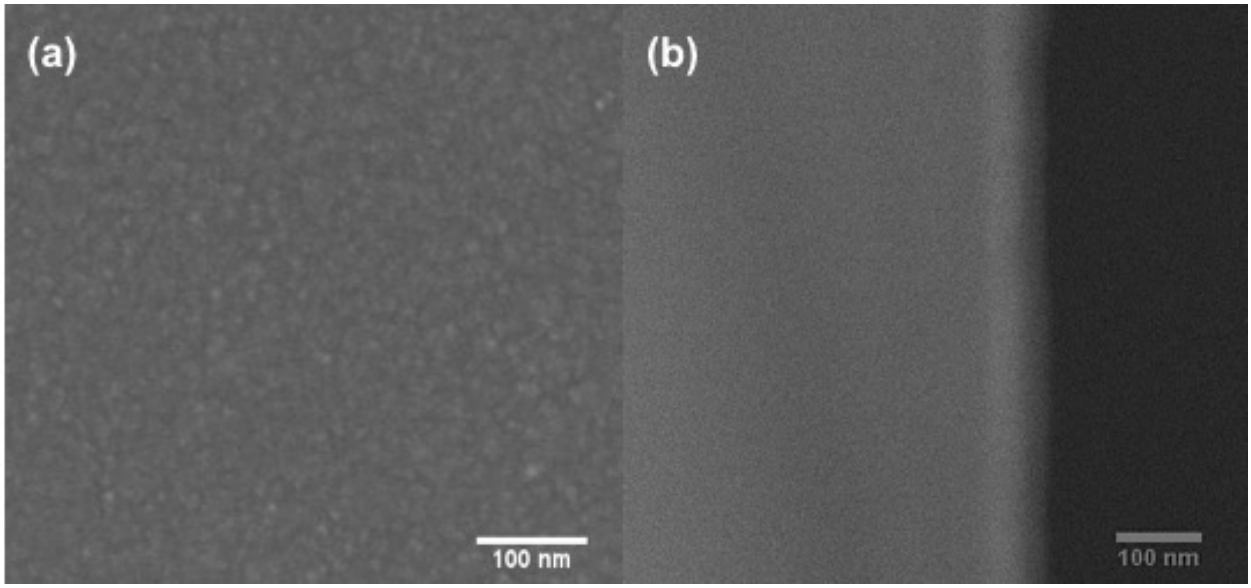

Figure 3.6 Scanning electron micrograph of a)Alumina (100cycle ALD) coated CdSe/CdS Dots-in-Rods film b) cross-section image of $Al_2O_3$/DIR film where 100 cycle of alumina was deposited over 100 cycles

### 3.7.2. ALD for Fabrication of MIM and MIMIM Cavities:

Atomic layer deposition plays an important role for deposition of oxides and nitrides with sub nanometer precision. Here we used ALD to deposit oxide layers for designing metal/insulator nanocavities. Silver has been deposited using e-beam evaporation as discussed below. Before bringing the substrates into the ALD chamber, around 25 nm of alumina were deposited using e-beam evaporator in order to avoid oxidation and etching of silver layer. It has been observed that both high energy plasma and water precursors, when in direct contact with metals, either etch the metal or oxidize it. In order to avoid such problem, one needs to either reduce the plasma power or shorten the water pulse time. However, both of these affect the deposition rate of the oxide dramatically. Hence, we deposited 25 nm of alumina layer on the top of silver prior to ALD deposition. We followed the same deposition technique for alumina deposition as illustrated above. After depositing the required thickness of the oxide layer by ALD, samples are transferred back to the e-beam evaporator to deposit the second silver layer in order to complete full MIM nanocavity. Similarly, multilayer metal/insulator cavities are fabricated using the same process again.

## 3.8. Embedding Nanocrystal Layers Inside MIM and MIMIM Cavities:

Above we have discussed the processes involved in fabrication of metal/insulator nanocavities. However, embedding colloidal nanocrystals inside the cavity is not a straight forward process as the cavity resonance has to be tuned to the nanocrystal emission wavelength. In order to achieve that, we followed a step by step fabrication process. First around 30nm of silver was deposited by e-beam evaporator with 25nm of thermal alumina on the top. The sample has been analyzed using ellipsometry and the thickness of the films was verified. We simulated the MIM and MIMIM

structure with MATLAB. The results infer that in order to match the second resonance peak of MIMIM with the emission wavelength of DID NCs, one needs to fabricate a symmetric MIM or MIMIM cavities, where the dielectric layer thickness should be around 125 nm. In order to achieve this, we coated 25 nm of $Al_2O_3$ layer by ALD on the top of MI structure made of 30 nm of Ag and 25 nm of $Al_2O_3$. After that, a thin layer of DID NCs are spin coated over it at 3000 rpm as explained above. The sample was brought to the ALD chamber and 50 nm of $Al_2O_3$ layer are deposited on the top by thermal ALD process at 110°C. This results in a configuration where a DID NCs layer has been sandwiched between the alumina layers. After this, the sample was brought to the e-beam chamber and 30 nm of silver was deposited on the top. This completes one full MIM, where the insulator is filled with layer of DID NCs. The whole structure was analyzed by ellipsometry after each deposition step. Following the same process, MIMIM structures with an embedded DID layer has been fabricated. We also varied the volume fraction of NC layer to the dielectric layer in order to achieve strong coupling conditions.

## 3.9. Electron Beam Evaporation of Metal and Dielectric Layers:

Electron Beam Evaporation (e-beam evaporator) is a form of physical vapor deposition technique in which the target material to be used as a coating, is bombarded with an electron beam from a charged tungsten filament to evaporate and convert the target material from solid to gaseous state for deposition to be carried out over a given material. In a typical e-beam evaporator process one uses high energy electrons to evaporate the source or target material. Electrons, which are thermionically emitted from a hot filament and accelerated in to a source material can generate sufficiently high energy flux to evaporate the material. In our process we used 10kV of voltage with 1 A of emission current, which delivers 10 kW of energy to the material.

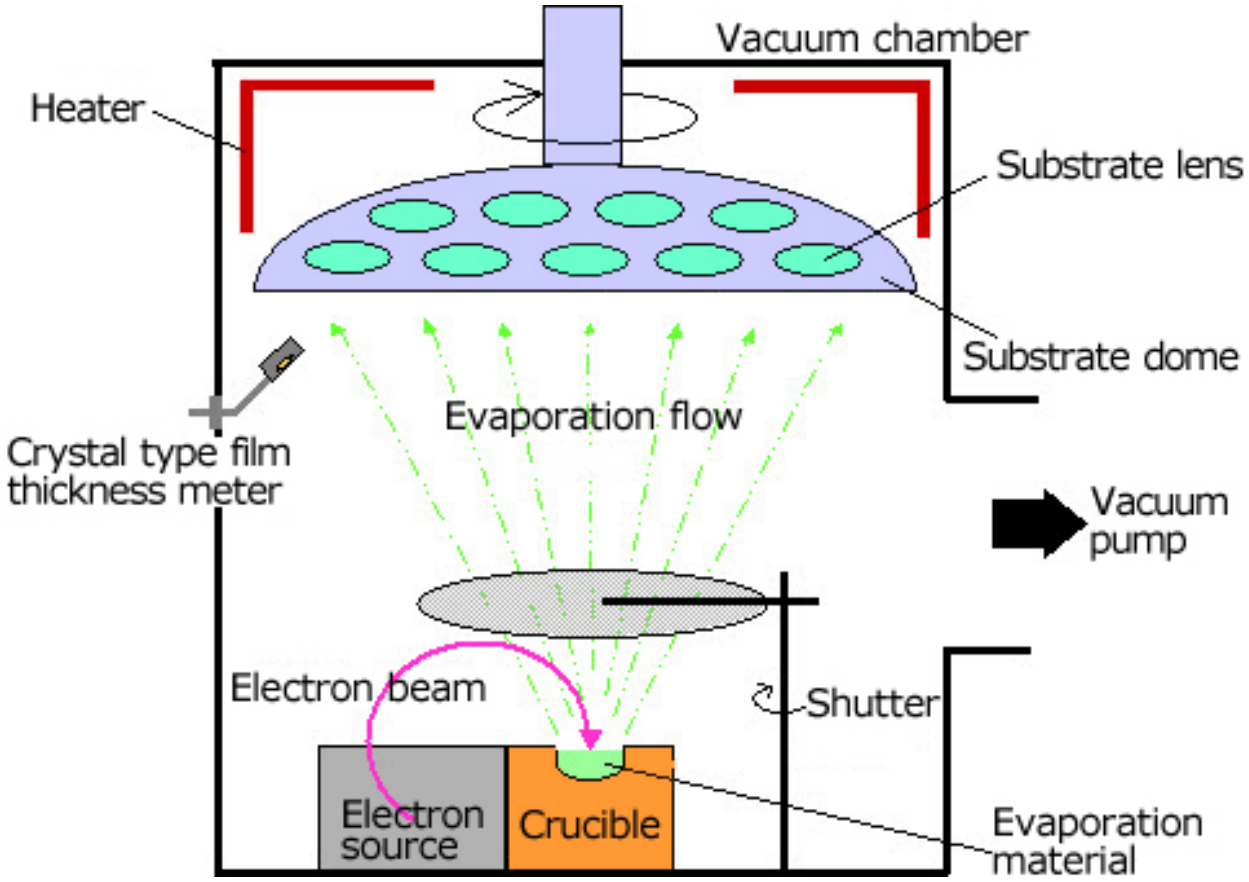


Figure 3.7 Schematics of an electron beam evaporator system (reproduced with permission from cdm-optics.com).

The path of the evaporated ions inside e-beam evaporator is controlled by the Lorentz force, which is given by sum of both its electric and magnetic components

$$F = F_E + F_B = q_e E + q_e v \times B \tag{3.6}$$

Where F is calculated in Newtons/m$^2$, $q_e$ the charge of electron measured in Coulomb, E is electric field in V/m, B in webers/m$^2$ = tesla and $v$ is the electron velocity in m/s. $F_E$, known as force due to electric field that accelerates the electron away from the filament. However, the magnetic force is balanced by the centrifugal force of the electron making a curve of radius r.

Table 3.1: Process Parameter for PVD75 E-Beam Evaporator

| Material | Deposition Rate (A/s) | PID Parameters P | I | D | Accuracy (in %) | Max.Power (in %) |
|---|---|---|---|---|---|---|
| Ag | 0.4 | 20 | 0.9 | 0.00 | 10 | 50 |
| Au | 0.3 | 50 | 0.9 | 0.05 | 5 | 50 |
| $Al_2O_3$ | 0.3 | 25 | 0.9 | 0.00 | 10 | 50 |
| $SiO_2$ | 0.3 | 25 | 0.9 | 0.00 | 20 | 100 |

## 3.10 Chapter Summary:

In this Chapter we have discussed steps involved in fabrication of homogenous films of different nanocrystal materials with tunable thickness. The films are analyzed by both optical and electron microscopy. Because of continuous device miniaturization, the demand of atomic scale growth of thin films is highly desirable. In order to fulfill the needs, atomic layer deposition techniques have been developed to achieve conformal and uniform thin film with controlled thickness. ALD stands out to be very effective when coating of high aspect ratio nanostructure is concerned. Aa a model system of ALD, the deposition of Al2O3 was outlined. We also discussed thermal ALD and radical enhanced ALD processes. While carrying out an ALD process, one needs to care about the growth per cycle (gpc) in order to maintain a uniform deposition rate. We discussed in detail about the possible parameters that affect the gpc rate in a typical ALD process. Further, ALD processes on colloidal NCs film were discussed. ALD on spincoated NCs film has been performed and the composite films are characterized both optically and by SEM. We concluded that thermal ALD process are particularly suitable for surface coating over NCs film. Fabrication of subwavelength planar nanocavities is discussed in detail. We found that accurate process parameters for e-Beam evaporator processes and ALD are quite important for obtaining a precise cavity design and fine tuning the cavity thickness. MIM and MIMIM systems with desired cavity resonances were fabricated successfully. We further embedded colloidal NCs inside MIM and MIMIM cavities and tuned the cavity resonance to the emission wavelength of DID NCs to achieve maximum coupling efficiency.

# Chapter 4

## Spectroscopic Ellipsometry: A Precise and Non-destructive Technique for Thin Film Characterization

### 4.1 Introduction

Ellipsometry is a non-invasive technique that allows a thorough characterization of the optical properties of a plethora of systems, from simple thin films, to sophisticated structures. It is used since the 19th century, introduced by the pioneering work of Paul Drude. With the emergence of micro/nano electronics, interest in Ellipsometry has grown fast. Today, the range of applications in which Ellipsometry is routinely used spans from basic research in physical sciences, to semiconductor[84] and data storage solutions, displays, communication[85], biosensor[86], optical coating[87] and many more. In this work, Ellipsometry is mainly used to characterize the optical constants of simple fundamental layers as well as to retrieve the effective parameters and uncommon properties like near-zero permittivity of much more complex systems.

### 4.2 Basic Principle

Ellipsometry measures the depolarization of a source with known polarization occurring as a consequence of its interaction with matter. As such, it uses polarized light as a probe. Hence, fundamental understanding of polarization state of light is important.

#### 4.2.1 Light and Polarization

Light is an electromagnetic wave travelling in space. The oscillation direction of the electric field related to the wave in space and time is called *polarization* . Light with randomly oriented electric field oscillation, is considered unpolarized. On the contrary, when the electric field oscillation traces a well-defined shape at any point and time, it is possible to talk about *polarized* light.[88]. In figure 4.1 the x and y components of the electric field of a plane wave travelling in vacuum are illustrated. The phase difference between the two components of the electric field describes the overall polarization state of the electric field.

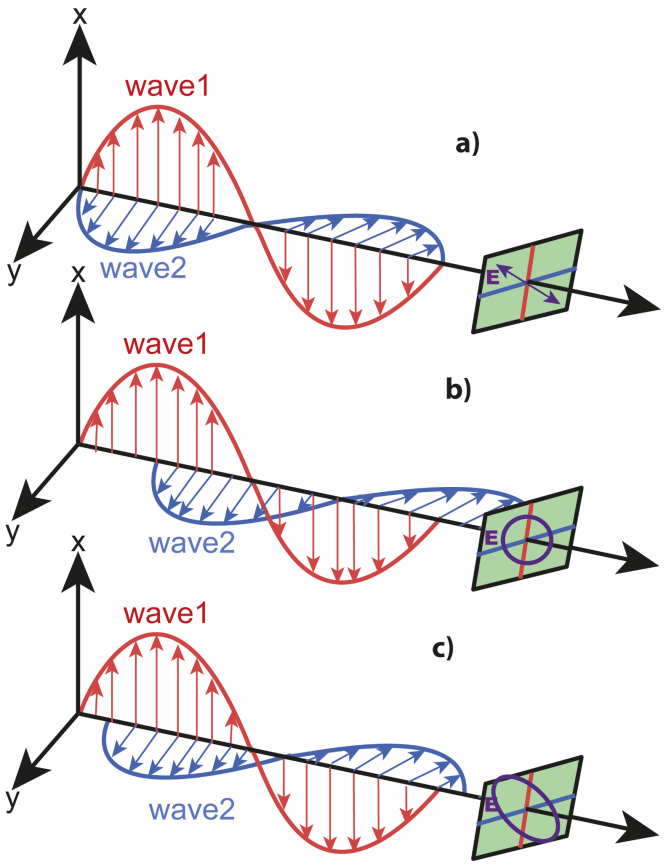


Figure 4.1 a) Linear b) Circular and c) Elliptical polarization.

There are three principal polarization state of light::

1. Linear Polarization: Phase difference equal to π.
2. Circular Polarization: Phase difference equal to π/2.
3. Elliptical Polarization: Phase difference equal to any other angle.

## 4.3 Reflectance Ellipsometry

The fundamental working principle of ellipsometry, is the analysis of the change of the polarization state of light when it is reflected by or refracted through a material. There exist several Ellipsometry techniques, but the most used is the *Reflectance/Transmittance Ellipsometry*. A typical reflectance ellipsometry measure consists in the evaluation of two quantities called the *generalized ellipsometrical angles* Ψ and Δ, by means of which it is possible to express the ratio $\rho$ between the complex Fresnel coefficients $R_p$ (p-polarized reflectance) and $R_s$ (s-polarized reflectance) as follows:

$$\rho = \frac{R_p}{R_s} = \left|\frac{R_p}{R_s}\right| e^{i(\delta_p - \delta_s)} = \tan(\Psi) e^{i\Delta} \tag{4.1}$$

Where

$$\left|\frac{R_p}{R_s}\right| = \tan(\Psi) \tag{4.2}$$

$$(\delta_{p-}\delta_s) = \Delta \tag{4.3}$$

Equation 4.2 reveals that Ψ is the angle whose tangent gives the ratio of the amplitude attenuation (or magnification) of the p-reflection with respect to the s-reflection. According to equation 4.3, Δ is the phase shift of the p-component of the polarization of the reflected beam with respect to the s-component.

A careful fit of the measured angles brings to the calculation of the optical properties (refractive index, dielectric permittivity, depolarization…) of the sample.

Usually, in order to obtain a reliable and univocal fit, the generalized angles are collected at more than one angle. Since the optical response depends also on the thickness of the samples, a complete spectroscopic analysis needs also the measure of the Transmittance to be included in the fitting process. This gives also precious information on eventual absorption bands, crucial to characterize plasmonic effects and excitonic transition.

The basic reflectance ellipsometric setup is the one shown in Figure 4.2:

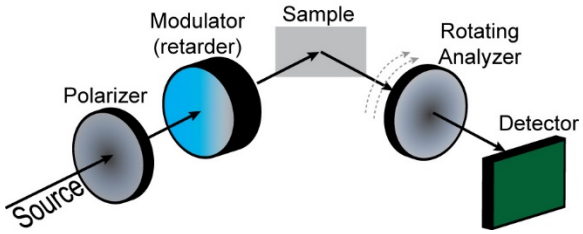


Figure 4.2 Typical reflectance Ellipsometry setup, involving a modulator in the source path and a rotating analyzer in the detecting path.

The quality of a fit can be expressed in terms of *Mean Squared Error* (MSE), that gives an accurate measure of the divergence between the fit and the original data. A fit can be considered physically meaningful if the MSE is kept reasonably below 30.

## 4.4 Glass Substrate and Metallic Thin Films

In thin films analysis, knowledge of the optical properties of the substrate is essential. For many applications simple glass is a perfect substrate, due to its transparency in the visible range that allows the acquisition of the transmittance of the thin films. Simple glass respects the well-known Cauchy dispersion and can be modeled with a single oscillator:

$$n(\lambda) = A + \frac{B}{\lambda^2} + \frac{C}{\lambda^4} \tag{4.4}$$

*A,* B and *C* are the fitting constants. It is important noticing that the Cauchy dispersion does not model the imaginary part of the refractive index and, therefore, is not necessary Kramers-Krönig consistent. However, since glass losses are reasonably negligible in the visible range, this approach is still physically meaningful and widely accepted. One way to take losses into account is expressing κ(λ) with the well-known Urbach absorbance:

$$\kappa(\lambda) = \alpha e^{1.24 \cdot \beta\left(\frac{1}{\lambda} - \frac{1}{\lambda_B}\right)} \tag{4.5}$$

Where $\lambda_b$ is the absorbance band-edge wavelength, and α and β are fitting parameters.
For the glass substrates used in this work, the parameters are the following:
Table 4.1.

| **A** | **B** | **C** | **α** | **β** | **$\lambda_b$ [nm]** |
|---|---|---|---|---|---|
| 1.5026 | 0.0088 | 0 | 2.05 x $10^{-6}$ | 6.04 | 350 |

The procedure used for the glass can be readily extended to higher index dielectrics such as $Al_2O_3$ , provided they hold a wide transparency range in the visible.
Due to its low loss and exceptional plasmonic properties, silver (Ag) has been used as a metal in all the proposed applications. Even though the optical properties of Ag in the visible can be exhaustively modelled via the well-known Drude dispersion, Ellipsometry allows a finer characterization. The model of figure 4.3 has been set up by starting from the Drude oscillator for Ag, and adding two Lorentzian oscillators to finely describe the behavior around the vanishing permittivity wavelength. Such a range is significant since it constitutes a well-studied case of natural *epsilon-near-zero* (ENZ) response occurring in Ag at 327 nm, known as Ferrel-Berreman mode. The contribution to the overall dielectric permittivity given by the Lorenzian oscillators is defined by the general formula:

$$\tilde{\varepsilon}_j(E) = \frac{\alpha_j E_0}{E_0^2 - E^2 - i\beta_j E} \tag{4.6}$$

Table 4.2.

| Oscillator | α | β | $E_0$(eV) |
|---|---|---|---|
| 1 | 0.298 | 0.188 | 3.607 |
| 2 | 0.388 | 0.406 | 3.325 |

The fit is very good (MSE=2.28) and the model is highly accurate especially in the ENZ range.

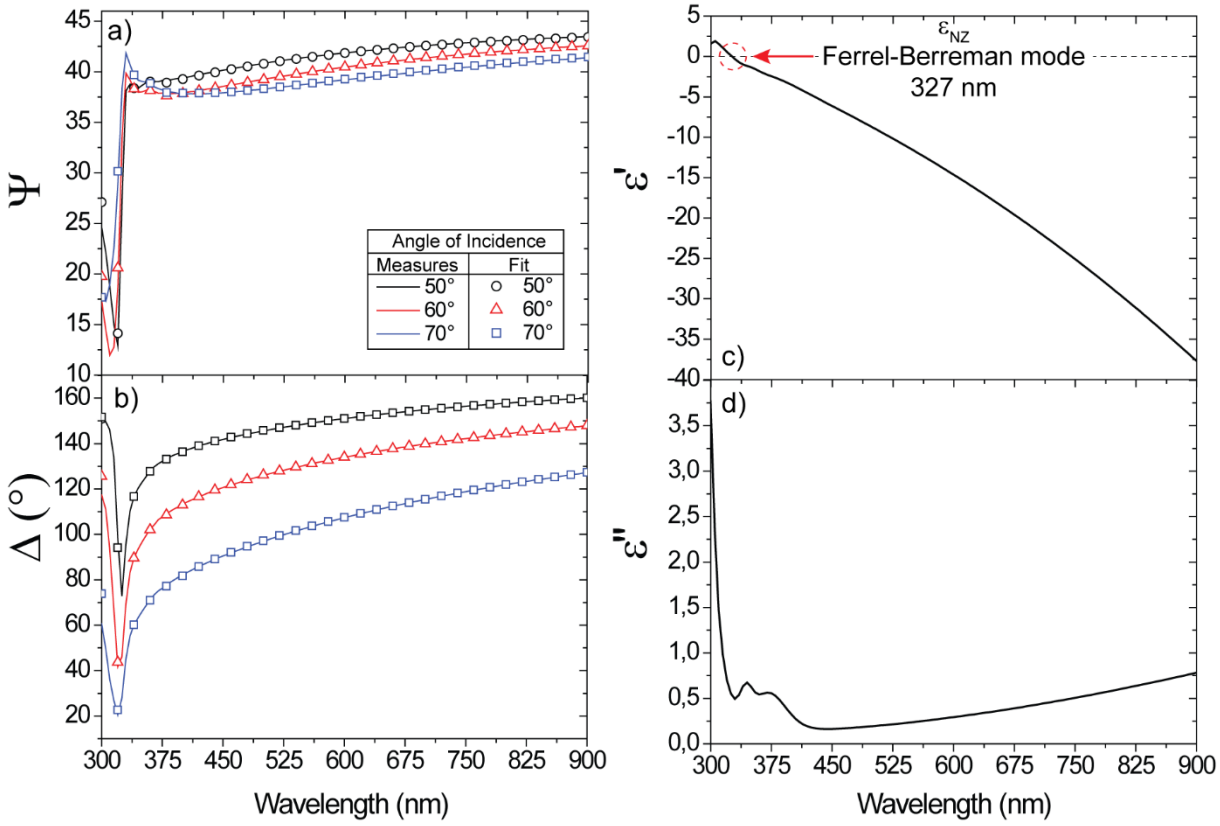


Figure 4.3 (a,b) Demonstrate measured $\psi$ and $\Delta$ at three different incident angle for 30nm of Ag layer (c,d) variation of real and imaginary part of dielectric constant of Ag layer

## 4.5 Dot-in-dot Nanocrystals

Colloidal quantum dots play a significant role in this thesis since their stability and flexibility makes them the material of election for the investigation of light-matter interaction in the considered nano-structures. Retrieving their refractive index is then crucial for the design of suitable metal/dielectric nano-cavities. Moreover, many properties can be evaluated via direct measure of their dielectric permittivity. As will be deepened in the dedicated chapter, the imaginary part of the complex dielectric permittivity of fluorescent materials gives information on the energy and strength of all the dipolar transitions occurring in the material, allowing a fine determination of their band structure. Figure 4.4a,b show the measured and fitted $\Psi$ and $\Delta$ for a 23 nm film of CdSe/ZnS Dot-in-dot (DID) colloidal quantum dots (QDs) used in Chapter 8 . A very good MSE (~ 16) is obtained, confirming the validity of the fit. Obtaining a good fit for absorbing materials like most of the fluorophores are is not simple and requires a dedicated approach. The technique adopted in this case can be summarized as follows:

1. Determination of the transparency range of the material. For this QD, a good choice is starting the fit from 800 nm, sufficiently far from the excitonic transition and emission wavelength. This allows a fine determination of the thickness of the film and sets a good starting point for the evaluation of the real part of the dielectric permittivity.

2. Proceeding with a *point-by-point* fit. Once the thickness of the film and its real permittivity are determined with suitable precision in a sufficiently large portion of the transparency range, the *point-by-point* algorithm allows for a wavelength-by-wavelength retrospective calculation of the refractive index values towards the visible range. Such a procedure has the great advantage of detecting the small features of the measured value of Ψ and Δ (like the excitonic transitions in QDs) but, as a drawback, it does not enforce Kramers-Krönig consistency.
3. Fit of the *point-by-point* obtained refractive index values via classic Kramers-Krönig consistent oscillators.

Figure 4.4c,d shows the real and imaginary part of the dielectric permittivity of the considered QDs. The oscillators by which the model is composed are:

a. **Cauchy+Urbach absorbance tail**: Models the real refractive index of the QD in the transparency range. Even though it is not necessary Kramers-Krönig consistent, it gives physically meaningful information for dielectrics, as explained before.
   Table 4.3

| **A** | **B** | **C** | **α** | **β** | **$\lambda_b$ [nm]** |
|---|---|---|---|---|---|
| 1.6421 | 0.006006 | 0.003232 | 0.0034719 | 0 | 400 |

**b. Lorentz:**
   Table 4.4

| Oscillator | A | B | $E_0$ |
|---|---|---|---|
| Core | 0.015 | 0.199 | 2.09 |
| Shell | 0.081 | 0.507 | 2.67 |

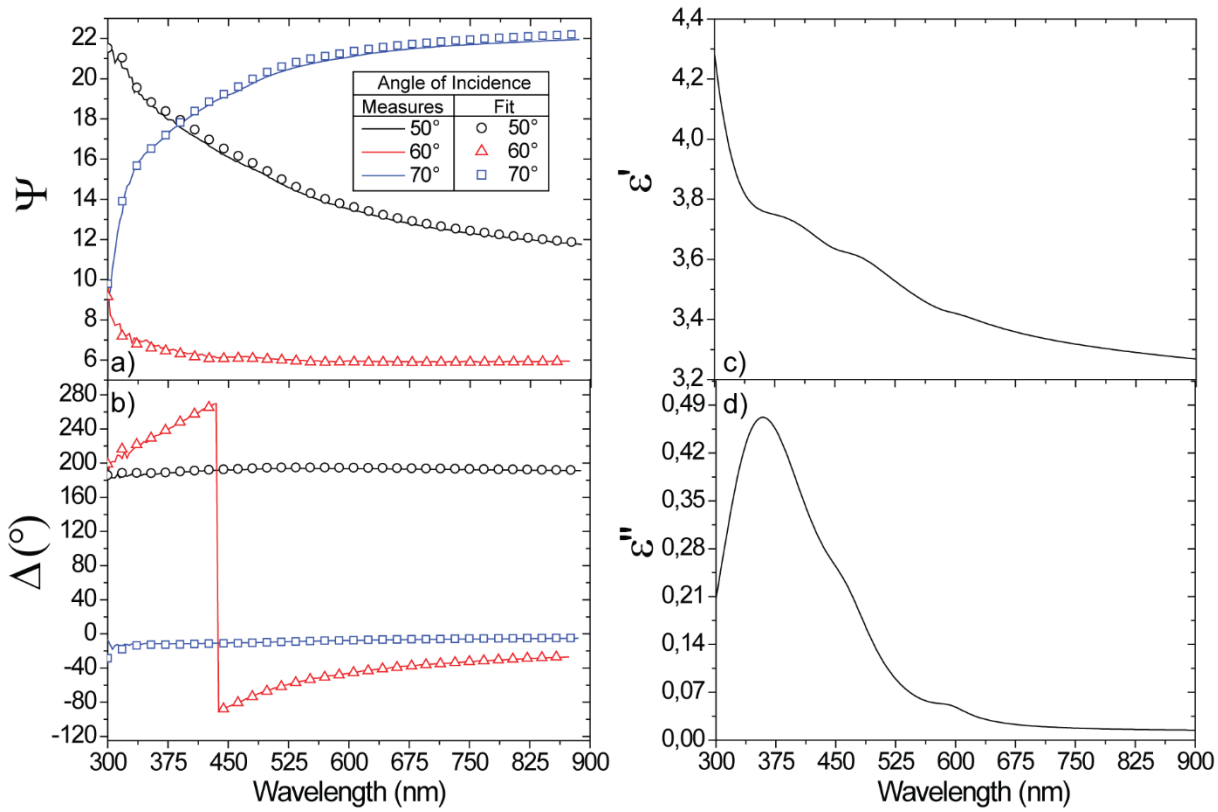


Figure 4.4 (a,b) Ellipsometrically measured $\psi$ and $\Delta$ at three different angle of incidence (c,d) Experimentally derived real ($\varepsilon'$ )and imaginary ($\varepsilon''$) part of dielectric constant for spincoated CdSe/ZnS Dot-in-Dot nanocrystal film

## 4.6 Metal/Insulator/Metal Nano-cavities

Composite structures like metal/insulator multilayers can be analyzed through a dual point of view. On one hand Ellipsometry allows retrieving information on each single layer by which the multilayer is composed thus building a true multilayer model giving rise to the measured Ψ and Δ, on the other the multilayer can be seen as an effective unknown material characterized by the measured Ψ and Δ. This second approach allows an homogenization of the composite material that is as more valuable as much the composite structure is made of subwavelength building blocks. Metal/Dielectric/Metal multilayers made of deeply subwavelength layers fall in this case. Figure 4.5a,b show the measured and fitted Ψ and Δ for a 20/80/20/80/20 nm $Ag/Al_2O_3/Ag/Al_2O_3/Ag$ metal/insulator/metal/insulator/metal (MIMIM) multilayered nano-cavity, as sketched in the inset of Figure 4.5b. The fit shows very good MSE (~ 16) . Once more, the calculation of the effective dielectric permittivity requires a dedicated technique. Instead of constructing a multilayered model, it is possible to considered the measured Ψ and Δ as the optical response of a single unknown layer, so that its optical parameters can be calculated as follows:

1. Starting the fit from a very reflective range. Typically, for these structures the reflective range is very broad and characterized by an optical response very close to that of the metal embedded in the multilayer. This allows a fine determination of the starting refractive index

points to be considered as an *educated guess* for the *point-by-point* fit to be carried out in Step 2.

2. A *point-by-point* fit of the complex refractive index from the reflectance range (typically red-NIR range) towards the absorbance range occurring in the visible is carried out.
3. A Kramers-Krönig consistent fit of the complex refractive index as calculated in Step 2, via classic oscillators.

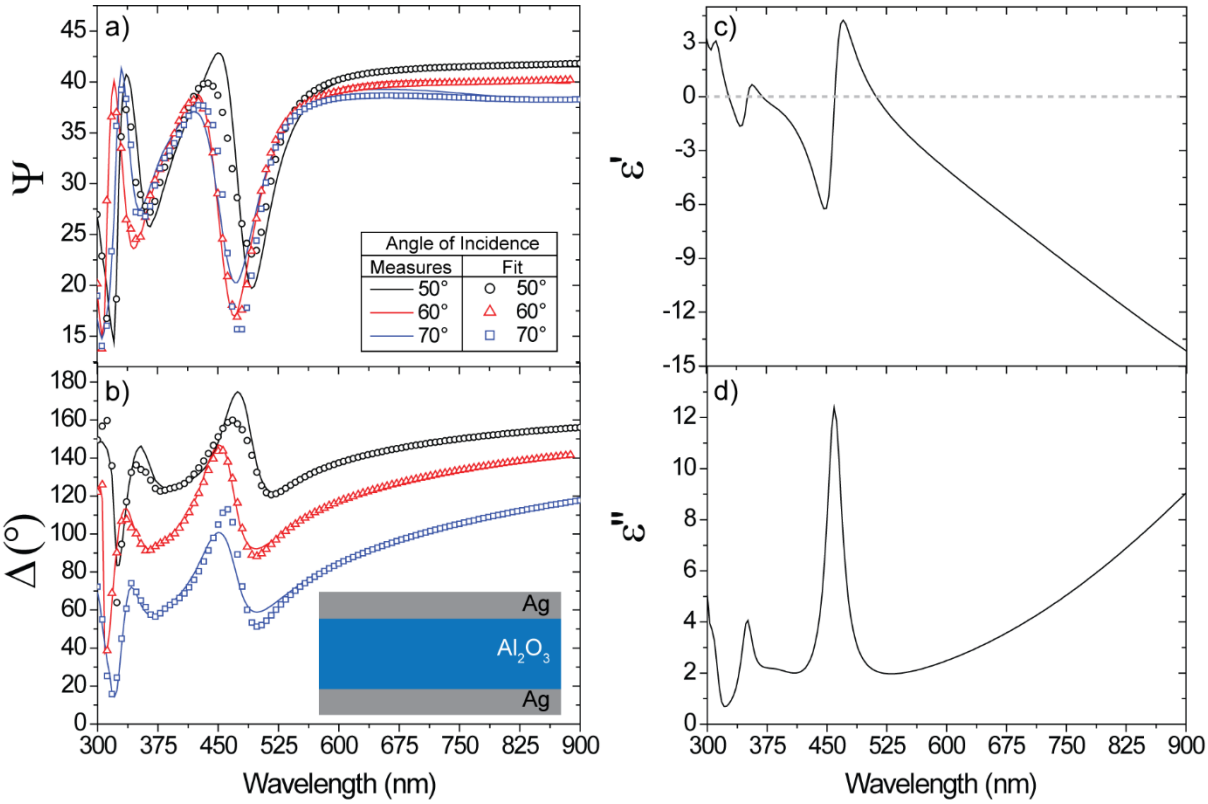


Figure 4.5 (a,b) Ellipsometrically measured $\psi$ and $\Delta$ at three different angular incidence (c,d) experimentally measured real ($\varepsilon'$ )and imaginary ($\varepsilon^{"}$) part of dielectric constant for metal/insulator multilayer MIMIM system consisting of Ag (20nm) and $Al_2O_3$(80nm) layer

In carrying out such an analysis, the number of oscillators can grow. This is due to the intrinsic asymmetry of plasmonic resonances. The used oscillators are:

Table 4.5

| **Oscillator Type** | **Use** | **α** | **B** | **$E_0$** |
|---|---|---|---|---|
| Lorentz | IR reflectance | 10.251 | 0.93558 | 1.2548 |

| | | | | |
|---|---|---|---|---|
| Lorentz | Low-Energy Resonance | 10.071 | 0.17294 | 2.6853 |
| Lorentz | High-Energy Resonance | 0.79771 | 0.11252 | 3.5825 |
| Gauss | High-Energy Resonance | 1.9535 | 0.23431 | 3.51 |
| Gauss | UV-Absorbance | 4.1167 | 0.23395 | 4.1594 |

## 4.7 Chapter Summary:

In this chapter we briefly introduce ellipsometry as a standard and non-destructive technique to characterize thin film. We described the fundamental working principle and experimental setup of reflectance Ellipsometry..Being this the technique of election for the investigation of the optical response of the considered systems, we provided several examples, illustrating how Ellipsometry can be adopted to characterize the optical response of very standard materials (thin films of noble metals) as well as new generation fluorophores and more complicated plasmonic/photonic nano-structures.

# Chapter 5

## Resonant Tunneling and Strong Coupling of Epsilon-Near-Zero Modes in Layered Metal/Insulator Nano-Cavities

### 5.1 Abstract:

Materials with unconventional value of permittivity have been the object of intense research in last decade. For example, artificial materials with negative effective permittivity have been extensively used in many fields, including subwavelength imaging and device miniaturization. Recently there has been growing interest in the scientific community on low permittivity materials whose permittivity is less than the free space permittivity. It has been found that epsilon-near-zero (ENZ) materials possess many peculiar properties like squeezing electromagnetic waves in to very narrow channels[10], design of matched zero index materials[89], shaping the radiation pattern of a source[90], and radiative coupling to fluorophores to enhance the fluorescence[54] etc. However, naturally available ENZ materials are limited to certain wavelengths and lack tunability. In this chapter, we propose a way to engineer ENZ resonances that span the whole visible range based on Metal-Insulator-Metal nanoresonators. We propose an analytical model in the framework of quantum mechanics that allows to calculate the exact dispersion relation of bound and quasi-bound modes of the MIM nanocavities. Strong coupling between two MIM cavities is demonstrated in a MIMIM system made of two stacked MIMs. We demonstrate how one can control the coupling between the two MIMs composing the MIMIM by simply acting on the thickness of the central metal layer and of the dielectric layers.

### 5.2 Introduction:

The pursuit of natural and artificial epsilon-near-zero materials has led to interesting optical properties like supercoupling[10, 91], highly directional beaming[92], optical nanocircuits[93] and optical switches[94] etc. Near-zero dielectric permittivity, also known as Epsilon-Near-Zero (ENZ), naturally occurs, for example, in silver around 327 nm, where this metal manifests a particular feature called Ferrel-Berreman mode.[53] Apart from the naturally occurring ENZ wavelengths in noble metals, an approach for obtaining a customizable ENZ response is engineering composite conductive oxides like Indium-Tin-Oxide (ITO) and Aluminum doped Zinc Oxide (AZO). These materials possess an intrinsic ENZ behavior, which can be tuned with the help of proper doping [95-98]. However, achieving ENZ response in the whole visible range in these systems is extremely difficult. Recently, it has been experimentally demonstrated that Metal/Insulator/Metal (MIM) nanocavities manifest ENZ response at their resonant modes.[54] These structures proved to be ideal for the engineering of weak interaction with a fluorophore tuned to their ENZ mode, inducing a noticeable enhancement of the photophysical properties of the emitter placed on the top of them, as will be demonstrated in the next chapter.[54] In this chapter we demonstrate that the ENZ response

occurring in metal/insulator nanocavities can be seen as the resonant tunneling of photons impinging on MIM nanocavity at its resonance. The exact dispersion relation of the MIM for both bound and quasi-bound modes is calculated analytically in the framework of quantum mechanics, showing excellent agreement with Scattering Matrix Method (SMM) calculations and experiments. We also show how to exploit the ENZ nature of these modes to design superabsorbing nanocavities by adopting a slightly modified version of the symmetric nanoresonator. Also, for this architecture the analytical dispersion relation is calculated demonstrating very good agreement with the modes calculated by SMM simulation. Such an in-depth analysis gives the opportunity of setting-up a semi-classical approach to the study of the photonic resonant tunneling, revealing the quantum nature of the phenomenon. We also studied the coupling between two MIM cavities placed one on top of each other, thereby composing a MIMIM structure. The hybridization of the resonances, finely adjustable via controlling the central metal's thickness, gives rise to two new modes, realizing a double ENZ resonant structure.

## 5.3 Materials and Methods:

### 5.3.1 Fabrication:

The MIM and MIMIM structures have been fabricated by a multistep process that consist of deposition of (i) the metal (Ag), and (ii) the dielectric ($Al_2O_3$) layers. For (i), electron-beam induced thermal evaporation (Kurt J. Lesker PVD 75) of Ag on a glass substrate was employed to obtain a Ag layer with desired thickness, then followed by deposition of 10 nm $Al_2O_3$ inside the same system to prevent Ag from oxidation. For (ii), the $Al_2O_3$ was deposited in an atomic layer deposition (ALD) system (FlexAl from Oxford Instruments) using a thermal deposition process with a stage temperature of 110 °C, resulting in an alumina deposition rate of 0.09 nm/cycle. Tri-methylaluminate (TMA) and $H_2O$ were used as precursors. A heating step of 300 s was performed before starting the ALD cycles. Each ALD cycle consisted of a $H_2O$/purge/TMA/purge sequence with a pulse durations of 0.075/6/0.033/2 seconds, respectively.

### 5.3.2 Characterization of the MIM and MIMIM Structures:

The characterization of the optical properties of all the fabricated multilayer structures has been conducted by spectroscopic ellipsometry with a Vertical Vase ellipsometer by Woollam, in the range from 300-900 nm. Spectroscopic analysis has been carried out at three different angles (50°, 60° and 70°) with a step of 3 nm. P-Polarized reflectance and transmittance measurements have been carried via ellipsometry as well, in a broad range of angles, which comprise the case of 40° discussed in this work. The resolution for recording the spectra was 3 nm, and all spectra have been normalized to the intensity of the Xe lamp.

### 5.3.3 Modeling and Simulations:

Finite Element Method based full-field simulations have been carried out by means of COMSOL Multiphysics. As boundary conditions, appropriately swept-meshed Perfectly Matched Layers have been imposed, while the nanometric layers constituting the MIM have been meshed with a free triangular texture (2D simulation) in which the maximum element size is 2 nm. Illumination is provided by a plane wave impinging at the angle of interest via a classic internal port excitation, adjacent to the upper Perfectly Matched Layer domain. Dielectric permittivities of all the selected materials were taken from experimentally measured data. Scattering Matrix Method simulations, as well as the calculation of the Tunneling probabilities, have been conducted by means of customized MATLAB codes.

## 5.4 Results and Discussions:

### 5.4.1 Equivalence Between Stationary Schrödinger Equation and Helmholtz Equation:

Recently, an equivalence between the paraxial equation of light waves and the Schrödinger equation has been set up.[99-101] This equivalence proved precious to unveil the role of the refractive index as the "optical potential" seen by the photons. In this respect, it is possible to reinterpret the stationary Schrödinger equation for massive particles expressed in Equation 5.1 setting up an optical Schrödinger equation as shown in Equation 5.4, by choosing an optical potential *U(x)* so that the resulting wavevector is a function of the complex refractive index of the considered $j^{th}$ material in which the propagation takes place:

$$-\frac{\partial^2}{\partial x^2}\psi(x) + \frac{2m}{(\hbar)^2}[E - U(x)]\psi(x) = 0 \tag{5.1}$$

Equation 6.1 can be further reduced to

$$\frac{\partial^2}{\partial x^2}\psi(x) - \frac{8\pi^2 m}{h^2}[E - U(x)]\psi(x) = 0 \tag{5.2}$$

$$\frac{\partial^2}{\partial x^2}\psi(x) - \frac{(2\pi)^2}{\lambda^2}\frac{2m}{h^2}\lambda^2[E - U(x)]\psi(x) = 0 \tag{5.3}$$

$$\frac{\partial^2}{\partial x^2}\psi(x) - [k_0 n_j(x)]^2\psi(x) = 0 \tag{5.4}$$

Where $k_0 = \frac{2\pi}{\lambda}$ is the wavevector in vacuum, $\widetilde{n_j}(x) = \frac{\sqrt{2m(E-U(x))}}{h}\lambda = n_j(x) + ik_j(x)$ is the complex refractive index of the $j^{th}$ material whose real and imaginary part are given by $n_j(x)$ and $k_j(x)$ respectively. In this form, the "optical" Schrödinger equation naturally resembles the classic Helmholtz equation of waves. In the case of dielectric materials, the imaginary part of the refractive index is negligible, and the wavefunction *ψ(x)* assumes the typical form of a harmonic propagating wave $\psi_D(x) = Ae^{-ik_0 n_j(x)}$. On the contrary, in metals the real part of the refractive index is very small (for example, in the case of silver, *n(x)* is comprised between 0.03 and 0.06 in the whole visible range[102], but the imaginary one can be relevant, so that the wavefunction assumes

the shape of a decaying exponential in the form $\psi(x) = Ae^{-k_0 k_j x}$. It is important to notice that considering that the wavefunction in the dielectric and the metal is equal to $\psi_D(x)$and $\psi_M(x)$ respectively, implies that the wavevector is equivalent to $k_M = ik_0 k_M$for the metal and $k_D = k_0 n_D$ for dielectric. This allows avoiding the non-Hermiticity of the optical Schrödinger equation, as it would naturally be in the presence of lossy materials. These considerations can be used to analyze the light propagation in metal/dielectric nanocavities composed by subwavelength dielectric cores placed between nanometric metallic mirrors.

### 5.4.2 MIM Resonators and Finite Square Well:

Metal/Insulator/Metal (MIM) can be treated as a finite square well potential (FSWP) when the external metal thickness exceeds several times the skin depth. The dispersion relation for the FSWP is well studied.[103-104] Based on this, it is straightforward to establish an optical analogy which leads to exact dispersion relation of modes of MIM and is given by

$$\tan(k_0 n_d \frac{t_d}{2}) = \frac{\kappa_m}{n_d} \tag{5.5}$$

and the odd modes are given by;

$$-\cot(k_0 n_d \frac{t_d}{2}) = \frac{\kappa_m}{n_d} \tag{5.6}$$

Where, $k_0 n_d = \frac{2\pi}{\lambda} n_d$

These equations can be solved graphically by evaluating the crossing points between the two curves

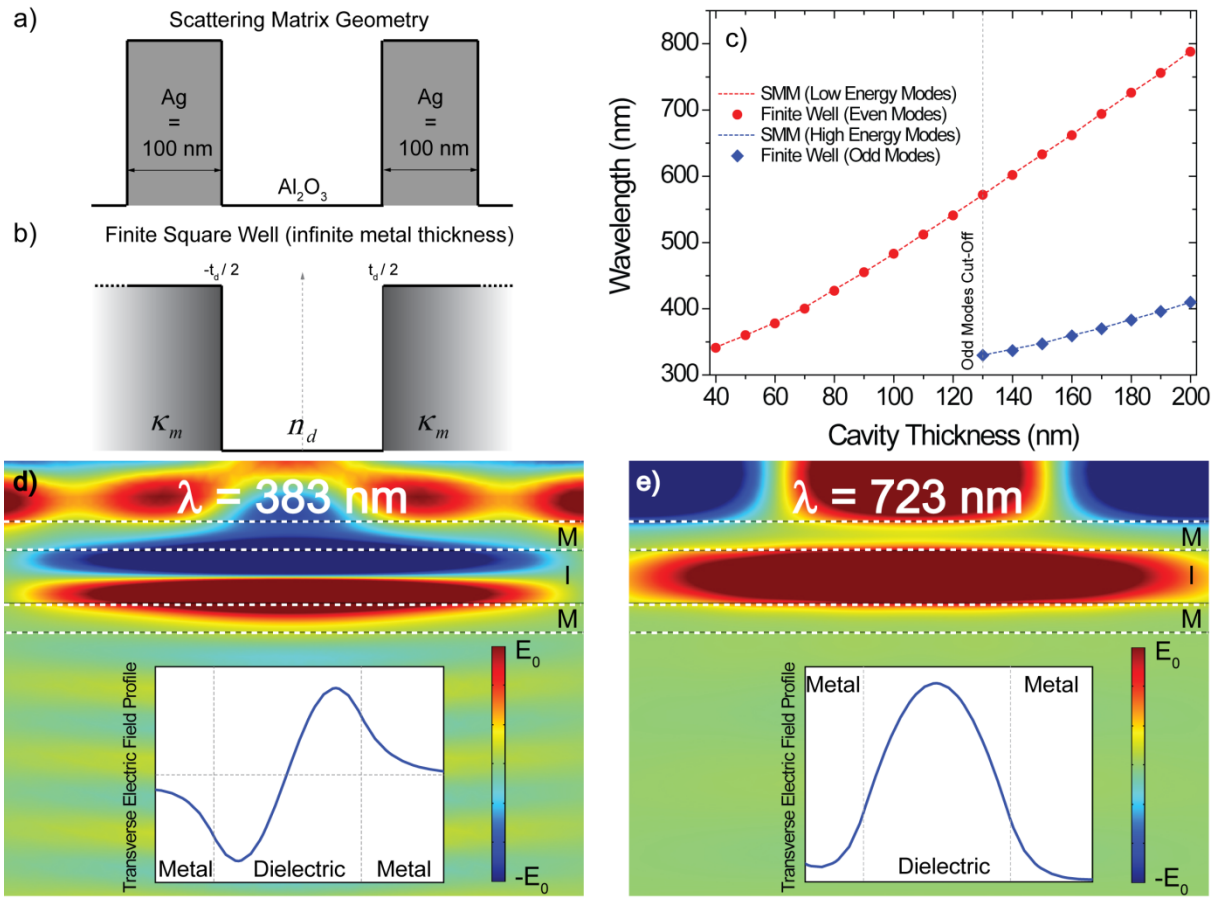


Figure 5.1: Sketch of a MIM with very thick metallic claddings of 100 nm (a) reproducing the case of a Finite Square Potential Well (FSPW) (b). (c) Modes of the FSPW calculated as a function of the thickness of the dielectric core using Equation 5.5 and Equation 5.6 compared with SMM obtained resonances (absorbance=1-Transmittance-Reflectance) of a MIM made of Ag=100nm and 40 to 200 nm thick $Al_2O_3$ dielectric core. Antisymmetric (d) and Symmetric (e) mode of an Ag=100nm and $Al_2O_3$=180nm investigated using COMSOL based Finite Element Method simulation.

Figure 5.1a gives a sketch of MIM made of 100 nm thick silver layer which acts as potential barrier for the finite square well. The imaginary part of the refractive index quantifies the height of the potential well. A classic analysis can be carried out on such system via a classic scattering matrix technique, with a monochromatic light coming from vacuum at normal incidencet impinging on the metal. In this case the modes of the MIM are evaluated as absorbance maxima calculated as 1-(Transmittance+Reflectance). An almost perfect correspondence between the peaks in absorbance calculated via Scattering Matrix Method simulations and the modes of the FPSW calculated by Equation 5.1 and Equation 5.2 is found. Very interesting is the case of the high energy odd modes which show a cutoff when the dielectric thickness is reduced so that $\tan\left(k_0 n_d \frac{t_d}{2}\right) < \frac{\kappa_m}{n_d}$. Very similar results have been obatained by Avrutsky et al. describing particular modes in MIM called Gap Plasmon Polaritons.[105] Figure 5.1.c,d show the typical field profile of the odd and even mode

respectively occurring at $\lambda_{odd}$ = 383 nm and $\lambda_{even}$ = 723 nm inherent to a MIM with Ag = 100 nm and $Al_2O_3$ = 180 nm.

## 5.5 Leaky Finite Square Well Potential and Tunneling through a MIM:

When the thickness of the two metal mirrors reduces towards the skin depth of the considered metal, the modes of the MIM shift and the simple finite potential well model cannot be used anymore. In this case, due to the leaky thin metal mirrors, the tunneling probability through them increases so that it is impossible to look for bound modes of this configuration. The key for finding the analytical dispersion for this configuration is recognizing that due to the significant tunneling probability of the photon inside the cavity, a phase component has to be added to the expression of the wavefunction inside the dielectric core which now results equal to $\Psi(x) = \cos(\kappa_0 n_d x + \phi)$, where $\phi$ is the additional phase component equal to the tunneling probability of the photon through the metal barrier. Therefore, the analytical expression for the quasi-bound modes of this configuration (named "leaky" finite square well potential) can be found starting from the previous considerations and result equal to:

$$\tan(k_0 n_d \frac{t_d}{2} + e^{-2k_0 k_m t_m}) = \frac{k_m}{n_d} \tag{5.7}$$

$$-\cot(k_0 n_d \frac{t_d}{2} + e^{-2k_0 k_m t_m}) = \frac{k_m}{n_d} \tag{5.8}$$

Equation 5.7 and Equation 5.8 correspond to the quasi-bound even and odd modes respectively for the leaky FPSW. The tunneling probability through a metal barrier of thickness $t_m$ is given by $e^{(-2k_0 k_m t_m)}$. Figure 5.2a shows the quasi-bound modes of a MIM cavity made of a fixed $Al_2O_3$ cavity of 150 nm embedded between two Ag layers, whose thickness is varied between 10 nm and 90 nm, compared with the modes of the structures calculated via SMM as maxima in absorbance (A=1-T-R). The correspondence between SMM and experiments is very good, until the thickness of the silver layer approaches values close to the percolation threshold below which it is difficult obtaining homogenous and uniform films. The case of the tunneling of a photon through a single metal barrier can be readily extended to a double barrier, as it is in the case of the complete MIM. It is well known that the tunneling probability through a double potential barrier can ideally assume unitary value, a condition known as resonant tunneling.[106-109] In reality, due to unavoidable cavity losses, the tunneling probability is never equal to one but, rather, shows a maximum in correspondence to the resonant tunneling frequency. Figure 5.2c shows the tunneling probability (dashed curves) through MIM structures composed by Ag layers of 50 nm and four different cavity thicknesses equal to (i) 50 nm, (ii) 100 nm, (iii) 150 nm, and (iv) 200 nm, compared to the transmittance calculated for the same structures via a classic Scattering Matrix Method (SMM) approach. The resonant tunneling modes correspond to the maxima of the tunneling probability curves. In Figure 5.2d-g the quasi-bound modes calculated via both exact dispersion relation and SMM as well as the resonant tunneling modes and the transmission maxima for the same MIM

structures composed by 50 nm Ag mirrors embedding an $Al_2O_3$ core whose thickness is varied between 40 nm and 200 nm are shown together. An almost exact correspondence between the quasi-bound modes, the resonant tunneling wavelengths and transmittance maxima is found, allowing to confirm that the resonant tunneling phenomenon occurs for the quasi-bound modes of the leaky MIM.

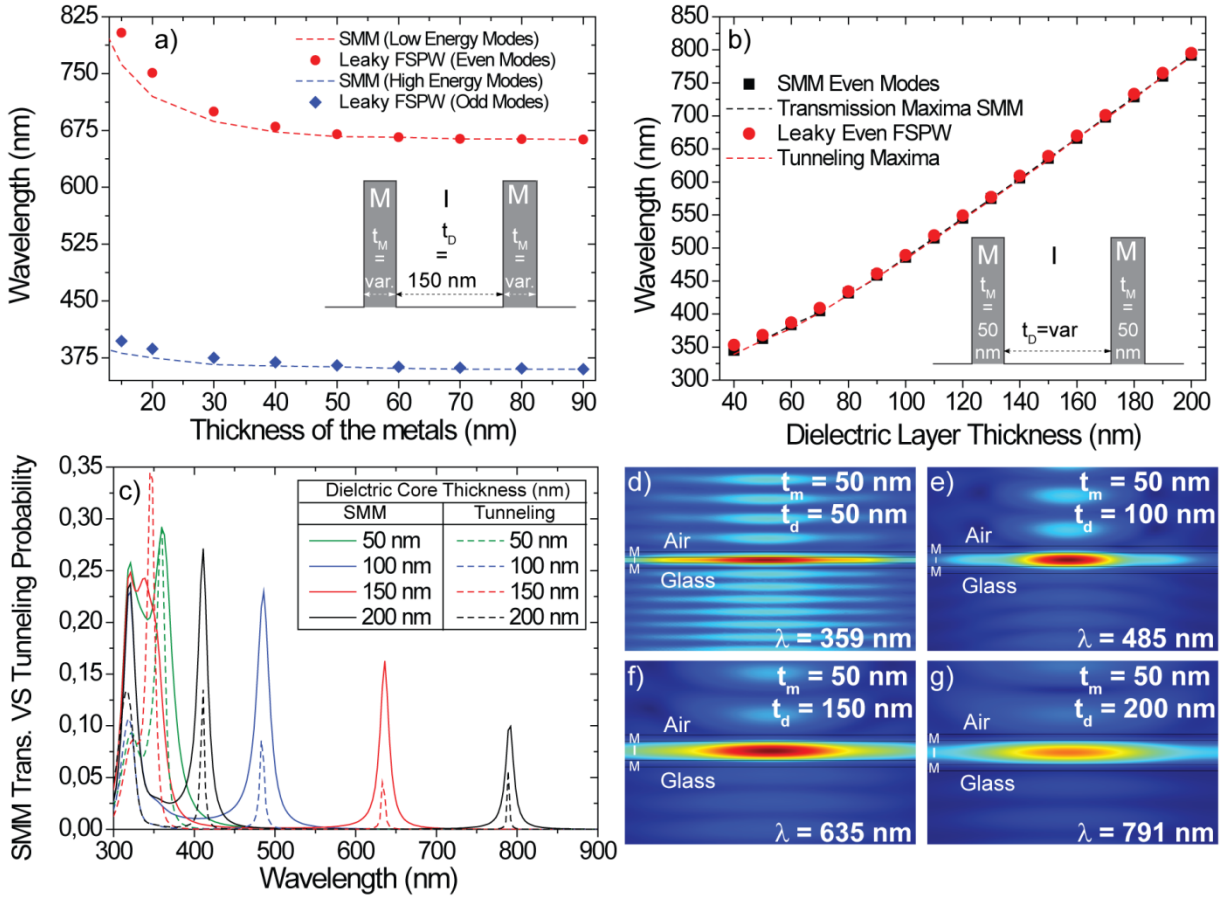


Figure 5.2: (a) Even (red circles) and odd (blue diamonds) modes of the Leaky FSPW calculated by means of Equation 5.7 and Equation 5.8 as a function of the variation of the metallic cladding thickness from $t_M$ = 8 nm to $t_M$ = 90 nm with a fixed dielectric core of 150 nm, compared with those calculated by means of SMM (absorbance=1-Transmittance-Reflectance) showing very good agreement. (b) Comparison between even modes calculated via Equation 5.7 (red spots), tunneling maxima (dashed red curve), SMM calculated even modes (black squares) and SMM calculated transmission maxima (dashed black curve), calculated as a function of the variation of the dielectric core from 40 nm to 200 nm, with fixed metallic claddings of 50 nm. The perfect correspondence between these four quantities confirms the resonant tunneling nature of the resonant modes of the MIM structure. (c) Comparison between SMM calculated transmission (solid curves) and Tunneling probability calculated, through a MIM made of 50 nm thick metallic claddings and four different dielectric core thickness equal to 50 nm, 100 nm, 150 nm and 200 nm. (d-g) 2D plot of the norm of the electric field for the tunneling (transmittance) maxima of (c), calculated via COMSOL based FEM simulations, showing the excellent light confinement performances of the MIM cavities at their resonant wavelengths.

## 5.6 Epsilon-Near-Zero Nature of the Resonant tunneling Modes and Effective Dielectric Permittivity of the MIM:

While describing a particle in a potential barrier, three important cases are usually considered: (i) the particle has energy higher than the barrier, (ii) the particle has energy lower than the barrier and (iii) the particle has energy exactly equal to the barrier. The last one is particularly interesting since, in this case, the wavefunction propagates in the potential barrier as a constant. This ideal case can be verified only in case of vanishing wavevector, resulting in a unitary tunneling coefficient, reproducing the case of the resonant tunneling described before. A similar conclusion can be drawn between tunneling of a photon in a MIM and of an electron in a double barrier. In this perspective the whole MIM can be viewed as an homogenized material with an effective dielectric permittivity $\epsilon_{eff,MIM}$ , which precisely describes the optical response of the MIM in the visible range. Hence, the resonant tunneling modes of the MIM cavity correspond to wavelengths at which the MIM behaves as an effective epsilon-near-zero material.

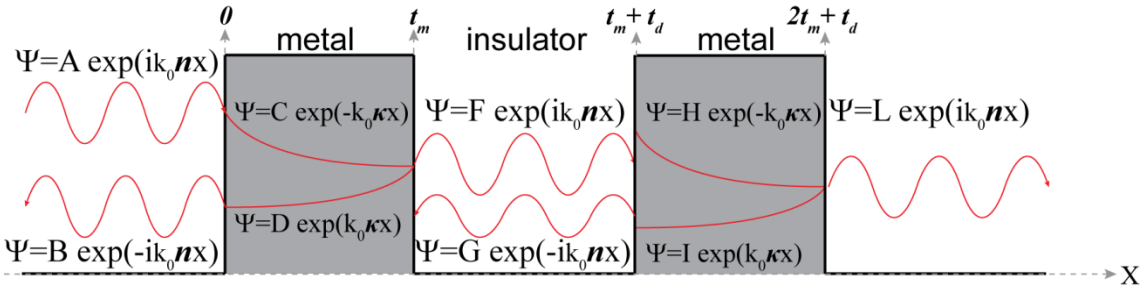


Figure 5.3 Sketch of the Resonant Tunneling through the MIM structure.

Figure 5.3 shows the sketch of the tunneling of photons in a MIM structure. In order to set up a model for the effective dielectric permittivity of the MIM, it is possible to start from the consideration that, on the contrary of its reverse "IMI" structure, in which the screening action provided by the central metal core's electrons maintains a near zero charge at the center of the waveguide,[49] a non-zero electric field at the inner metal/dielectric interfaces of the MIM can be sustained in the form of a symmetric (low-energy) and an anti-symmetric (high-energy) mode as shown in a previous section (see Figure 5.1d and 5.1e). Due to the finite thickness of the metals, the oscillation of the free electron cloud is confined in the bulk, thus introducing a restoring force as shown in Figure 5.4d. Therefore, it is possible to model the MIM as an harmonic oscillator with central frequency $\omega_{0,MIM}$. Losses introduced by both the metal and the dielectric partially convert the stored radiation energy in heat, while the nanometric size of the utilized metals drains the radiation coupled inside the cavity out of it even at the resonant frequency. This introduces a damping $\gamma_{MIM}$. Under the driving action of the electric field in the cavity, the electron cloud undergoes a collective displacement by a distance $\delta_x$. The equation of the motion, therefore, results equal to:

$$m_e^*\ddot{\delta}_x - m_e^*\gamma_{MIM}\dot{\delta}_x - m_e^*\omega_{0,MIM}^2\delta_x = -q\vec{E}(t) \quad (5.9)$$

where $m_e^* \omega_0^2 \delta_x$ is the restoring force, and $m_e^*$ is the effective mass of the electron in the cavity. The position as a function of time can be readily obtained:

$$\delta_x = -\frac{q\vec{E}(t)}{m_e^*(\omega^2 - \omega_{0,MIM}^2 - i\gamma_{MIM}\omega)} \quad (5.10)$$

The total dipole moment of the electrons inside the MIM cavity can then be expressed as:

$$\vec{P}_{MIM} = qN\delta_x(t) = -\frac{Nq^2\vec{E}(t)}{m_e^*(\omega^2 - \omega_{0,MIM}^2 - i\gamma_{MIM}\omega)} \quad (5.11)$$

The total displacement vector induced in the overall MIM cavity can then be seen as sustained by an effective permittivity $\varepsilon_{eff,MIM}$ in such a way that:

$$\vec{D}_{MIM} = \epsilon_d\vec{E}(t) + \vec{P}_{MIM} = \epsilon_d\epsilon_{eff,MIM}\vec{E}(t) \quad (5.12)$$

and we obtain a useful expression for $\epsilon_{eff,MIM}$:

$$\epsilon_{eff,MIM} = 1 - \frac{Nq^2}{m_e^*\epsilon_d(\omega^2 - \omega_{0,MIM}^2 - i\gamma_{MIM}\omega)} \quad (5.13)$$

The quantity $\omega_{MIM}^2 = \sqrt{\frac{q^2N}{m_e\epsilon_d}}$ corresponds to the strength of the oscillator at the natural frequency $\omega_{0,\,MIM}$ so that:

$$\epsilon_{eff,MIM} = 1 - \frac{\omega_{MIM}^2}{(\omega^2 - \omega_{0,MIM}^2 - i\gamma_{MIM}\omega)} \quad (5.14)$$

It has to be noticed here that, within the limit of the skin depth of the chosen metal, $\omega_{0,MIM}$ depends on the metal thickness as well as to the impinging angle, and a more sophisticated model has to be set up in order to include these effects. On the other hand, it is very useful to consider the complete MIM system as an *engineered* version of the constituent metal. In the case of Ag, this can be achieved by adding the well-known Drude model for silver to the expression in Equation 5.14:[110]

$$\epsilon_{eff,MIM} = \epsilon_\infty - \frac{\omega_P^2}{(\omega^2 + i\gamma\omega)} + \frac{\omega_{MIM}^2}{(\omega^2 - \omega_{0,MIM}^2 - i\gamma_{MIM}\omega)} \quad (5.15)$$

Equation 5.15 represents the effective permittivity of the MIM structure for even modes. One of the main advantages of this expression is that it can be readily expanded to include the odd modes, whether the dielectric core's thickness is dimensioned in order to push their cut-off frequency far enough. In the case of a pure Ag layer, the parameters are $\gamma_{Ag}$=0.021 eV and $\omega_P$=13.825 THz (corresponding to 9.1 eV) and $\varepsilon_\infty \approx 5.75$.[110-111] The $\omega_{0,MIM}$ and $\gamma_{MIM}$ can be experimentally retrieved. In this respect, ellipsometry reveals a powerful investigation tool, since it gives a direct measure of the overall dielectric permittivity of the MIM structure, allowing for a precise determination of $\omega_{0,MIM}$ and $\gamma_{MIM}$. $\omega_{MIM}$ is left as a fitting parameter and, for this case, the correspondent energy value is equal to 2.998 eV. Figure 5.4a-c shows the real case of an experimentally realized MIM structure made of two Ag layers with thickness of 30 nm and a central $Al_2O_3$ layer of 112 nm, compared with the effective permittivity modeled by means of Equation 5.15. In the experiments, p-polarized monochromatic incoherent light coming from a Xe lamp impinges on the sample at an angle of 40°. This allows to decompose the wavevector of the impinging light into two components, one parallel to the metal/dielectric interfaces (X-direction) and another perpendicular to them (Y-direction). Such a configuration allows to investigate both the plasmonic nature of the modes, induced by the Y electric field component and the symmetric

nature of the excited ENZ cavity mode, propagating in the X direction as a true waveguide mode. The fitting of the ellipsometric spectroscopic parameters Ψ and Δ gives $E_{0,MIM}$ = 2.422 eV and $\gamma_{MIM}$ = 0.063 eV (when conducting ellipsometric analysis, it is more convenient considering energy rather than angular frequency).

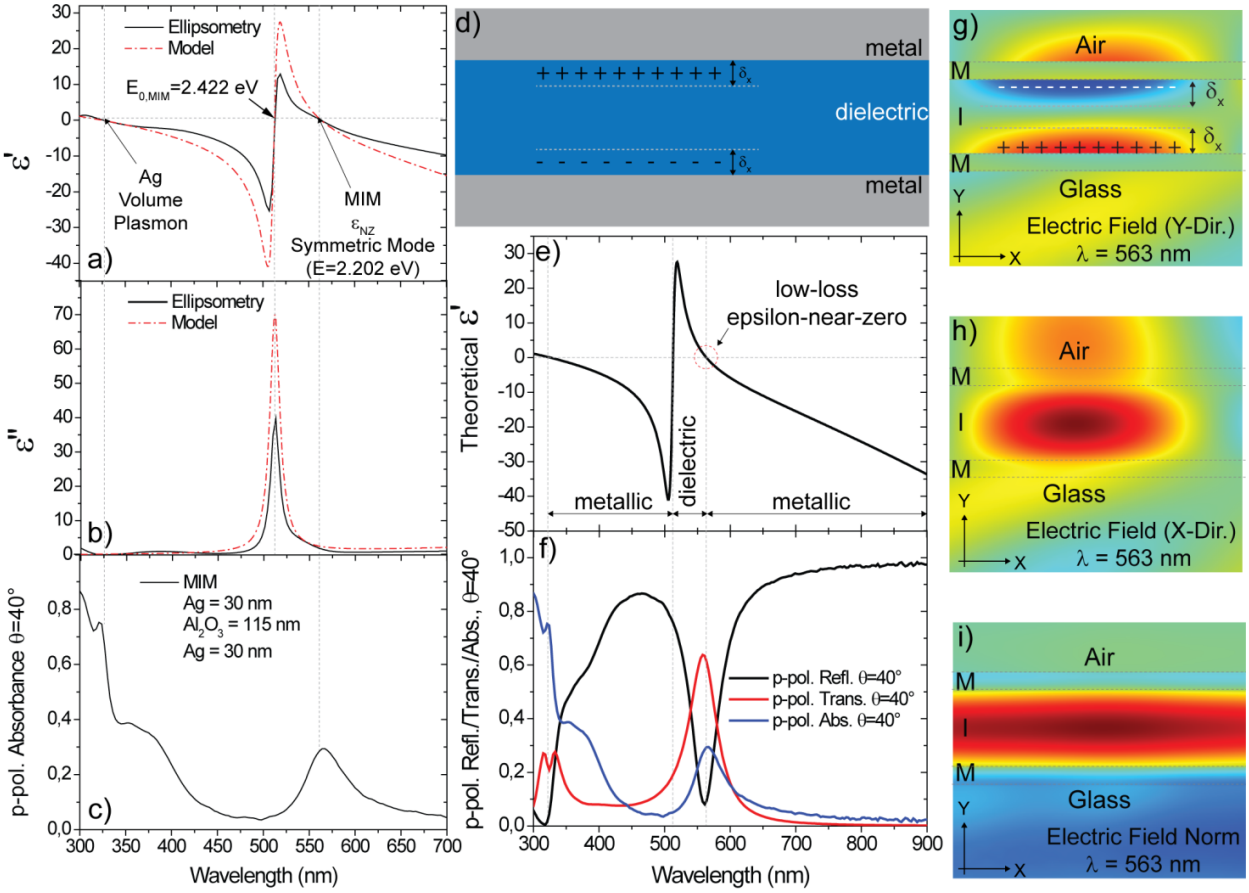


Figure 5.4: Ellipsometrically measured (black solid curves) and theoretically modeled (red dashed curves) real (a) and imaginary (b) dielectric permittivity, detected at 40°, of an experimentally fabricated MIM made of Ag = 30 nm and $Al_2O_3$ = 115 nm. The curves show exactly the same trend and a perfect agreement on the salient parameters being the Ag volume plasmon and the ENZ symmetric mode at E=2.202 eV occurring exactly at the experimentally measured absorbance maximum (c), being also the resonant tunneling mode for that precise angle. This confirms the ENZ nature of the resonant tunneling modes of the MIM nano-cavities. (d) Sketch of the proposed structure highlighting the displacement of the electrons in the dielectric core due to the presence of the electric field at the resonance, acting as a driving force. (e) Ellipsometrically measured effective dielectric permittivity as in the case of (a) in comparison with (f) Reflectance (black curve), Transmittance (red curve) and Absorbance (blue curve), measured at an angle of 40°. The measured optical response (T,R and A) showed in (f) confirm the effective metallic, dielectric and ENZ features both predicted by the effective permittivity model and experimentally measured. Vertical (g) and horizontal (h) distribution of the electric field in the analyzed MIM at the resonant wavelength, calculated at 40° via COMSOL simulations, together with the simulated norm of the electric field (i) calculated as $(Ex^2+ Ey^2)^{1/2}$.

In order to take the residual polarizability of the MIM into account, a slight modification has to be made to $\varepsilon_\infty$ increasing it from 5.75 to 6.9. As shown in Figure 5.4a, the resonance occurring at $E_{0,MIM}$ = 2.422 eV corresponds to a volume plasmon holding the typical vanishing real dielectric

permittivity. Unfortunately, due to its high lossy nature (see Figure 5.4b), it is impossible to excite it with classic transverse light. At slightly higher wavelength than $E_{0,MIM}$, however, the effective real dielectric permittivity decreases, eventually crossing the zero at $E_{ENZ,MIM}$ = 2.202 eV. The imaginary dielectric permittivity at this wavelength is sufficiently low to allow an efficient coupling of the impinging light with the MIM, resulting in a cavity-like resonance clearly measurable in both reflectance and transmittance spectra (see Figure 5.4f). Figure 5.4f shows the ellipsometrically measured Reflectance and Transmittance together with the MIM absorbance calculated as 1-(T+R), at 40°. It is worth noticing that the Transmittance and Absorbance maxima occur at almost the same wavelength, experimentally validating that the *resonant tunneling* and the *epsilon-near-zero* quasi-bound mode occur at almost the same wavelength, thus confirming the epsilon-near-zero nature of the modes of the MIM. Since the real effective dielectric permittivity of the MIM at this wavelength is zero, and the imaginary part is very low, this mode is a true epsilon-near-zero. No momentum matching technique is required to excite it. Figure 5.4e,f show a complete characterization of the dielectric properties of the MIM structure. From the proposed model, as well as from Ellipsometry, it turns out that (i) between the silver volume plasmon (3.792 eV = 327 nm) and $E_{0,MIM}$ (2.422 eV = 512 nm) and after $E_{ENZ,MIM}$ (2.202 eV = 563 nm) the MIM cavity shows a highly metallic behavior, characterized by negative dielectric permittivity, high reflectance and low transmittance. On the contrary, between $E_{0,MIM}$ and $E_{ENZ,MIM}$ the permittivity becomes positive and the MIM assumes a dielectric character, with high transmittance. At $E_{ENZ,MIM}$ the permittivity goes to zero and so happens to the reflectance leading the absorption to manifest a peak. The electric field distribution for this mode calculated by means of COMSOL based Finite Element Methods (FEM) simulations, exciting with a plane wave at a grazing angle of 40° is showed in Figure 5.4g,i. The oblique incidence allows to detect the transverse (Figure 5.4g) and longitudinal (Figure 5.4h) electric field distribution in the case of the MIM ENZ mode. This feature is perfectly consistent with the prediction given by Dionne et. al.[23] for a system made of a $SiO_2$=100nm cavity, very close to the one presented here, where it is shown that, at these frequencies, both symmetric and antisymmetric modes called *Gap Plasmon Polaritons* are allowed in the structure. This particular electric field configuration enables an effective confinement of the light in the MIM nanocavity, as shown in the calculated norm of the electric field expressed as $\sqrt{E_x^2 + E_y^2 + E_z^2}$, which takes the energy stored in the cavity into account (Figure 5.4i).

## 5.7 Super-Absorbing Epsilon-Near-Zero Modes in MIM Nano-Resonators:

The Epsilon-Near-Zero quasi-bound modes of the MIM nano-resonator can be exploited in order to engineer a MIM Super-Absorber, with absorbance values close to 100 % . In order to do this, it is sufficient to dimension the bottom Ag layer much thicker than its skin depth so that it plays the role of a back-reflector and only an exiguous number of photons can tunnel through. At the same time, the top Ag layer has to be kept thin enough to ensure high tunneling probability endowing the cavity mode with a good Q-Factor. It is calculated by ratio between the wavelength of mode to its full width half maximum (FWHM). A sketch of the system is given in the insets of Figure

5.5.a-c. In such a configuration, the electric field cannot be transmitted through the thick bottom Ag layer so that Transmittance is always very close to zero. On the other hand, in correspondence of the Epsilon-Near-Zero quasi-bound mode, the Reflectance reaches very low values, ideally vanishing. For these modes, an almost perfect confinement of the radiation is therefore achieved, thus verifying the super-absorbing conditions.

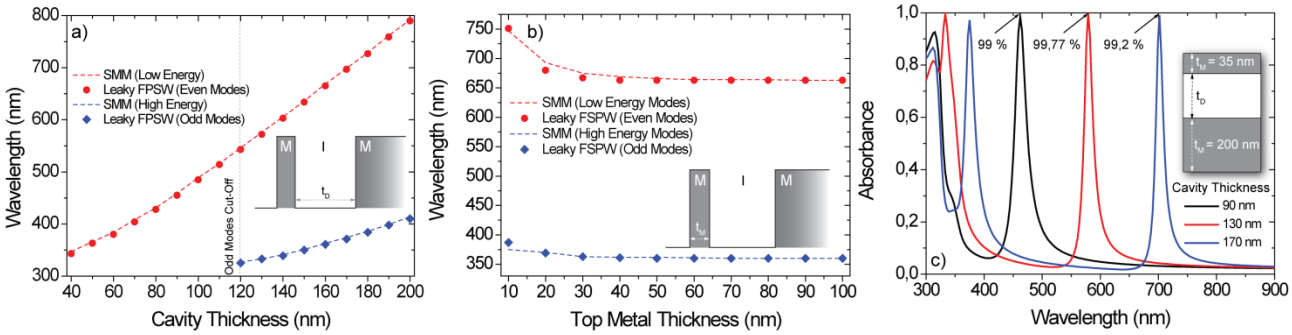


Figure 5.5: (a) Even (red circles) and odd modes (blue diamonds) calculated as a function of the variation of the dielectric core's thickness via the exact dispersion relations in Equation 5.16 and Equation 5.17, compared with the SMM calculated even (red dashed curve) and odd (blue dashed curve) modes (A=1-T-R). The superabsorber structure is made of a thin front tunneling Ag layer of 35 nm, a dielectric $Al_2O_3$ core and a Ag back-reflector of 200 nm. The agreement between SMM and analytical dispersion relation is perfect. (b) Even (red circles) and odd modes (blue diamonds) calculated as a function of the variation of the thin Ag tunneling front layer thickness via the exact dispersion relations in Equation 5.16 and Equation 5.17, compared with the SMM calculated even (red dashed curve) and odd (blue dashed curve) modes (A=1-T-R). The thickness of the dielectric core is kept fixed at 150 nm. Once more, the agreement between the analytical and the numerical solutions is perfect. (c) SMM calculated absorbance for three different superabsorbing structures as defined in (a) in which the thickness of the dielectric core is respectively equal to 90 nm (black curve), 130 nm (red curve) and 170 nm (blue curve). All the considered structures show absorbance higher than 99 %, with an outstanding peak of 99.77 % in the case of $t_D$=130nm.

Even though the symmetry of the system is broken by the thick metallic layer, it is still possible to look for an analytical expression of the quasi-bound modes of the MIM super-absorber. Since the photon tunnels twice through the potential barrier constituted by the top Ag layer, Equation 5.7 and Equation 5.8 can be modified accordingly:

$$\tan\left(k_0 n_d \frac{t_d}{2} + e^{-4k_0\kappa_m t_m}\right) = \frac{\kappa_m}{n_d} \tag{5.16}$$

$$-\cot\left(k_0 n_d \frac{t_d}{2} + e^{-4k_0\kappa_m t_m}\right) = \frac{\kappa_m}{n_d} \tag{5.17}$$

Equation 5.16 constitutes the exact dispersion relation for the even modes, while Equation 5.17 is related to the odd ones. Figure 5.5a shows a comparison between the quasi-bound modes calculated by means of Equation 5.16 and Equation 5.17 (dotted curves) and those calculated via SMM (dashed curves), for a MIM with Ag = 35 nm and $Al_2O_3$ dielectric core whose thickness is varied between 40 nm and 200 nm. The almost perfect correspondence confirms the validity of the expressions proposed in Equation 5.16 and Equation 5.17. Figure 5.5b shows the dependence of the quasi-bound ENZ modes on the thickness of the top metallic layer. The bottom Ag layer is fixed at 200 nm while the dielectric cavity thickness is 150 nm. Once more, the correspondence

between the modes calculated via SMM and the analytical dispersion relations is very good, but slightly diverges for thicknesses of the top metal layer close to its percolation threshold.

## 5.8 Epsilon-Near-Zero Resonant Tunneling Modes of the MIMIM:

When stacking a second MIM nanocavity on top of the single MIM, thereby building a MIMIM structure, the two cavities interact with a strength that is directly dependent on the thickness of the central Ag layer. Such a scenario retraces the case of two pendulums in which the two bobs are connected via a spring. The analogy can be understood considering the two MIM cavities as the two pendulums and the central metal layer shared between the two cavities as the connecting spring. The thickness of the central metal layer plays the role of the stiffness of the spring. When the central Ag layer is too thick, the interaction between the two cavities is very weak, and the two MIMs behave as two independent systems. On the other hand, if the central Ag layer is thin enough, the two nanocavities can exchange energy with an efficiency proportional to the tunneling probability through the central metal barrier. Such interaction induces a hybridization of the resonant modes of the MIMIM system, resulting in two new resonances whose energies are respectively higher and lower than the one of the original MIMs. This phenomenon is known as *strong coupling* and is typical of all the systems in which two or more oscillators are somehow connected and can efficiently exchange energy. In particular, for MIM like resonators it has already been widely investigated previously.[54] The MIMIM system is therefore characterized by two resonances holding symmetric (Figure 5.6d-f) and anti-symmetric (Figure 5.6a-c) field profiles which can be seen as, respectively, the in-phase and out-of-phase superposition of the field profile of the independent constituent MIMs. Figure 5.6a-c show the X and Y electric field profile, together with the norm of the electric field calculated for the anti-symmetric mode of a MIMIM, composed by a 30/112/30/105/30 nm alternated $Ag/Al_2O_3$ layers, while Figure 6.6d-f show the same parameters for the symmetric mode. It can be immediately seen that the propagation length of the symmetric and antisymmetric resonances in the X direction are different, as expected for these modes.[49] Moreover, the analysis of the norm of the electric field, reveals that the two resonant modes are effectively confined inside the cores of the two cavities. One of the main advantages of the model proposed in Equation 5.15 is that it can be readily extended to structures composed by multiple connected MIM cavities simply by adding additional oscillator with suitable parameters. In the case of the considered structure, the new equation is:

$$\in_{eff,MIM} = \in_{\infty} - \frac{\omega_P^2}{(\omega^2 + i\gamma\omega)} + \frac{\alpha_1 \omega_{MIM}^2}{\left(\omega^2 - \omega_{0,MIM_{-1}}^2 - i\gamma_{MIM_{-1}}\omega\right)} + \frac{\alpha_2 \omega_{MIM}^2}{\left(\omega^2 - \omega_{0,MIM_{-2}}^2 - i\gamma_{MIM_{-2}}\omega\right)} \quad (5.18)$$

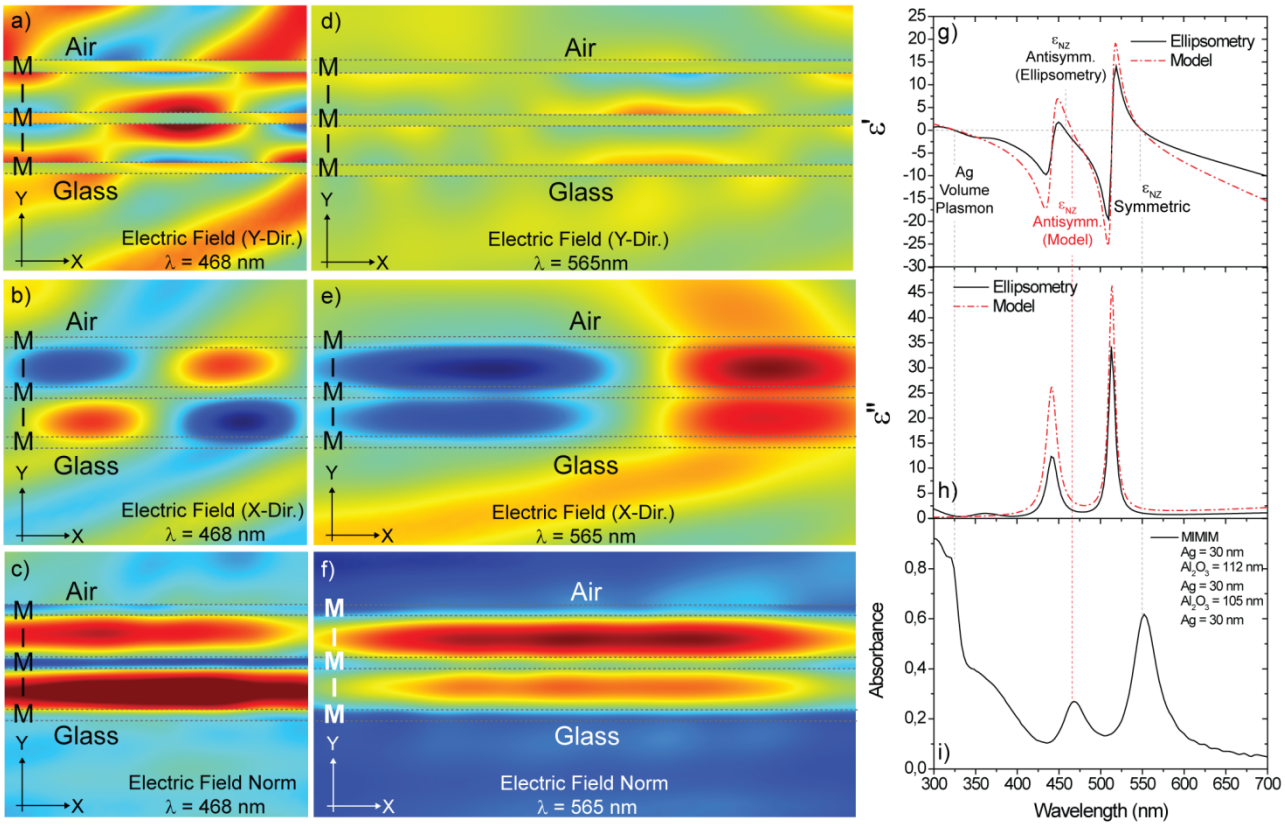


Figure 5.6: (a) Vertical and (b) horizontal component and (c) norm of the Electric Field inside a MIMIM cavity made of Ag/$Al_2O_3$ layers of 30/112/30/105/30 nm evaluated at the antisymmetric mode (λ=468nm) via COMSOL based FEM simulations. The model is excited via a monochromatic plane wave impinging at 40° angle. (d-f) Same parameters evaluated for the symmetric mode. (g) Real and (h) imaginary experimentally (black solid curve) and theoretically modeled via Equation 5.18 (red dashed curve) part of the effective dielectric permittivity for the considered MIMIM. A very good agreement is found in all the salient features (Ag volume plasmon, low and high energy ENZ modes) (i) absorbance of a MIMIM cavity made of Ag/$Al_2O_3$ layer of thickness 30/112/30/105/30 nm measured by ellipsometry

where $\gamma_{Ag}$=0.021 eV, $\varepsilon_{inf}$=6.8 eV and $\omega_P$=13.825 THz (corresponding to 9.1 eV). Once more, it is useful to consider energies rather than angular frequencies, so that $E_{0,MIM-1}$=2.452 eV, $E_{0,MIM-2}$=2.7382 eV, $\gamma_{MIM-1}$=0.075 and $\gamma_{MIM-2}$=0.07, being these last four parameters experimentally retrieved by means of Ellipsometry. Moreover, when determining the strength of each single oscillator, it is more convenient fixing the parameter $\omega^2_{MIM}$ and correct it by means of a suitable correction constant that considers the change in effective mass of the electrons in the cavities for the two different modes. The term at the numerator of each oscillator is, therefore, composed by a fixed $\omega^2_{MIM}$ and a correction coefficient $\alpha_i$ (where $i$ is the considered resonance) and, in this case, $\alpha_1$=0.35 and $\alpha_2$=0.3. Figure 5.6g,h show the real and imaginary part of the effective dielectric permittivity measured by Ellipsometry (solid black curves) and modeled by means of Equation 5.18 . Once more, the model is able to reproduce the experimental effective permittivity measured by means of Ellipsometry with very good precision. Figure 5.6i shows the ellipsometrically

measured absorbance of the considered MIMIM. As expected, two maxima are present, representing the two ENZ resonant tunneling modes of the structure. It is worth noting that the two low-loss zero crossing points of the real dielectric permittivity of the MIMIM either measured by Ellipsometry or calculated by means of Equation 5.18 correspond to the experimentally measured resonant tunneling modes detected as maxima in absorbance, thus confirming their ENZ nature.

## 5.9 Strong Coupling Demonstrated as Mode Anticrossing in the MIMIM Structures:

For a sufficiently thin central Ag layer, the plasmons in the coupled cavities can mutually exchange energy very efficiently before decaying, and strong coupling can be achieved. In this regime, a clear splitting of the two resonances occurs, generating two new $\varepsilon_{NZ}$ resonances at higher and lower energies with respect to the unpertubed modes. The splitting of two resonances determine how strongly the two modes coupled to each other and can be termed as coupling strength and can be experimentally evaluated as the energy difference between the two absorbance peaks at the center of the anticrossing. $\hbar\Omega$ is approximately twice the coupling constant g between the two systems,[112-115] that determines the coupling strength. The strong coupling regime is reached when the condition $4g^2/(\gamma_{MIM-1}\cdot\gamma_{MIM-2})>1$ is fulfilled,[112, 116] from which also the crucial importance of the damping of the unpertubed MIM $\varepsilon_{NZ}$ resonances ($\gamma_{MIM}$) can be appreciated. Moreover, it has been demonstrated that if the additional condition $g/\omega_0>0.1$ is satisfied, a regime called Ultra-Strong Coupling is achieved, for which a variety of novel phenomena have been predicted.[117-120] The distinctive signature of the strong coupling between two oscillators is the anticrossing of their hybridized energies that occurs if the frequency of one oscillator is varied across the frequency of the second one. To reproduce this scenario, five MIMIM structures have been fabricated, in which the thickness of one dielectric layer (the bottom one) was varied in the range from 60-160 nm, while the thicknesses of all other layers were kept fixed. Here the thickness of all three Ag layers was 30 nm, and the top alumina layer had a thickness of 112 nm. Figure 5.7a shows the typical anticrossing behavior of the high-energy (blue markers) and low-energy (red markers) hybridized $\varepsilon_{NZ}$ resonances in the MIMIM structures that were ellipsometrically detected as maxima in their absorption spectra. The corresponding spectra are shown in Figure 5.7b. The black markers in Figure 5.7a report the GPP energies of the corresponding MIM structures, and the grey dots give the GPP energy of the MIM with 112 nm alumina thickness. We note the excellent agreement with Scattering Matrix Method (SMM) simulations that are shown as dotted lines in Figure 5.7a.

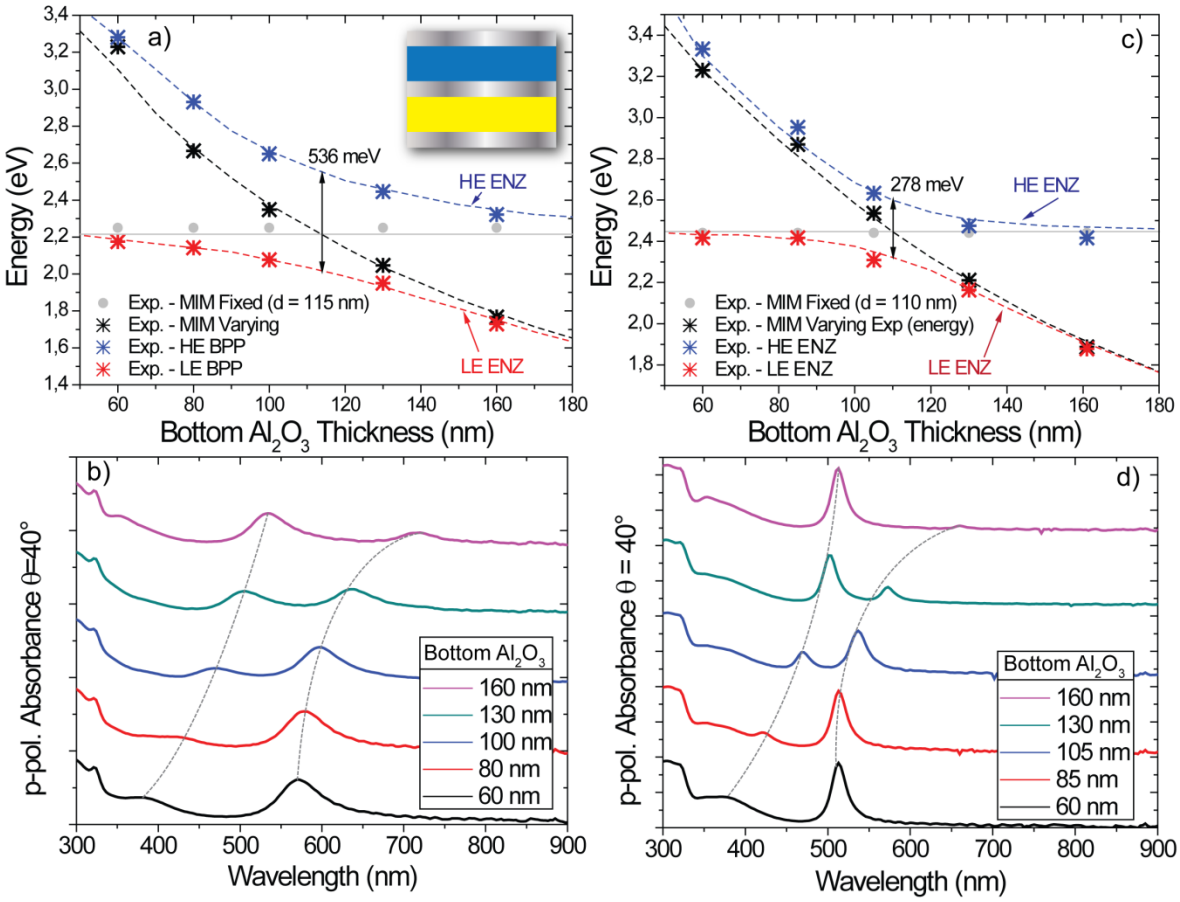


Figure 5.7. Strong Coupling and typical anticrossing of the hybridized $\varepsilon_{NZ}$ resonances: (a,c) Anticrosscing of the high-energy (blue) and low-energy (red) $\varepsilon_{NZ}$ modes in MIMIM structures where the thickness of the bottom dielectric layer was varied, while all other layers were kept fixed with two different silver thickness 20 and 30 nm. (b,d) p-pol absorbance at 40° for two metal thickness of 20 and 30 nm with varing bottom layer di-electric thickness. The thickness of the Ag metal layers and of the top dielectric were 30 nm and 112 nm, respectively.

The coupling strength in Figures 5.7a,c is 536 and 278 meV, respectively, evaluated by our simulations as the energy difference between the two resonances of the MIMIM structure at the center of the anticrossing. Figure 5.7c shows experimental and simulated data for MIMIM structures where the thickness of the metal layers is varied while the dielectric layers were kept fixed (at a thickness of 100 nm in the simulation, and close to 100 nm in the experiments). The coupling between two successive MIM can be significantly increased by reducing the thickness of the screening metal layers, and our experimental data set converges to maximum value of 536 meV corroborated with the simulations, for a thickness of the Ag layers of 20 nm. Since the damping relates to the Q factor ($Q = {}^{\omega}/_{\Delta\omega} = \omega\tau$), we see that a higher metal thickness leads to a higher Q factor, and therefore to a longer lifetime of the plasmon in the cavities. Figure 5.7d demonstrates that very narrow resonances, with $\gamma$ of around 50 meV, are achievable at the price of lower coupling strengths.

## 5.10 Chapter Summary:

In this chapter we investigated the epsilon-near-zero nature of the resonant tunneling modes of MIM nanocavities. An analytical expression has been found for the exact prediction of the ENZ resonances, providing an easy way for the engineering of customized MIMs showing ENZ features where desired in the visible range. The results we found are in excellent agreement with SMM and Finite Element Method (COMSOL) simulated structures. A quantistic insight to the physical origin of these modes has been provided, clarifying the reason why such modes can be excited without any need for momentum matching techniques. A phenomenological model for the effective permittivity of the MIM nanostructure has been provided, overcoming the well-known inaccuracies of the classic Effective Medium Theory, showing excellent agreement with experimentally fabricated structures and pinning the epsilon-near-zero nature of the described resonant modes. We also demonstrate how this model can be easily extended to describe the features of more sophisticated multiple cavities systems such as MIMIM structures. As a noticeable application, we demonstrate the possibility of realizing a customizable perfect absorber working at the ENZ resonant tunneling modes of suitably designed MIM structures. The systems we propose constitute the basic brick for completely tunable artificial ENZ materials, proposing as the fundamental technological framework for a plethora of applications like refractive index sensors and perfect absorbers, configuring at the same time as an intriguing and easy toolbox for the investigation of more sophisticated quantum scenarios.

(Note: Results presented in this chapter are under submission. My personal contribution to this work includes sample fabrication and characterization, as well as the ellipsometry analysis)

# Chapter 6

## Planar Double-Epsilon-Near-Zero Cavities for Enhancement of Spontaneous Emission and Purcell Effect

### 6.1 Abstract

Enhancing the photo-physical response of fluorophores constitutes a significant achievement towards the advance of photonic and optoelectronic technologies employing them as gain media. To this aim, the fluorophores are usually embedded in sophisticated photonic cavities or nano resonators. Such structures typically require nanoscale lithography processes, which are costly in fabrication and inadequate for implementation on large surface area. Moreover, in many cases the fluorophores are not deposited on the surface and therefore not available for the detection of biochemical reactions, for example by confocal fluorescence spectroscopy. The recent advances in the study of a promising extreme light propagation regime based on Epsilon-Near-Zero resonances, reveal extremely useful in this perspective. In this chapter, we design metal/dielectric nanocavities to be resonant with the absorption and emission bands of the employed light-emitting dyes. Using $CsPbBr_3$ perovskite nanocrystal films as emitters, we study the spontaneous emission and decay rate enhancement induced by our Double Epsilon-Near-Zero (double-ENZ) structure. We experimentally demonstrate the existence of two ENZ wavelengths occurring at the two predicted Bulk Plasmon Polariton (BPP) modes by directly measuring their dielectric permittivity via ellipsometry analysis. Finite Elements Method simulations confirm the resonant nature of these modes, demonstrating strong electric field enhancement inside the nanometric dielectric layers. We show how the double-ENZ nature of this plasmonic nanocavity can be exploited to achieve both Surface Plasmon Enhanced Absorption (SPEA) and Surface Plasmon Coupled Emission (SPCE), inducing a noticeable enhancement of both the spontaneous emission and the decay rate of the perovskite nanocrystal film placed on top of the nanocavity. Tuning the thickness of the dielectric spacer layer on the surface allows to reduce the losses induced by the metallic layers and to maximize PL and quantum yield. Finally, we discuss the possibility of tailoring the two ENZ wavelengths of this structure within the visible spectrum simply by finely designing the thickness of the two dielectric layers, which enables resonance matching with a broad variety of dyes. Our device design is appealing for many practical applications ranging from sensing to low threshold amplified spontaneous emission, because we achieve a considerable (four-fold) PL enhancement while enabling simple fluorophore deposition on a planar surface that keeps the fluorophores exposed and accessible if needed.

### 6.2 Introduction

Enhancing the spontaneous emission of a fluorophore is of great interest for a plethora of new emerging technologies spanning from optical biosensing[121], low threshold lasers [122-123] and single

photon sources.[124-126] In order to achieve such an effect many approaches have been proposed, most of which make use of an optical cavity to enhance the spontaneous emission rate of a fluorophore posed either inside or in proximity of it. Such an effect is known as *Purcell Effect*.[127-129] One of the most interesting ways to enhance the Purcell effect is to take advantage of a special propagation regime involving nanometrically confined evanescent waves rising from the *plasmonic* properties of very thin metallic films. [130-134]Generally, the mechanisms governing such a phenomenon are two: Surface Plasmon Enhanced Absorption (SPEA) [135-136]and the Surface Plasmon Coupled Emission (SPCE)[137-140]. The former is inherent to the enhancement of the absorbance of the fluorophore by means of a plasmonic absorber, while the latter refers to the possibility of improving its emission by exploiting the resonant properties of a plasmonic structure, acting as a cavity. Enhancement of the emission rate and photoluminescence by several orders of magnitude has been achieved by specifically designed nanoresonators that embed the fluorophore inside the plasmonic cavity. However, these approaches typically have two drawbacks: (i) fabrication of such structures is very demanding, and (ii) to obtain such record values the fluorophore has to be inserted at the position of highest field enhancement that extends only few nanometers in size, which might not be compatible with the size of target biomolecules, and the target molecule might not be exposed to the surface. In this respect, planar plasmonic multilayers can represent a very interesting alternative. It has been demonstrated that in a planar structure, metallic and dielectric multilayer can behave as an absorber (and as a resonant cavity) if its dielectric permittivity vanishes at a precise wavelength, manifesting a condition known as *Epsilon Near Zero* (ENZ)[10, 12, 90, 95-96, 141-143]. Here, we show how to take advantage of both the SPEA and SPCE effects by making use of a plasmonic system, whose dielectric permittivity has been specifically designed to manifest a *Double Epsilon Near Zero* (double-ENZ) behavior. The first ENZ condition, occurring at smaller wavelengths is tuned to match the absorbance band of the fluorophore posed on the top, thus inducing the enhanced absorption properties. The second ENZ wavelength is tuned on the emission peak of the fluorophore, acting as a resonator to reach the plasmon coupled enhancement of the emission. As a fluorophore, we chose perovskite $CsPbBr_3$ nanocrystals emitting in the green spectral region[144]. Perovskite crystals as emitters are a particularly appealing material system for our approach, since their emission and absorption properties can be tuned across the entire visible spectrum both by chemical composition (through anion exchange), and via quantum confinement[37, 144-148]. Furthermore perovskite emitters manifest excellent optical properties such as high quantum yield reaching almost unity, narrow emission linewidth, and negligible influence of self-absorption and Förster resonance energy transfer[149].

We demonstrate that by exploiting the SPEA and SPCE effects the spontaneous emission of the perovskite nanocrystals layer is enhanced by a factor of 4 for MIMIM with respect to their emission from a layer on the bare dielectric substrate. In order to highlight the contribution of both ENZ conditions, we present a comparison with a plasmonic structure that manifests only one ENZ regime in the absorption band of the fluorophore. For such a system, only the SPEA effect is present, which enables us to clearly separate the SPEA and SPCE contributions to the fluorophore

emission. For the single ENZ case we observe a small increase in emission (about a factor of 1.5) and only a slightly reduced decay time, while for the double-ENZ one four-fold enhancement of the emission, accompanied by a significantly shortened decay time are observed. We demonstrate experimentally and theoretically that tuning the thickness of the dielectric surface spacer layer to some tens of nanometers maximizes the PL enhancement and quantum yield.

Recently, the occurrence of the ENZ condition has been demonstrated, in particular in metal/dielectric multilayers known as *hyperbolic metamaterials*, consisting of a high number of periodically stacked subwavelength metal(M)/insulator(I) pairs[150-161]. Usually, the design of the ENZ wavelength in these systems is carried out in the framework of the Effective Medium Theory (EMT). Although the EMT is found useful for a high number of layers, it fails to predict the salient features occurring in plasmonic systems made of an finite and small number (1,2,3…) of metal/insulator cavities, like the MIM and MIMIM structures discussed here and illustrated in Figure 7.1a,b.

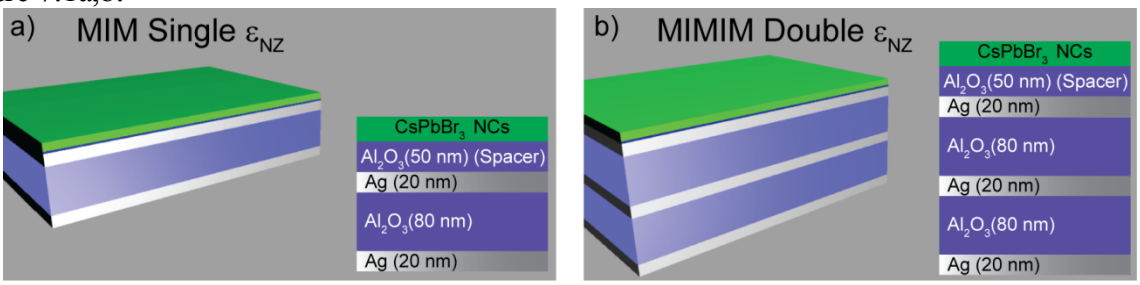


Figure 6.1. Sketches of the (a) single ENZ (MIM) and (b) double ENZ structures. A 50 nm thick $Al_2O_3$ layer has been deposited on the top of each structure as a spacer between the dye ($CsPbBr_3$ nanocrystals) and the Ag layer.

Figure 6.1b shows the double-ENZ system, consisting in a double metal/insulator (MIMIM) plasmonic cavity, in comparison with a single ENZ (MIM) one (Figure 6.1a). Ag has been chosen as a metal due to its very good plasmonic properties and low losses in the band of interest (around 500 nm wavelength), while $Al_2O_3$ has been used as a dielectric due to both its suitable refractive index and high transparency in the visible range. Scattering Matrix Method calculations allowed a precise design of the thickness of the layers that yielded 20 nm for Ag and 80 nm for $Al_2O_3$. An exhaustive description of the propagation of the light inside a MIM structure has been given by Meier [45] and for the MIMIM structure by Avrutsky et. al[105]. The MIMIM double cavity system supports four modes, of which only the two with a symmetrical field distribution persist[162]. These modes are denominated *Gap Plasmon Polaritons* (GPP) and are extremely confined inside the structure. When the number of adjacent nanocavities (intended as the number of dielectric layers sandwiched between two silver ones) increases, a mutual repulsion of these modal indices occurs. This interaction between these cavity plasmon modes induces their hybridization[163-164], thus giving rise to strongly confined bulk modes called *Bulk Plasmon Polaritons* (BPPs)[105].

## 6.3 Materials and Methods:

### 6.3.1 Fabrication of the MIM and MIMIM Structures

MIM and MIMIM multilayers have been fabricated following the procedure discussed in experimental section 5.3.1 in chaper 5.

*ALD of alumina:* Atomic layer deposition was carried out in a Flexal ALD system from Oxford Instruments, using a thermal process with a stage temperature of 110 °C, resulting in an alumina deposition rate of 0.09 nm/cycle. Tri-methylaluminate (TMA) and $H_2O$ were used as precursors, and we performed a pre-heating step for 300 s before stating the ALD cycles. Each cycle consisted of a $H_2O$/purge/TMA/purge with a pulse durations of 0.075/6/0.033/2 seconds, respectively.

### 6.3.2 Spectroscopic Ellipsometry

The optical constants and thickness of the Ag and $Al_2O_3$ single layers, as well as those ones of the MIM and MIMIM structures, have been obtained by spectroscopic ellipsometry carried out by a V-VASE ellipsometer (Woollam). Reflectance (R) and transmittance (T) spectra were ellipsometrically measured, while the absorbance (A) of the MIM and MIMIM structures has been calculated from the measured transmittance and reflectance data as A=1-(T+R). Such an approach gives precise results for multilayers of smooth films.

### 6.3.3 Electromagnetic Simulation

Finite Elements Method based simulations were performed with the commercial software COMSOL Multiphysics. Simulation are full field, considering a monochromatic plane wave impinging at an angle of 40° as an excitation source.

### 6.3.4 Synthesis of $CsPbBr_3$ Nanocrystal

$CsPbBr_3$ nanocrystals were provided by the Nanochemistry group at IIT, and synthesized by following the procedure of Protesescu et al. with some minor modifications.[28] Lead(II) bromide (PbBr2, 99.999% trace metals basis), cesium carbonate ($Cs_2CO_3$, reagentPlus, 99%), octadecene (ODE, technical grade, 90%), oleylamine (OLAM, 90%), oleic acid (OA, 90%) Ethyl acetate ( 90%) and Toluene (TOL, anhydrous, 99.8%) were purchased from Sigma-Aldrich. 0.3 mmol of $PbBr_2$ and 10ml of octadecene (ODE) were loaded in a 25ml 3-neck flask and dried under vacuum for 30 min at 120 °C. Degassed OA (Oleic Acid, 0.8 ml) and OAm (Oleylamine, 0.8ml) were injected under nitrogen flow. After complete dissolution of the $PbBr_2$, the temperature was raised to 170 °C and 0.6 ml of previously synthesized Cs-oleate (0.125 M in ODE) was swiftly injected. Immediately after the injection, the NCs solution was quickly cooled down to room temperature with an ice water bath and the NCs were collected via high-speed centrifugation (at 12000 rpm for 10 minutes), followed by redispersion in 3ml of toluene. The purification process was repeated again by adding 1ml of ethyl acetate, and finally, the NCs were dispersed into 2ml toluene. The deposition of $CsPbBr_3$ NCs has been carried out by spin-coating at 2000 rpm for 60 seconds.

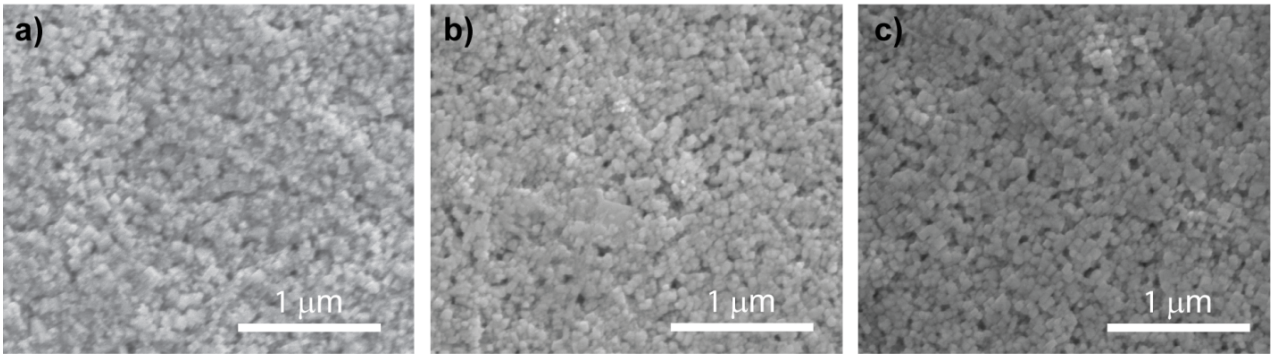


Figure 6.2. SEM analysis demonstrating the homogeneity of the NC films deposited on (a) bare alumina substrate, (b) MIM and, (c) MIMIM samples.

### 6.3.5 Fluorescence Spectroscopy

Photoluminescence (PL) on MIM and MIMIM structures coated with perovskites films on the top was measured with an Edinburgh Instruments fluorescence spectrometer (FLS920), which included a Xenon lamp with monochromator for steady-state PL excitation. The PL spectra recorded from MIM and MIMIM were obtained with an excitation wavelength of 400 nm by keeping excitation and emission slit width fixed at 2 nm and 1 nm, respectively. The spectra were recorded with 2 nm resolution and 0.5 second dwell time. Time resolved PL decay was studied with a time-correlated single-photon-counting unit coupled to a pulsed diode laser. The PL decay traces were recorded by exciting the sample at 405 nm with a 50 ps pulse at a repetition rate of 0.05 – 1 MHz. The signal was collected at PL peak wavelength with a bandwidth of 10 nm. The PLQY of the films has been measured with a calibrated integrating sphere and an Edinburgh FLS900 fluorescence spectrometer. All the measurements were carried out on spin-coated perovskite films on MIM and MIMIM substrate with dimensions of $1.6 \times 1.3$ cm$^2$ at an excitation wavelength of 400 nm. The optical density of the spin coated films was kept around 0.1 at the excitation wavelength. The signal was collected with an excitation and emission bandwidth of 10 and 0.40 nm, respectively.

## 6.4 Spectroscopic Ellipsometry

### 6.4.1 Comparison between Effective Medium Theory and Experimental Effective Dielectric Permittivity:

The optical properties of metal/dielectric stacks made of a sufficiently high number of bilayers are usually calculated in the framework of the Effective Medium Theory (EMT). Such an approximation is able to take into account the extreme anisotropic nature of the multilayers, giving at the same time a very good estimation of some of their principal features such as the topological transitions[121] . According to the EMT, a metal/dielectric periodic multilayer exhibits two dielectric

permittivities, one parallel to the layers surface ($\varepsilon_{\parallel}$) and one perpendicular to them ($\varepsilon_{\perp}$), whose well known expressions are:

$$\epsilon_{\parallel} = \frac{\epsilon_D t_D + \epsilon_M t_M}{t_D + t_M} \tag{6.1}$$

$$\epsilon_{\perp} = \frac{\epsilon_D \epsilon_M (t_D + t_M)}{\epsilon_D t_D + \epsilon_M t_M} \tag{6.2}$$

However, the resonant propagation regime occurring in stacks made of an exiguous number of metal/dielectric bilayers is completely neglected by the EMT. In order to demonstrate this discrepancy, we reported in Figure 6.3 a comparison between the real part of $\varepsilon_{\parallel}$ and $\varepsilon_{\perp}$ calculated with the equation 6.1 and 6.2, together with the experimentally measured effective permittivity by means of ellipsometry:

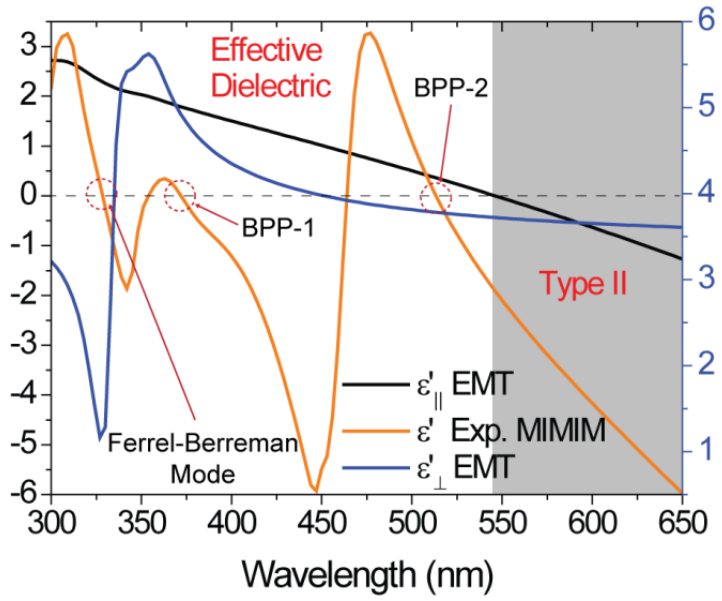


Figure 6.3: Comparison between the experimental, ellipsometrically measured effective dielectric permittivity and the EMT expressions of $\varepsilon_{\parallel}$ and $\varepsilon_{\perp}$ .

As we discussed above, a MIMIM subwavelength structure constitutes a double plasmonic cavity. As such, it is possible to confine two plasmonic modes, corresponding to the so-called BPPs inside the dielectric layers that are sandwiched between nanometric metal mirrors. Figure 6.3 demonstrates that the plasmonic modes correspond to an ENZ response for each cavity that match exactly the confined wavelengths. The orange curve in Figure 6.3 represents the experimental ellipsometrically measured dielectric permittivity of the MIMIM structure. The occurrence of the ENZ condition at both the two BPPs, as well as at the Ferrel-Berreman mode (around 327nm) is well evident as a zero crossing (see red dotted circles) of the dielectric permittivity curve. The effective permittivities (red and black curves) calculated by EMT completely neglect these features, and therefore are unable to describe the propagation in the two epsilon-near-zero regimes as well as in the Ferrel-Berreman mode.

### 6.4.2 Double Epsilon-Near-Zero Mode

In Chapter 5 we had detailed discussion of existence Epsilon near zero mode in both MIM and MIMIM systems. In order to exploit the novel phenomena like infinite photonic density of states (PDOS) at ENZ wavelength, MIM and MIMIM can be coupled to fluorophore in which the absorption and emission of the fluorophore are in resonance with the ENZ mode of MIM and MIMIM.

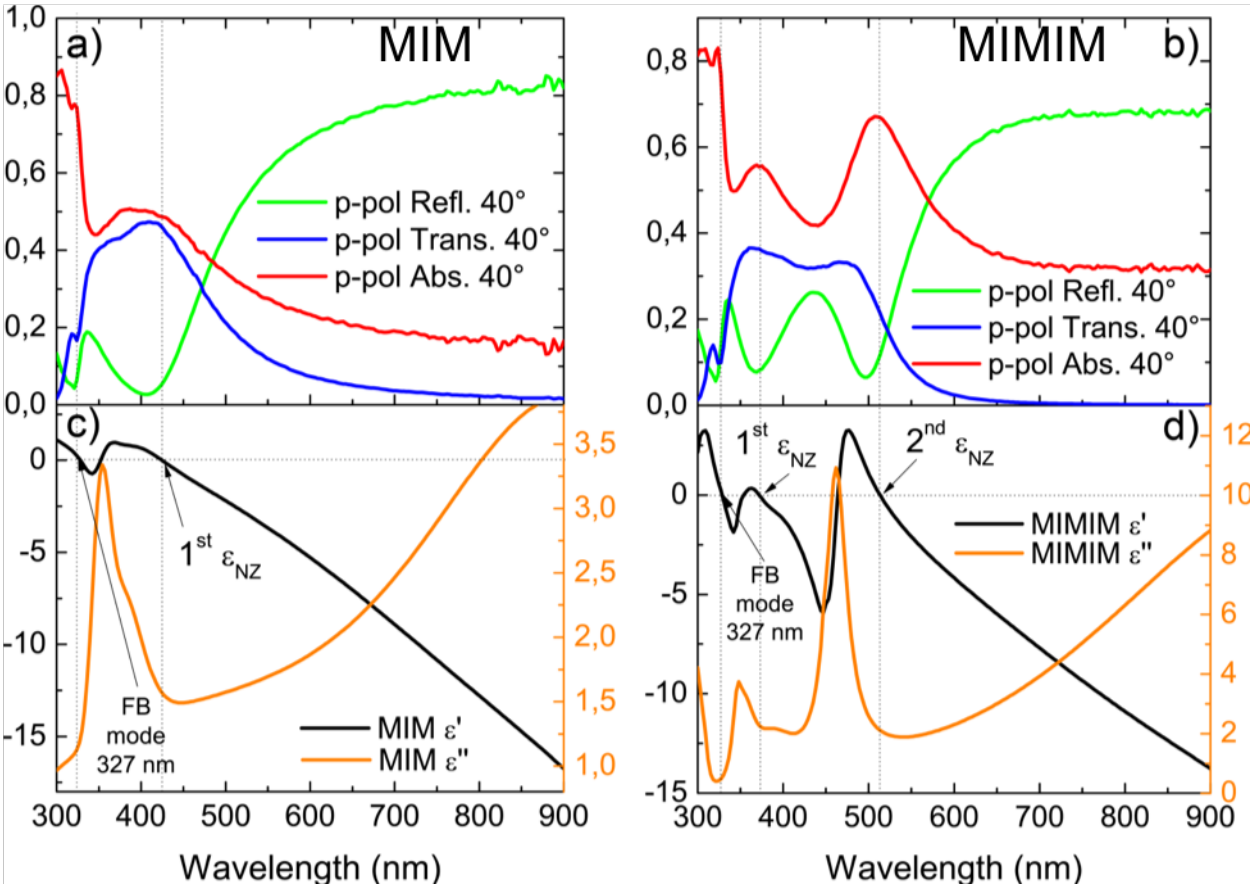


Figure 6.4. (a,b) Transmittance (blue), Reflectance (green) and Absorbance (red) of a) the MIM and b) the MIMIM systems. (c,d) Ellipsometrically measured real (black) and imaginary (orange) part of the dielectric permittivity of the MIM (c) and MIMIM (d) structures.

Figures 6.4a and 6.4b show the p-polarized reflectance (R) and transmittance (T) measured with an ellipsometer at a grazing angle of 40° for the MIM and MIMIM nanocavities. The absorbance (A) was then calculated as A=1-(T+R). As expected, for the MIM structure a maximum in absorbance is detected very close to the dip in reflection (see Figure 6.2.a), corresponding to the BPP mode of this structure at 425 nm. For the MIMIM system, as predicted, two BPPs modes are observed as maxima in absorbance, the first one at 373 nm and the second one at 510 nm. Both

the MIM and MIMIM structures manifest a peak in absorbance at λ=327 nm due to the well-known Ferrel-Berreman mode. The Ferrel Berreman mode constitutes a particular case of very low-loss BPP resonance, whose ENZ nature has been extensively investigated by theory[52,53]. Even though in the SPEA process we do not take its contribution into account, its presence is of crucial importance for validating our experimental investigations. As mentioned before, the optical constants of metal/dielectric multilayers are usually approximated in the framework of the EMT. For structures with only a small number of layers, this method does not yield zero crossings in the effective permittivity dispersions at the frequencies of the BPPs, and therefore completely neglects their occurrence. Therefore, a direct measurement of the dielectric permittivities of both the MIM and MIMIM system is required. For this purpose ellipsometry is a powerful tool, and Figures 7.5c-d show the ellipsometrically measured real and imaginary dielectric permittivities of the MIM and MIMIM multilayers, respectively. The ellipsometric investigation of the optical response of the MIM and MIMIM structures allows for a homogenization of their dielectric permittivities, i.e. the optical properties of the plasmonic multilayer structures can be fully described by a homogenized permittivity function. This approach illucidates the ENZ nature of the BPPs originating from the plasmonic multilayers, and is corroborated by reproducing the experimental transmission and reflection spectra with good accuracy. Ellipsometric measurements confirm the presence of the Ferrel-Berreman mode occurring in both the structures around 327 nm, highlighting its low loss ENZ nature. For the MIM structure, one other low-loss ENZ wavelength is detected at λ=425 nm, the $BPP_1$ for which a corresponding maximum in absorbance is found. For the MIMIM structure, two low-loss ENZ modes are detected apart from the Ferrel-Berreman mode, the $BPP_1$ and $BPP_2$, respectively at 373 nm and 510 nm, which correspond precisely to the two measured absorbance peaks.

### 6.4.3 Finite Element Simulation:

In order to confirm the plasmonic nature and the nanometric confinement of the electric field inside the dielectric layers sandwiched between the silver ones, Finite Elements Method based simulations have been performed by using COMSOL Multiphysics. Figures 7.5b-c show the electric field inside and around the MIMIM multilayer induced by illumination at an angle of 40° incidence for wavelengths at 384 nm and 510 nm (the ENZ wavelengths). Clearly the electric field is strongly enhanced in the dielectric layers of the MIMIM structure at the BPP frequencies, due to the ENZ condition. This affects also the wave fronts which are almost parallel to the layers in the plasmonic cavity. We note that the simulated absorbance peak is found at 373 nm and therefore slightly shifted with respect to the experimental one at 384 nm. Figure 6.5a shows a comparison between the experimentally derived absorbance and the COMSOL simulation (red curve), calculated by integrating the electric field inside the two dielectric layers. The very good agreement in spectral position between experiments and simulations confirms the ENZ nature of the two absorbance peaks.

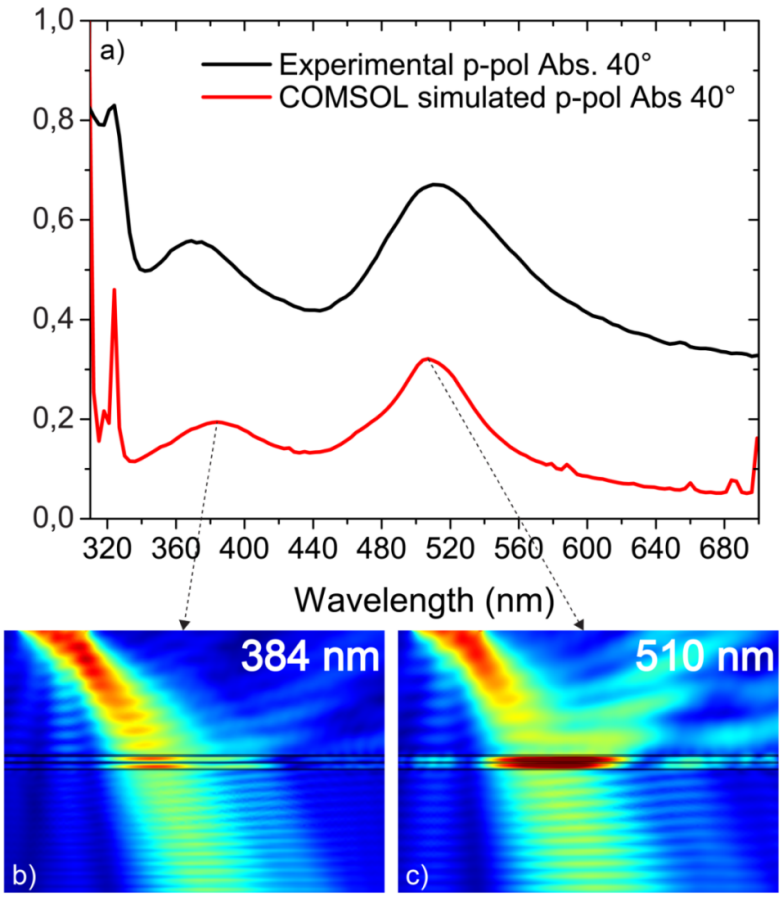


Figure 6.5. a) Experimentally measured absorbance (black) of the MIMIM structure and the corresponding COMSOL (red) simulation. Field propagation profile simulated at the two ENZ wavelengths found based on the COMSOL simulation, respectively at b) 384 nm and c) 510 nm. In both cases, the electric field remained strongly confined in the dielectric layers.

## 6.5 Purcell Effect Enhancement

### 6.5.1 SPEA and SPCE effect

Recently, it has been demonstrated that the weak coupling based interaction between a fluorophore and a plasmonic absorber in its proximity induces the SPEA phenomenon[137]. Moreover, the possibility of reaching an extremely high Photonic Density of States (PDOS) in the proximity of the ENZ wavelength has been extensively demonstrated[143, 165-166]. The hyperbolic (or indefinite) isofrequency surfaces occurring in the ENZ regimes allow wave vectors up to infinitely high values to propagate inside the metamaterial, which are usually known as "*high-k modes*"[151, 153, 160, 167]. This effect results in an extremely high PDOS at the ENZ frequency. Due to the high PDOS, a fluorophore in the proximity of an ENZ medium experiences a high Purcell effect and, as a consequence, its decay time is strongly reduced.[151, 153-154, 158] Eventually, such a high PDOS can lead to the enhancement of the spontaneous emission of a fluorophore, an effect known as SPCE.

The MIMIM plasmonic multilayer allows to take advantage of both the SPEA and SPCE effects at the same time, thanks to its double-ENZ resonating nature. In order to evaluate the SPEA and SPCE contributions to the PL and decay time, we compare the results of the MIMIM and MIM structures. Due to its single ENZ behavior the MIM system can solely exploit one resonance effect, which for $CsPbBr_3$ nanocubes as a dye is the SPEA. For $CsPbBr_3$ nanocubes, (i) their absorption band falls within both the single plasmon band of the MIM system and the first plasmon band of the MIMIM structure, while (ii) their emission matches the second ENZ wavelength of the MIMIM system. Figure 6.6a shows the absorption and emission of the $CsPbBr_3$ nanocubes together with the absorption bands of the MIM and MIMIM structures, confirming the above described overlap. The size and shape of the $CsPbBr_3$ nanocubes are evident in the Transmission Electron Microscopy (TEM) image displayed in Figure 6.6b.

### 6.5.2 Purcell Effect

The position of the fluorophore with respect to the plasmonic cavity plays a crucial role for the emission enhancement. One of the best ways to maximize their interaction is to embed the fluorophore inside the plasmonic cavity.[168-169] However, this requires technologically challenging processes in order to prevent the fluorophore's degradation, and to ensure a suitable spacing from the plasmonic metallic elements at the same time. A more facile approach consists in placing the fluorophore outside of the cavity, and in this case the distance to the cavity determines the emission properties. Here, we used an alumina layer as a spacer between the MIMIM cavity and the perovskite emitter layer, and we tuned its thickness from 5 nm to 100 nm. We find a maximum in PL for a layer thickness of 50 nm as shown in the inset in Figure 6.6c. Since the dielectric spacer layer is of the same material as the dielectric layers in the MIMIM structure (forming a MIMIMI multilayer), it strongly influences the electric field distribution. Finite elements simulations using

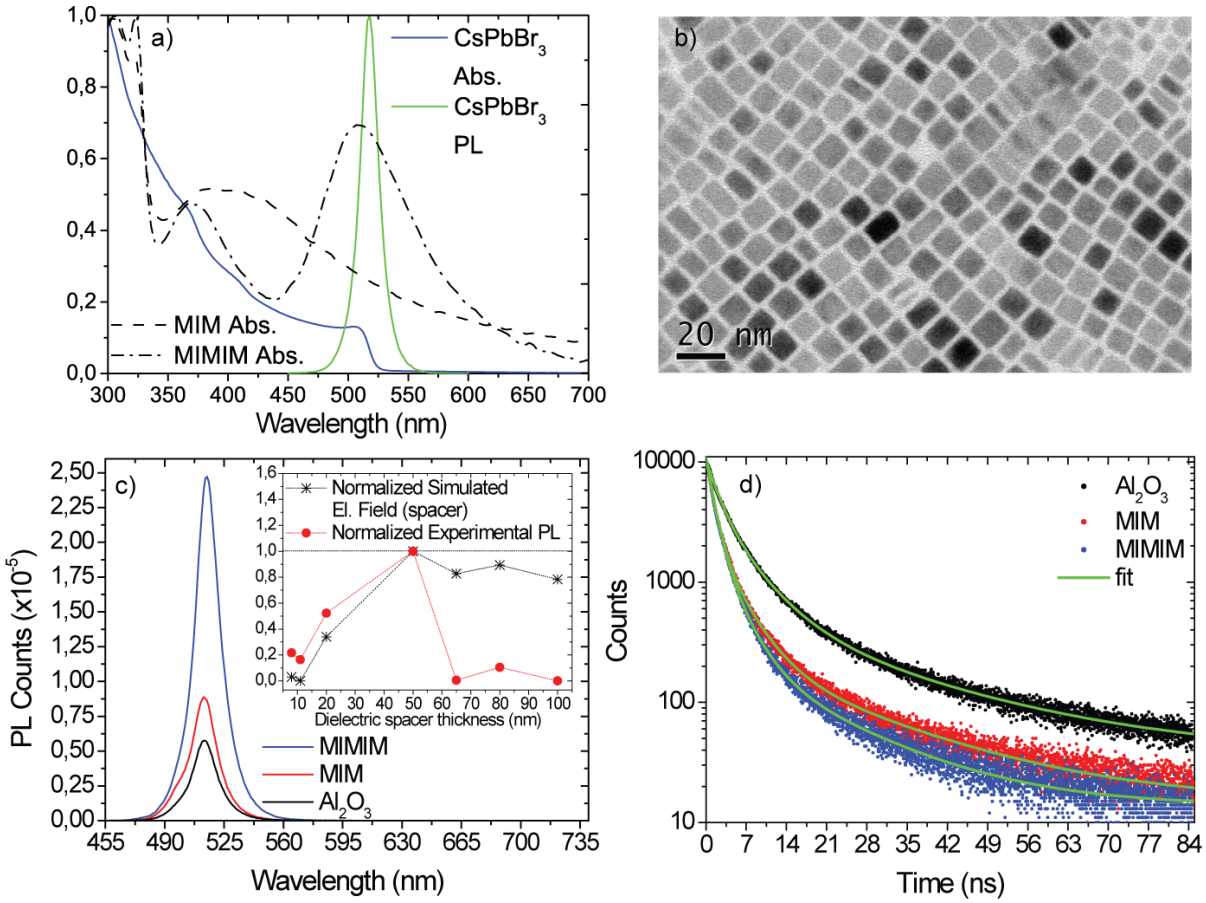


Figure 6.6. (a) Normalized absorption (blue line) and emission (green line) spectra of the $CsPbBr_3$ nanocubes are plotted together with the MIM (dashed black curve) and MIMIM (dash-dot black curve) normalized absorbance. (b) TEM images of the $CsPbBr_3$ nanocubes. (c) Spontaneous emission and (d) decay times of $CsPbBr_3$ nanocubes deposited on a bare $Al_2O_3$ substrate (black), a MIM (red) and MIMIM (blue) structure. The inset in (c) shows the experimental PL intensity versus the thickness of the dielectric layer at the surface, together with the results obtained for the electric field with finite elements simulations (COMSOL).

COMSOL show that the electric field is maximized for a spacer layer of 50 nm, in excellent agreement with our experimental data. A spacer layer with 50 nm thickness also strongly contributes to minimize the losses in PL induced by the metallic layers in the MIMIM structure. We emphasize that the spacing of the fluorophores to the metallic cavity can be well controlled without technological difficulty, and that our planar structure with the emitter layer on the surface ensures facile fluorophore deposition and accessibility for further needs.

The photoluminescence (PL) spectra of the $CsPbBr_3$ nanocubes are reported in Figure 6.6c for the three different cases: with the $CsPbBr_3$ nanocubes film on the top of: (i) a simple 80 nm $Al_2O_3$ layer, (ii) the MIM covered with a 50 nm thick $Al_2O_3$ spacer layer , and (iii) the MIMIM structure covered with a 50 nm thick $Al_2O_3$ spacer layer. A small increase of PL is found in the case of the MIM system that can be attributed to the SPEA effect. For the MIMIM multilayer, the PL experiences a noticeable four-fold enhancement, indicating that in this case both the SPEA and the

SPCE effects are taking place. The Time Correlated Single Photon Counting (TCSPC) measurements displayed in Figure 6.6d allow to access the spontaneous decay rate, and the fitting results for the life times with a three-exponential decay are reported in Table 6.1.

Table 6.1: Lifetime for the three systems consisting in simple $Al_2O_3$, MIM and MIMIM structures with a 50 nm thick $Al_2O_3$ layer on the top, obtained from fitting the decay traces with a three-exponential function. The average life time and the measured quantum yields (QYs) are also reported, as well as the calculated average radiative and non-radiative decay rates that were obtained using equations 1&2.

| | $\tau_1$ (ns) | $\tau_2$ (ns) | $\tau_3$ (ns) | $\tau_{AVG}$ (ns) | QY (%) | $\Gamma$ ($\mu s^{-1}$) | $K_{nr}$ ($\mu s^{-1}$) |
|---|---|---|---|---|---|---|---|
| $Al_2O_3$ | 2.14 | 5.74 | 23.26 | 9.77 | 50 | 51.16 | 51.16 |
| MIM | 1.27 | 4.23 | 20.5 | 6.32 | 35 | 55.33 | 102.76 |
| MIMIM | 1.34 | 3.58 | 15.67 | 4.59 | 75 | 163.09 | 54.36 |

In the proximity of the MIM structure, the lifetimes are shortened with respect to those of the bare $Al_2O_3$. It is worth mentioning that the MIM structure in this spectral range is extremely reflective, manifesting a strong metallic behavior. This is well known to occur in MIM structures above the ENZ wavelength since in that regime they start approaching the features of a so-called type II anisotropy typical of a hyperbolic metamaterial in the hyperbolic region. This increases the PDOS, which in turn, enhances the spontaneous decay rate. Comparing the MIM and MIMIM structures, we find that their fastest life time components $\tau_1$ are very similar (their difference of 50 ps is below the time resolution of our setup), while we observe significant reduced life time components $\tau_2$ and $\tau_3$ for the latter. We assign this reduction in life time to the increased PDOS provided by the SPCE effect, i.e. to the coupling of the spontaneous emission with the ENZ regime of the MIMIM system at 510 nm wavelength.

We have measured the quantum yield (QY) obtained from the perovskite film on the $Al_2O_3$, MIM, and MIMIM substrates, taking the absorbance of each non-coated substrate into account. We obtained a QY of 50% from the perovskite film on the $Al_2O_3$, 35% QY on the MIM, and a high QY of at least 75% on the MIMIM, as reported in Table 1. The decrease in QY from the $Al_2O_3$ to the MIM reflects the weak SPEA effect and the losses induced by the metallic layers, whereas the strong increase to 75% or higher for the MIMIM can be attributed to the plasmonic enhancement by the SPCE process. With the QY values and the values $\tau_{AVG}$ for average lifetime we can calculate the average radiative and non-radiative decay rates, using equation 2.26 and 2.27 (in chapter 2) We obtain a strongly enhanced radiative decay rate for the MIMIM structure, and enhanced non-radiative decay in the MIM system that reflects the losses due to the vicinity of the metallic layers.

Since the PL and QY are strongly enhanced in the MIMIM structure, we can conclude that double ENZ condition leads to an enhanced PDOS that acts on the radiative decay of the nanocrystals, manifesting the Purcell effect.

## 6.6 Chapter Summary

We demonstrated the possibility to exploit the dual resonant nature of a specifically designed double-ENZ MIMIM multilayer in order to enhance both the absorbance, and the photoluminescence together with the decay rate of a film of $CsPbBr_3$ perovskite nanocrystals deposited on the top of the layer structure. Thanks to the special plasmonic features of the MIMIM system, two ENZ wavelengths at 373 nm and 510 nm that represent the BPP modes of this structure could be theoretically designed and directly experimentally measured by means of spectroscopic ellipsometry. In the MIMIM system, the PDOS is greatly enhanced in the absorption and emission bands of the dye and therefore both the SPEA and SPCE phenomena take place. This leads to a noticeable enhancement of the spontaneously emitted photons and of their decay rates from a fluorophore layer at the surface, in comparison with the MIM system, where only the SPEA effect is present. We demonstrate the possibility to enhance the Purcell effect without metallic grating couplers and sophisticated lithography processes. The double-ENZ MIMIM multilayer shows wide design flexibility, since the two ENZ wavelengths can be tuned in the whole visible range, making this system compatible with all large variety dyes. The system we investigated here represents a versatile platform for engineering the PL and decay rate enhancement of a desired fluorophore, and allows for facile design and fabrication of the plasmonic cavity as well as for the deposition of the fluorophores. Furthermore, the ease of fabrication is suitable for large surfaces and compatible with requirements for biomedical sensing and low threshold lasers.

(Note: Results presented in this chapter are already published (V. Caligiuri et al., *ACS Photonics*, **2018**, *5* (6), pp 2287–2294, My personal contribution to this work includes sample fabrication and characterization, fluorescence spectroscopy measurements, ellipsometry analysis)

# Chapter 7:

## Robust and Bright Photoluminescence from Colloidal Nanocrystal/$Al_2O_3$ Composite Films Fabricated by Atomic Layer Deposition

**7.1 Abstract:** Colloidal nanocrystals are a promising fluorescent class of materials, whose spontaneous emission features can be tuned over a broad spectral range via their composition, geometry and size. However, towards embedding nanocrystals films in elaborated device geometries, one significant drawback is the sensitivity of their emission properties on further fabrication processes like lithography, metal or oxide deposition etc.. In this chapter, we demonstrate how bright emitting and robust thin films can be obtained by combining nanocrystal deposition from solutions via spin-coating with subsequent atomic layer deposition of alumina. For the resulting composite films, the layer thickness can be controlled on the nanoscale, and their refractive index can be finely tuned by the amount of deposited alumina. Ellipsometry is used to measure the real and imaginary part of the dielectric permittivity, which gives direct access to the wavelength dependent refractive index absorbance of the film. Detailed analysis of the photophysics of thin films of core-shell nanocrystal with different shape and different shell thickness allow to correlate the behavior of the photoluminescence and of the decay life time to the changes in the non-radiative rate that are induced by the alumina deposition. We show that the photoemission properties of such composite films are stable in wavelength and intensity over several months, and that the photoluminescence completely recovers from heating processes up to 240 °C. The latter is particularly interesting, since it demonstrates robustness to the typical heat treatment that is needed in several process steps like resist-based lithography and deposition by thermal or electron beam evaporation of metals or oxides.

### 7.2 Introduction:

Colloidal nanocrystals have recently drawn significant interest for applications in light emitting devices due to their size and shape dependent optical and electronics properties, like narrow emission band and ultra-high photoluminescence quantum yield (PLQY).[78-81] In particular, core-shell structures are an efficient structure to reduce the influence of surface defects and allow for more bright and stable emission.[170-175] However, the stability of nanocrystals in thin films is significantly reduced, and their degradation caused by device fabrication processing and over time still hinders their use in effective optoelectronic devices.[176-177] In order to overcome this limitation, several methods have been studied, among which embedding the colloidal nanocrystals in a polymer matrix[178-180] or coating them with dielectric oxides [64, 181-186] revealed promising. Concerning coating of nanocrystal films with dielectric oxides, Atomic Layer Deposition (ALD)

has the advantage that the voids present in the thin films constitute suitable sites for the gaseous precursors acting in ALD.[64] Therefore ALD can efficiently infill these voids, which results in a compact composite film in which the nanocrystals are embedded in a dielectric matrix. [182-183, 186] We deposit alumina via ALD on nanocrystal films consisting of CdSe/ZnS core-shell nanoparticles, called dot-in-dots (DiDs) in the following, and CdSe/CdS dot-in-rods (DiRs). We chose those two materials, because on one hand they are among the most prominent colloidal nanomaterials used for light emission,[187-193] and because their difference in shape and architecture leads to different optical properties.[194-195] For example, DiRs can manifest polarized emission, and their elongated shape results in more porous films obtained by spin-coating. Although the PL intensity of the nanocrystal films is reduced by alumina deposition with just a few ALD cycles, we find that it recovers significantly once the infilling of the film is completed, which typically happens at 20-50 ALD cycles. Furthermore, the refractive index of the composite layer can be tuned to higher values with increasing amount of deposited alumina, until it saturates when the film is fully filled and the overcoating of the nanocrystal layer takes place. Concerning the study of the optical properties of such films, ellipsometry is extremely useful, both for evaluating the refractive index (*via* the real part of the dielectric permittivity) and for measuring the absorbance of the thin nanocrystal films via the imaginary part of the permittivity. The latter is usually problematic to measure in detail in transmission experiments, due to considerable background that originates from light scattering. Finally, composites films, where the nanocrystal layer has been fully overcoated by alumina, are robust to temperature treatment up to 240 °C, and maintain their PL intensity over several months of storage.

## 7.3 Materials and Methods:

**7.3.1 Nanocrystal Materials:** CdSe/ZnS DiDs stabilized with octadecylamine ligands were purchased from Sigma Aldrich (product number 790192) and dispersed in toluene with a concentration of 5mg/mL.

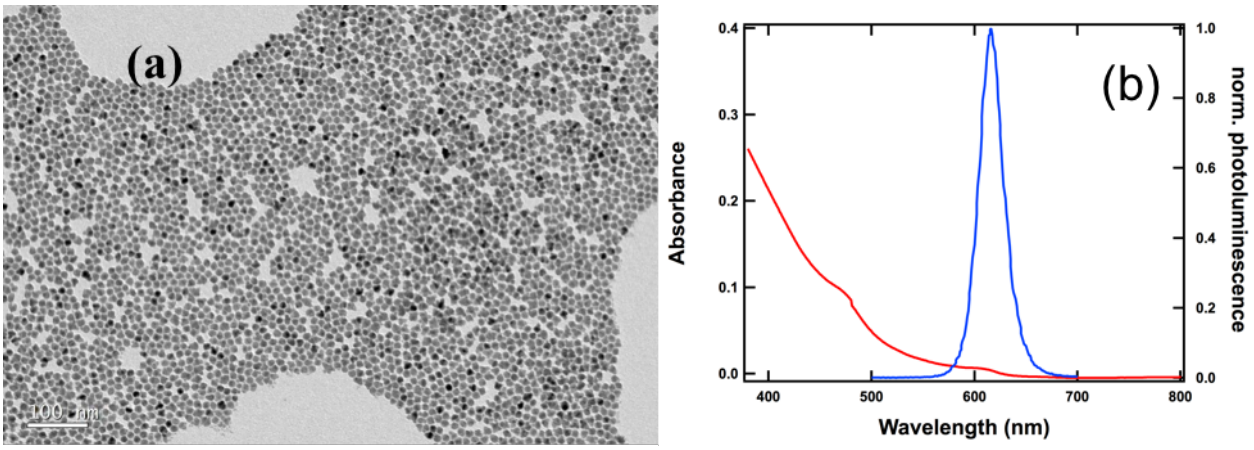


Figure 7.1. (a) Transmission electron micrograph of CdSe/ZnS Dots-in-Dots NCs (b) Photoluminescence and optical absorption spectra of CdSe/ZnS Dots-in-Dots in solution.

The CdSe/CdS DiRs were obtained from Dr. Prachi Rastogi from our group. For the thin-shell CdSe/CdS DiRs, first the CdSe cores with diameter of 4.3 nm were synthesized and purified according to the procedure described by Carbone et al..[174] For the shell growth, 90 mg of cadmium oxide was mixed together with 480 mg of ODPA, 3 mg TOPO and 60 mg HPA in a flask, and degassed at 130 $^0$C for an hour. Then 100 µM of the CdSe cores dispersed in S:TOP(90 mg:1.5 gm) were swiftly injected at 365 $^0$C into the flask under nitrogen atmosphere. After 8 minutes, the growth was terminated by cooling down the reaction. The samples were purified by precipitation with methanol, followed by centrifugation and resuspension in toluene.

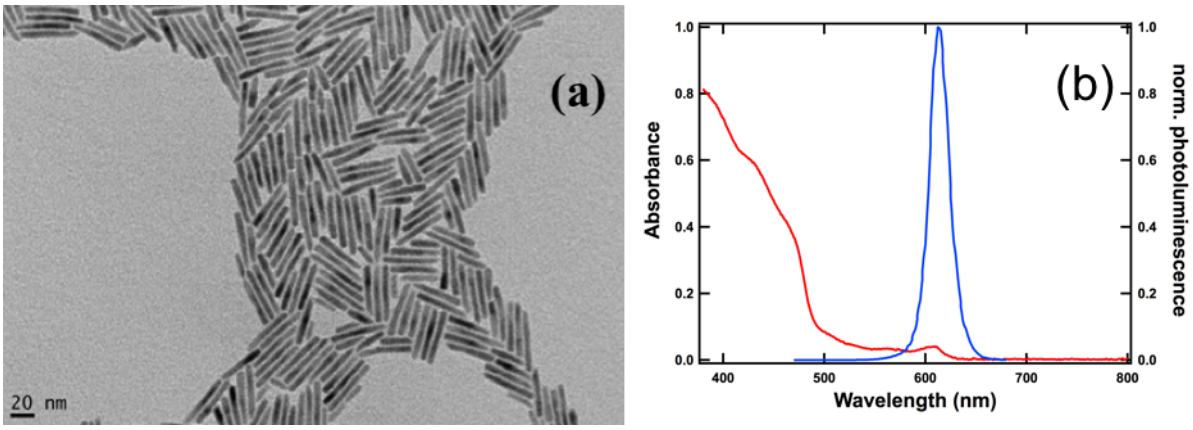


Figure 7.2. (a) Transmission electron micrograph of CdSe/CdS Dots-in-Rods NCs (b) Photoluminescence and optical absorption spectra of CdSe/CdS Dots-in-Rods in solution.

The thick-shell DiRs were synthesized from CdSe cores with 4.2 nm diameter according to the procedure described in Rastogi et al..[39] These DiRs had a diameter of 9 nm and a length of 17 nm.

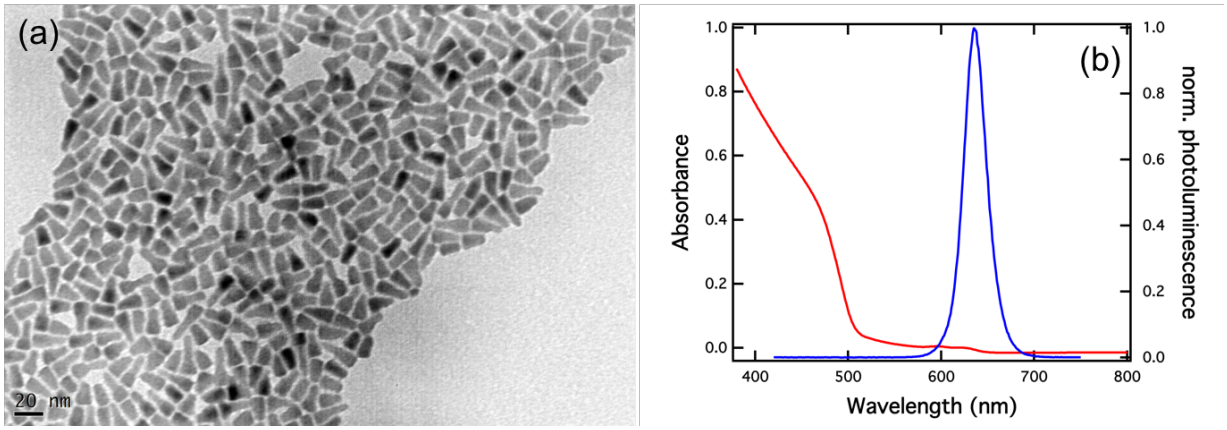


Figure 7.3. (a) Transmission electron micrograph of thick-shell CdSe/CdS Dots-in-Rods NCs (b) Photoluminscence and optical absorption spectra of thick-shell CdSe/CdS Dots-in-Rods in solution.

**7.3.2 Film Preparation:** The DIR and DID films were spin-coated on glass substrates at 3000 rpm for 1 minute, which resulted in a thickness of 33±3 nm and 25±2 nm for DIR and DID film respectively. The film thickness was measured with a Dektak profilometer. Figure 3.1(b,c) in

chapter 3 shows electron micrograph of spincoated DID and DIR film. SEM micrograph of ALD coated (100 cycles) DIR film and its cross-sectional image are shown in figure 3.6.

**7.3.3 ALD of Alumina:** Atomic layer deposition was carried out in a Flexal ALD system from Oxford Instruments, using a thermal process with a stage temperature of 110 °C, resulting in an alumina deposition rate of 0.09 nm/cycle. Tri-methylaluminate (TMA) and $H_2O$ were used as precursors, and we performed a pre-heating step for 300 s before stating the ALD cycles. Each cycle consisted of a $H_2O$/purge/TMA/purge with a pulse durations of 0.075/6/0.033/2 seconds, respectively.

## 7.4 Ellipsometry on ALD Coated NCs Film

### 7.4.1 Experimental Method

Spectroscopic Ellipsometry has been performed by with a V-VASE ellipsometer by Woollam in the range from 300 nm to 900 nm. Spectroscopic analysis, reflectance and transmittance spectra have been acquired at three different angles (50, 60, and 70°). Additionally, in order to refine the fit, normal incidence transmittance has been collected as well and fitted in the model. All measurements have been conducted with a resolution of 3 nm, and have been normalized to the intensity of the Xe lamp.

### 7.4.2 Tuning Refractive Index of ALD Coated NCs

The infilling and overcoating of the nanocrystal layer with alumina can be expected to modify the dielectric properties of the composite film, therefore, we have analyzed the dielectric permittivity by ellipsometry. Figure 7.4a and Figure 7.4c show the real part of the dielectric permittivity of the composite nanocrystal/alumina films as a function of the number of ALD cycles, measured at their respective emission wavelength. As expected from filling the voids in the film with a high refractive index material such as alumina, $\varepsilon'$, taken at the maximum of the PL peak, initially strongly increases with the number of ALD cycles (in the infilling regime), and eventually saturates in the overcoating regime. The DiD film manifests a sharp increase in dielectric constant within the first 20 ALD cycles, with a total increase from 3.41 to 3.62. For the DiR sample we observe an equally strong increase of 0.2 in $\varepsilon'$ (from 3.52 to 3.72) in the infilling regime that occurs more gradually, which that can be related to the slower filling of the larger amount of voids present in the DiR nanocrystal film. In this respect, the data obtained by ellipsometry allows us to distinguish the infilling from the overcoating regime more precisely.

### 7.4.3 Infilling and Overcoating Regime

Another way to differentiate between infilling and overcoating regime was to measure the film thickness after each interval of ALD cycles and compare it to the ellipsometry data. For a small number of cycles, we can expect that the alumina fills the voids in the nanocrystal film, as

illustrated in Figure 7.5a, and refer to this process as “infilling” in the following. Once the voids have been completely filled, the ALD of alumina increases the thickness of the layer, which can be related to overcoating of the composite layer with alumina (see Figure 7.5b). Once the voids have been completely filled, the ALD of alumina increases the thickness of the layer, which can be related to overcoating of the composite layer with alumina (see Figure 7.5c).

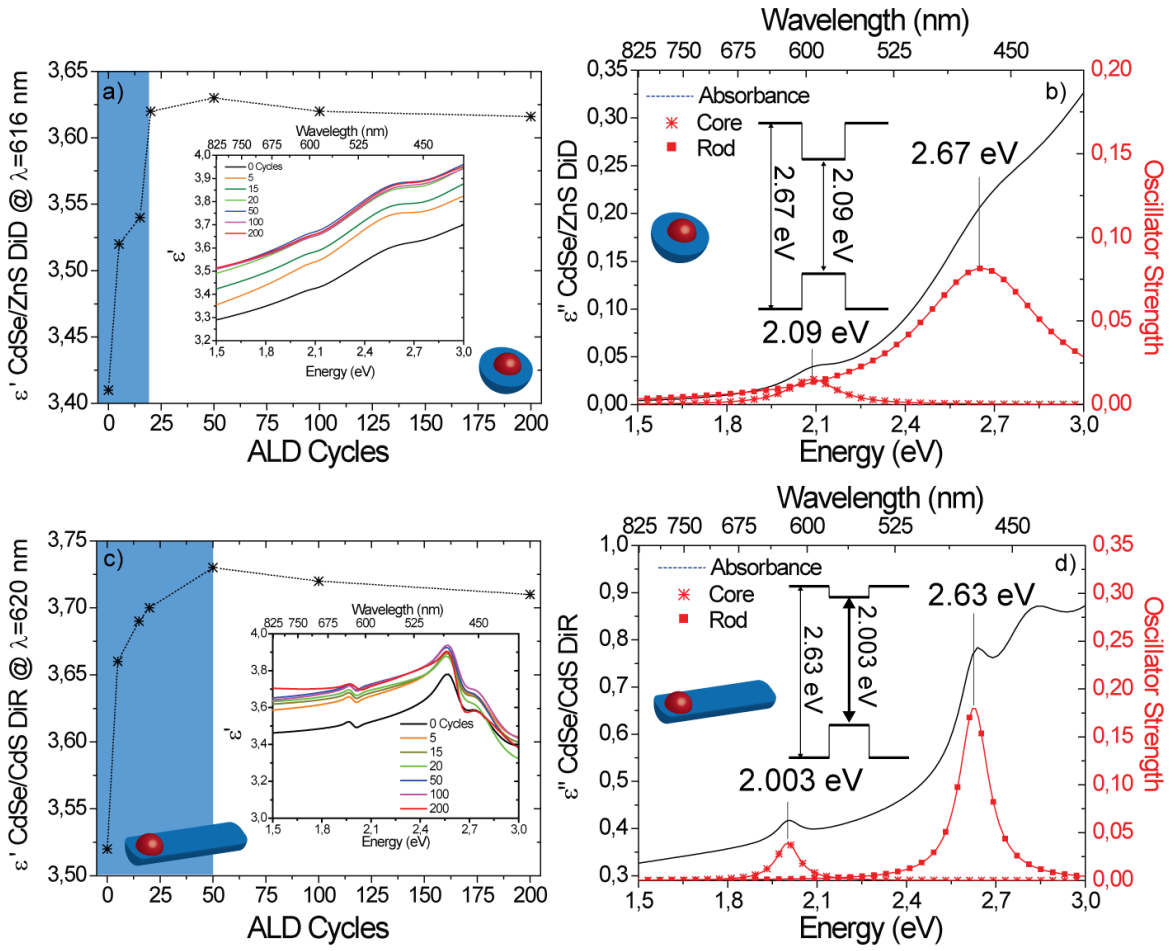


Figure 7.4 (a) and (c) depict the real part of the dielectric permittivity (ε’) acquired at the emission peak wavelength of DiD (a) and DiR (c), as a function of the number of ALD cycles. The shaded area highlights the infilling regime in which the permittivity increases. (b) and (d) show spectroscopic ellipsometry analysis of the imaginary part of the dielectric permittivity (ε’’) of the CdSe/ZnS DiD (b) and CdSe/CdS DiR (d) films. The contribution originating from the absorbance of the cores and the shells of the two systems have been fitted by means of lorentzian oscillators

following. Once the voids have been completely filled, the ALD of alumina increases the thickness of the layer, which can be related to overcoating of the composite layer with alumina (see Figure 7.5c). We measured the thickness of the films before and after the alumina deposition with a profilometer, as shown in Figure 7.5c. We find that up to around 20 cycles the film thickness remains more or less constant, followed by a linear increase. This allows us to distinguish the

infilling (flat) from the overcoating (linear increase) range, as illustrated by the shaded area in Figure 7.5c.

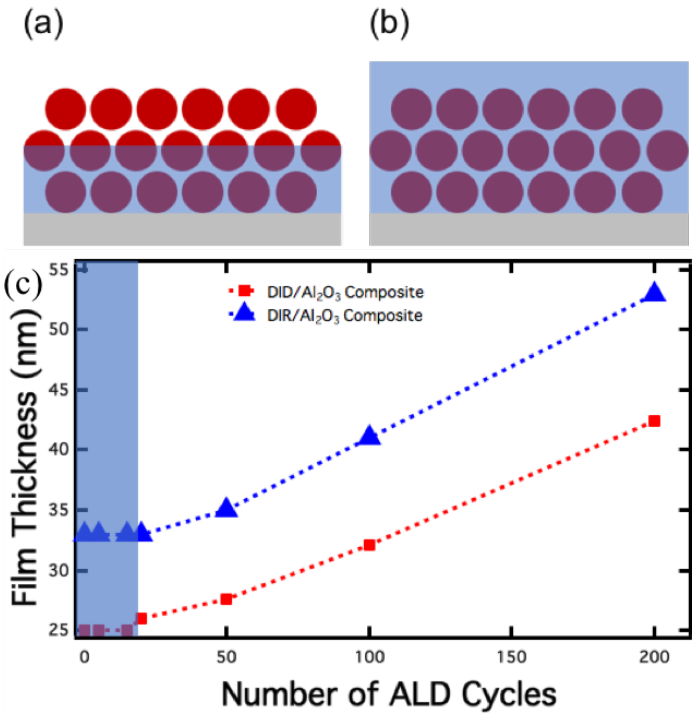


Figure 7.5 (a,b) Simplified schemes of a partially infilled (a) and an overcoated (b) nanocrystal film on a planar substrate. (c) Film thickness versus number of ALD cycles for DiD (red) and DiR (blue) films. The shaded region indicates the "infilling" regime, in which the alumina is deposited within the nanocrystals in the film, i.e. without significantly increasing the thickness of the layer.

### 7.4.4 Effective Tool for Determining Band gap for Thin Film

The absorption spectrum of a thin nanocrystal film is often problematic to measure in optical transmission experiments, for example with a spectrophotometer, since the morphology of the film results in considerable scattering. This light scattering typically leads to a pronounced tail in the absorption spectrum that camouflages details in this spectral range, which can make the assignment of the precise onset in absorption difficult. Another option that works extremely well for thin nanocrystal films is to access their absorbance by measuring the imaginary part of complex dielectric permittivity by ellipsometry. Figure 7.6 shows a comparison of the measured absorption and dielectric permittivity spectra of a composite nanocrystal film. The imaginary part of complex dielectric permittivity provides a direct measure of the absorbance, and allows for a very accurate

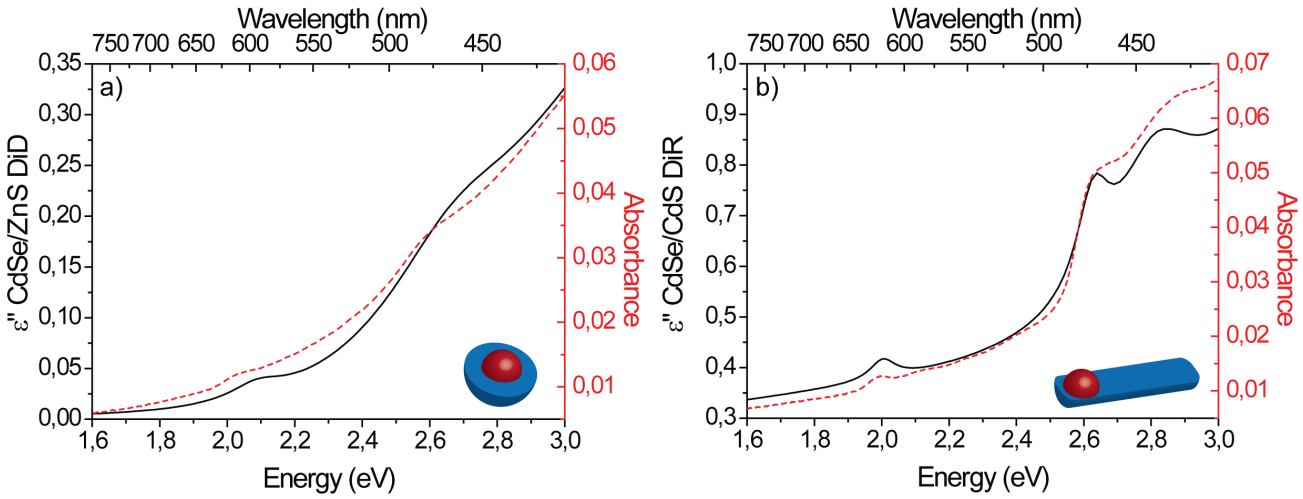


Figure 7.6. Comparison of the absorption spectra obtained via a spectrophotometer (Cary 5000) with the imaginary part of the dielectric permittivity measured with ellipsometry for DiD (a) and DiR (b) films on glass. Clearly, the features related to the optical transitions are more pronounced in the spectra obtained by ellipsometry.

assignment of the absorbance onset (*i.e.* the optical band gap), and higher energy transitions, as can be seen in Figures 7.4b and 7.4d. In particular, the contributions to the total absorbance deriving from the CdSe cores and CdS shells of the nanocrystals are evident in the spectra. These contributions can be quantitatively evaluated by modelling with damped harmonic oscillators[111, 196-197], which allows fitting of the resonances with the following complex term that contributes to the permittivity as given by equation 4.6 in chapter 4. In terms of the Lorentzian oscillator model, α is the oscillator strength, and β represents the damping of the oscillator. We note that eq. (8.1) is intrinsically Kramers-KrÖnig consistent, and that the real imaginary part of the function is equivalent to the description of light absorption in eq. (3) in Jellison et al.[196] The parameters related to the optical transitions in the CdSe/ZnS DiD and CdSe/CdS DiR nanocrystal films assigned to the core-shell band structure are reported in Table 7.1.

Table 7.1. Energy, oscillator strength and broadening of the core and shell transitions of the DiD and DiR nanocrystal films obtained by ellipsometry.

| | $E_0$ (eV) | A | B |
|---|---|---|---|
| DiD Core | 2.09 | 0.015 | 0.199 |
| DiD Shell | 2.67 | 0.081 | 0.507 |
| DiR Core | 2.003 | 0.039 | 0.093 |
| DiR Shell | 2.63 | 0.181 | 0.118 |

## 7.5 Fluorescence Spectroscopy on ALD Coated NCs Film

*Experimental Method:* PL on nanocrystals in solution and in films were carried out with an Edinburgh Instruments fluorescence spectrometer (FLS920), which included a Xenon lamp with monochromator for steady-state PL excitation. The PL spectra recorded from films were obtained

with an excitation wavelength of 400 nm by keeping excitation and emission slit width fixed at 2 nm and 1 nm, respectively. The spectra were recorded with 2 nm resolution and 0.5 second dwell time. Time resolved PL decay was studied with a time-correlated single-photon-counting unit coupled to a pulsed diode laser. The PL decay traces were recorded by exciting the sample at 405 nm with a 50 ps pulse at a repetition rate of 0.05 – 1 MHz. The signal was collected at PL peak wavelength with a bandwidth of 10 nm. The PLQY of the films has been measured with a calibrated integrating sphere and an Edinburgh FLS900 fluorescence spectrometer. All the measurements were carried out on spin-coated NCs film on glass substrate with dimensions of $1.6\times1.3$ $cm^2$ at an excitation wavelength of 400 nm. The optical density of the films was kept around 0.1 at the excitation wavelength. The signal was collected with an excitation and emission bandwidth of 10 and 0.40 nm, respectively.

Figure 7.7 shows the emission properties of the different films for CdSe/ZnS DiDs, and CdSe/CdS DiRs with respect to the number of ALD cycles. In all cases, we observe a rapid decrease in PL intensity within the first few cycles of ALD, followed by a recovery, and eventually again a much slower decrease. The maximum in recovery correlates very well with the transition from the infilling to the overcoating regime. For the DiRs, the photoluminescence quantum yield (PLQY) shows a similar behaviour as the PL amplitude, and in the case of the thick-shell DiRs, it reaches even higher values at 100 ALD cycles as compared to the PLQY of the initial DiR layer. Concerning the DiDs, the PLQY is overall lower and remains more or less constant, within the error margins. The average life time of the emission was evaluated by fitting the decay traces obtained in TCSPC measurements at the peak maximum with a three-exponential function. For the DiDs and thin-shell DiRs it decreases for few ALD cycles, recovers around 100 ALD cycles and for 200 ALD cycles the average life time is consistently larger than that of the bare nanocrystal layer. For the thick-shell DiR films no decrease, but just an increase of the average life time is observed, and the values of the average life times are much larger than those of the thinner shell nanocrystals. The overall much larger life time of the thick-shell DiRs is in good agreement with those reported in ref.[198]. Next, we calculate the average radiative and non-radiative decay rates using equation 2.26 and 2.27 (chapter 2).

The average radiative and non-radiative rates are plotted in the lowest panels of Figure 7.7. We find that the ALD coating mainly affects the non-radiative rate for the DiDs and thin-shell DiRs, while the radiative rate remains more or less constant. For the thick-shell DiRs the radiative and non-radiative rates are only marginally affected by the alumina coating.

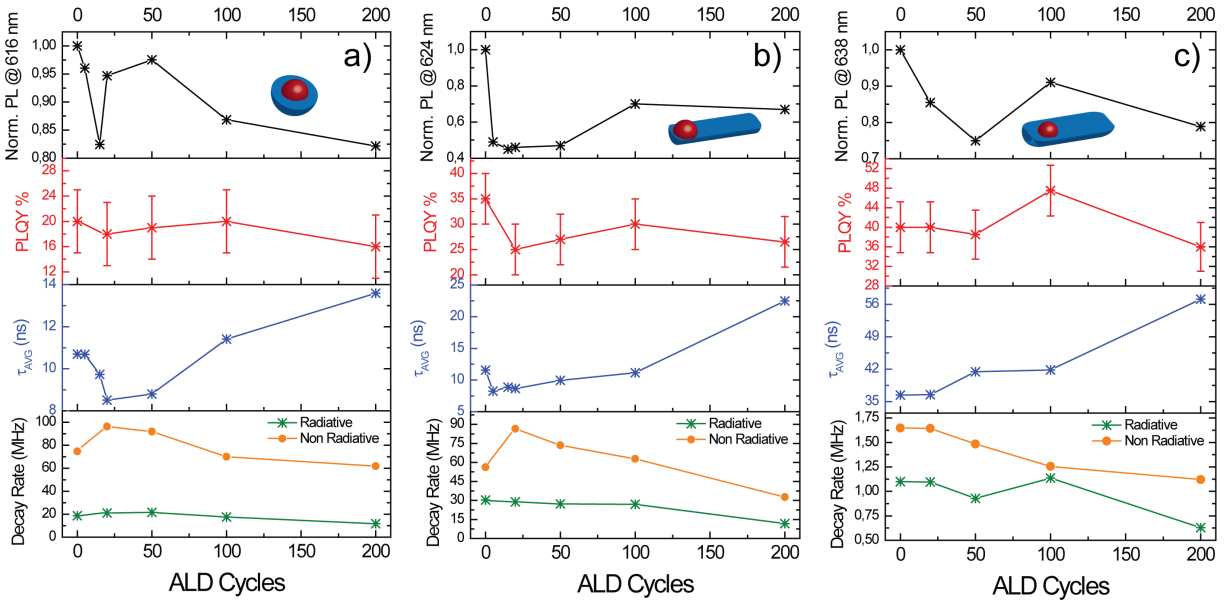


Figure 7.7. Photo-physical properties of DiD (a), thin-shell DiR (b), and thick-shell DiR (c) films coated with alumina via different number ALD cycles. The PL amplitude at the peak maximum, the PLQY, average life time, and the radiative and non-radiative decay rates are reported.

From this set of data, we can draw the following conclusions. For few cycles of ALD alumina coating the surface passivation of the nanocrystals, initially provided by the organic surface ligands, is deteriorated by the deposition of alumina that occurred at a temperature of 110 °C. Therefore, the non-radiative rate increases for the nanocrystals with a thin shell (DiDs and DiRs in (b)), which results in a decrease PL, PLQY, and average life time. Once the nanocrystal layer is completely filled and slightly overcoated with alumina (at 100 ALD cycles), the nanocrystal surface is again well protected from environmental influences that could quench the emission, and therefore the PL signal has recovered. The magnitude of the recovery depends on the quality of the surface passivation in the composite film, and on the sensitivity of the nanocrystal emission to surface effects. The DiDs that manifest more tightly confined excitons to the CdSe core region (by a thicker and higher bandgap shell) as compared to the thin-shell DiRs show an almost complete recovery of their PL (up to 96%), while the thin-shell DiRs recover only 70 % of their original PL. Also, the recovery of the PL in the DiD films occurs at lower number of ALD cycles (50 for DiDs, while 100 for DiRs), which directly relates to the faster infilling due to the much smaller void volume. The increase in PLQY and the much smaller impact of the alumina coating on the non-radiative rate in the case of thick-shell DiRs can be related to their increased insensitivity to surface modifications[188] and their long average PL decay times [198].

## 7.6 ALD on Monolayer Films Fabricated by Langmuir Blodgett Method

### 7.6.1 Monolayer Film Preparation:

Langmuir Blodgett troughs made from teflon with a volume capacity of 15 mL were filled with 8 mL of diethylene glycol. 20 µL of DiD NCs solution in hexane (1 mg/mL) were drop-cast on the top of diethylene glycol and the wells were covered for 10 minutes to ensure slow evaporation of hexane. Then the cover was removed, and the residual hexane was left to evaporate. After this, a yellow-colored floating film was formed over diethylene glycol. The film was fished from the solution with a glass substrate of size 5×5 $mm^2$, and dried on a hot plate at 80 °C to remove any remaining glycol.

### 7.6.2 Photoluminescence:

We coated a monolayer of DiDs that was fabricated by Langmuir Blodgett deposition with alumina by ALD in order to evaluate the influence of the NC film thickness on the emission properties. The results are depicted in Figure 7.8 and overall show a similar behaviour as the NC films described above, although the recovery in PL intensity reaches only up to 80 % and occurs slightly earlier (at 40 cycles).

## 7.7 Stability

### 7.7.1 Thermal Stability:

*Heat treatment:* The substrates were placed on a hot plate under ambient conditions and the PL was collected, under excitation at 350 nm with diode laser, with a lens and optical fiber coupled to an Ocean Optics (HR4000) spectrometer.

The overcoating of the nanocrystal films with alumina should lead to an improved stability of the optical properties towards harsh environmental conditions. Figure 7.9 and 7.10 shows the PL intensity recorded versus temperature in a heating and cooling cycle from 300 K to 520 K, normalized to its initial value at room temperature (300 K). In all cases the PL intensity strongly decreases with increasing temperature, following an Arrhenius behavior. However, for the non-coated films we observe also a significant reduction of the PL at RT after a completed temperature cycle that can be related to heat-induced degradation of the nanocrystals in the film, or of their surface

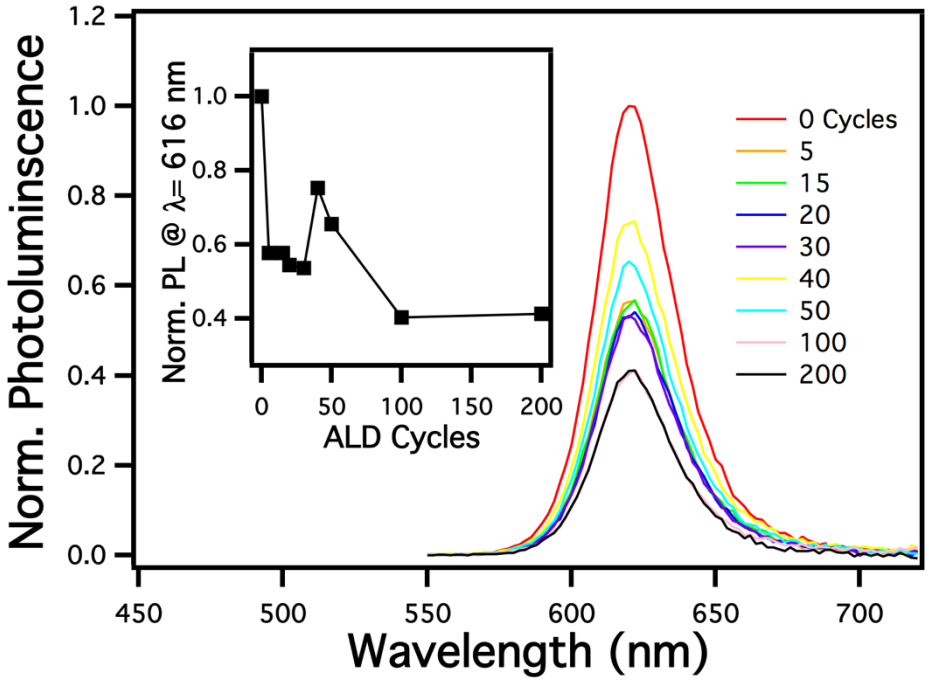


Figure 7.8. PL spectra recorded for different number of ALD alumina coating cycles for a monolayer of DiDs fabricated by Langmuir Blodgett deposition.

passivation. On the contrary, the alumina overcoated nanocrystal films are robust to this temperature treatment and maintain over 80 % of the PL for the DiDs, and 100% for the DiR after the cycle at RT (Fig. 7.9 and 7.10). We tentatively attribute the slight decrease in PL observed for the alumina coated DiD films to temperature induced changes at their surface, since the octadecylamine ligands used for these commercially available CdSe/ZnS might suffer from degradation at this temperature.

The robustness of the alumina overcoated DiR film to the heating up to 520K allows for fitting of the data with the Arrhenius formula:[199-202, 203]

$$I(T) = \frac{1}{1+C\ exp\left(-\frac{E_A}{k_B T}\right)} \qquad (6.4)$$

Where *I(T)* is the normalized PL intensity, *C* is a constant taking the non-radiative recombination into account, $E_A$ is the activation energy related to the non-radiative recombination process, and $k_B$ is the Boltzmann constant.

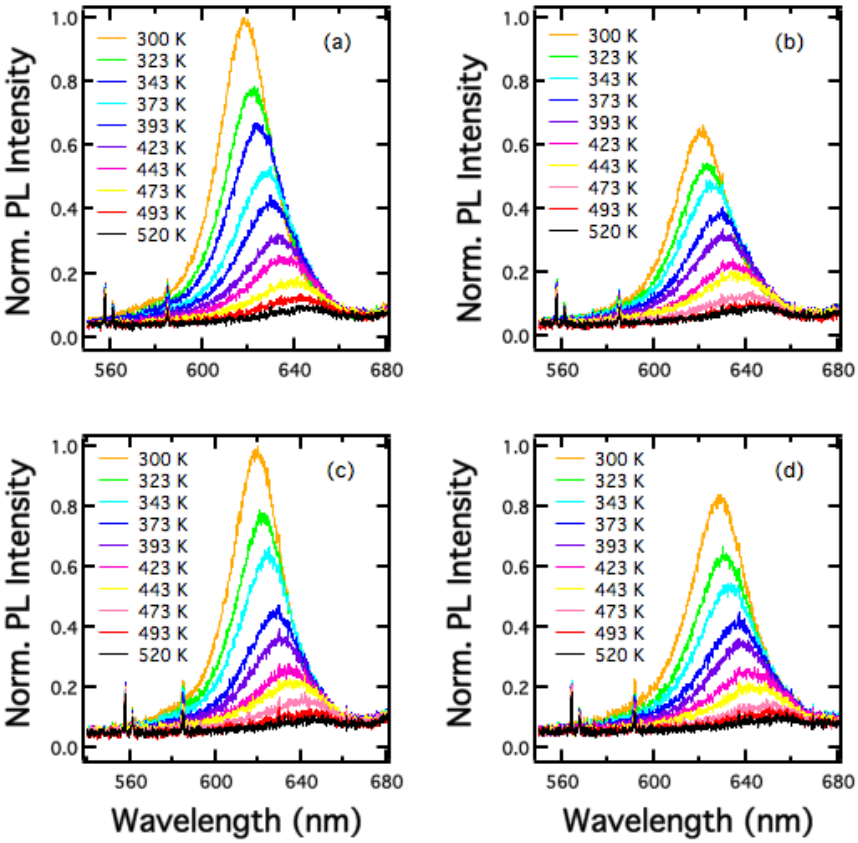


Figure 7.9. PL spectra recorded from non-coated DiD films (a-b), and from DiD films that were coated with 200 ALD cycles of alumina (c-d).

The fitting in Figure 7.12(d) yields an activation energy of around 0.3 eV, which is in reasonable agreement with the trap depths estimated for CdSe/CdS core-shell structures in [200]. The deposition of approximately 20 nm of alumina by 200 ALD cycles effectively protects the NC film from degradation due to oxidation at elevated temperatures, which indicates an effective sealing from the gases present in ambient atmosphere.

### 7.7.2 Stability in Air:

The ALD coating process with alumina is also able to protect the nanocrystal surface from degradation under ambient conditions for extended periods of time. Figures 7.11 (e,f) show the PL peak intensity, normalized to its value measured directly after film preparation, after 3 months of sample storage for different number of ALD cycles, i.e. for different amounts of alumina deposition that result in infilling and overcoating of the nanocrystal layer.

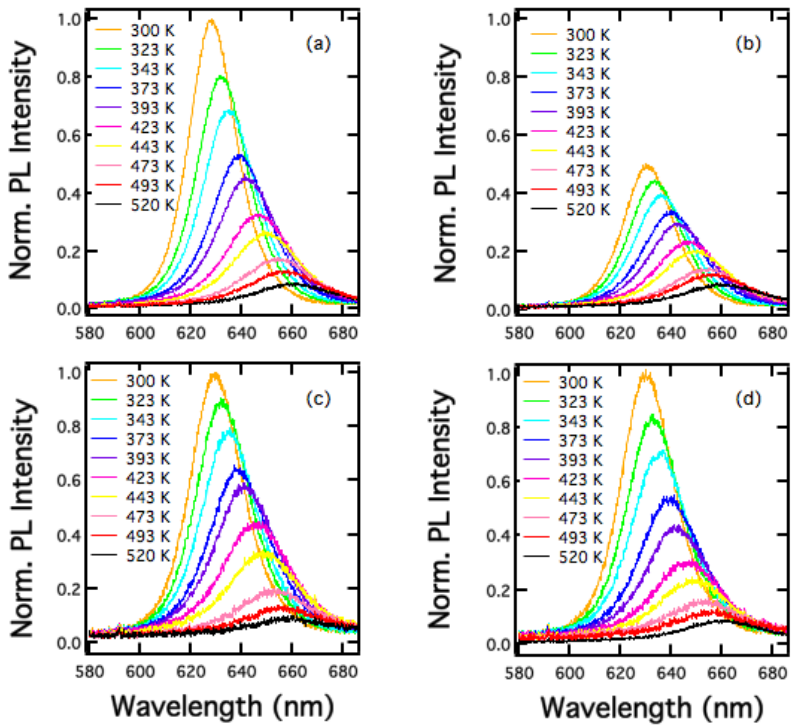


Figure 7.10. PL spectra recorded from non-coated DiR films (a-b), and from DiR films that were coated with 200 ALD cycles of alumina (c-d).

While partial filling of the nanocrystal layer does not increase the shelf stability, we clearly observe that overcoating the nanocrystal layer with 200 ALD cycles of alumina leads to stable emission intensity even after three months of sample storage. On the other hand, ALD infilling and overcoating of the NC layers results in a reduction of the conductance of the film if measured in vertical configuration.

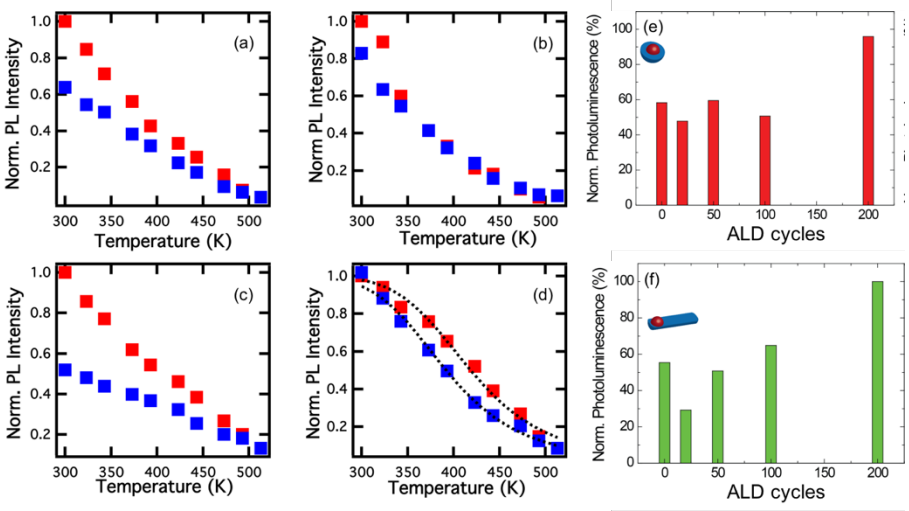


Figure 7.11. PL intensity versus temperature measured under ambient conditions for (a) non-coated DiD films, (b) DiD films coated by 200 ALD cycles of alumina, (c) non-coated DiR films and (d) DiR films coated by 200 ALD

cycles of alumina. (e,f) PL intensity recorded after 3 months of shelf time for nanocrystal films of DiDs (e) and DiRs (f) that were coated with different number of ALD cycles.

## 7.8 Chapter Summary:

We reported the fabrication of composite colloidal nanocrystal/alumina films in which the infilling and overcoating regimes of the nanocrystal layer can be controlled precisely by ellipsometry. In the infilling regime, the dielectric constant of the composite film can be tuned by the amount of deposited alumina. PL intensity and decay dynamics recover close to their original values for alumina overcoated films. The alumina overcoated nanocrystal films manifest robust and stable PL emission, both over time and with respect to heating of the film. This improvement of the film stability enables post-processing of the films without deteriorating their emission, for example by lithography techniques and metal deposition. Together with the opportunity to tailor the optical properties like refractive index, these properties are highly advantageous for controlling, for example, the coupling to plasmonic structures that potentially can be fabricated on top of the overcoated films, and which can lead to increased performance in LEDs or in energy harvesting. Furthermore, robust layered structures are promising for applications in metamaterial based nano-lasers, nano-lenses and sensors where highly emissive and high-refractive index gain materials are required.

(Note: Results presented in this chapter are already published M. Palei et al., ACS Appl. Mater. Interfaces, 2018, 10 (26), pp 22356–22362, My personal contribution to this work includes sample fabrication and characterization, fluorescence spectroscopy measurements, temperature dependent PL measurements, ellipsometry analysis)

# Chapter 8

## Dye Inside a Planar Nanocavity: Coupling of Epsilon-Near-Zero Resonances with Excitons

### 8.1 Abstract:

Coupling between plasmons and emitters has attracted large interest. Plasmon-Exciton coupling gives rise to a mixed state that can be seen as a quasi-particle called "Plexciton".[59] Such a phenomenon has been demonstrated in nanostructured materials, manifesting strong light confinement at small volume, typically requiring very demanding nanofabrication processes. Here, we fabricate MIM cavities with emitters integrated in the insulator layer, thus in the region of the strongest field enhancement. The ENZ resonance of the MIM cavity is tuned to the emission wavelength of the emitters, which represent a necessary requisite to obtain strong coupling. The fabrication process followed the approach of fabricating planar nanocavities made of metal and insulator, where the emitting nanocrystal layer is embedded in the dielectric layer. By tuning the volume fraction of the emitter layer and cavity thickness, we achieved the resonance matching condition of the cavity resonance with the nanocrystal emission.

### 8.2 Introduction:

When two systems with equal natural frequency interact via an energy exchange channel, they hybridize their optical response and new coupled modes arise. The splitting of these hybrid modes directly depends on the coupling strength. The system is then said to be in the strong coupling regime.

Strong coupling phenomena are observed in several fields. Among these, Light-Matter interaction stands out to be promising and shows a wide variety of strong coupling interactions. Gruber et. al. have shown strong coupling between silver nanowire and quantum dots where the quantum dot emission is strongly enhanced.[204] Similarly, strong coupling between localized surface plasmon and excitons has been demonstrated in a silver nano-shell geometry.[205] Strong mode splitting in photoluminescence have been demonstrated recently for a single silver nanoprism coupled to quantum dot, which manifests plasmon-exciton coupling in a hybrid system.[206] One possible alternative to such complicated nano-structures is constituted by systems showing optical transitions at the same frequency as the exciton. Among these, the ENZ MIM cavities considered in this work are very good candidates.

In Chapter 4 we have demonstrated strong coupling between two stacked passive MIM cavities. FEM analysis carried out in chapter 4 for MIM superabsorber suggests that, in the case of the even mode, the electric field confined inside the cavity is maximum at the center of the dielectric core.

Hence embedding the fluorophore inside the MIM and MIMIM nanocavities constitutes the most promising condition to reach the highest energy exchange between the fluorophores and the cavity.

The exciton-ENZ mode coupling has been investigated by Photoluminescence Excitation (PLE) of the fluorophore embedded in the cavity. This analysis reveals the occurrence of a new peak, that may be ascribed to the hybridization of the high energy ENZ mode and the exciton. These preliminary results constitute the basis for a more detailed analysis on the ENZ-exciton strong coupling regime.

## 8.3 Materials and Methods:

### 8.3.1 Fabrication of MIM and MIMIM

MIM and MIMIM multilayers have been fabricated via a combined e-beam (PVD 75 from Lesker) /ALD (FlexAL from Oxford Instruments) multistep procedure, including the deposition of a QDs layer via spin-coating.

Step 1: Ag (30nm) is deposited via E-beam evaporation.

Step 2: $Al_2O_3$ (50nm) bilayer is deposited via E-beam evaporation on the top of the Ag layer.

Step 3: A CdSe/ZnS (DID) quantum dot layer is spin-coated above the $Al_2O_3$ layer.

Step 4: On the top of the QDs layer, a second 50nm $Al_2O_3$ film is deposited by means of thermal ALD at 110 °C.

Step 5: A 30nm Ag layer is deposited via E-beam evaporation.

This completes one MIM stack with an embedded emitter layer. The procedure is repeated on the top of the MIM, starting from step 2, in order to create a MIMIM structure.

**ALD of Alumina***:* Atomic layer deposition was carried out in a Flexal ALD system from Oxford Instruments, using a thermal process with a stage temperature of 110 °C, resulting in an alumina deposition rate of 0.09 nm/cycle. Tri-methylaluminate (TMA) and $H_2O$ were used as precursors, and we performed a pre-heating step for 300 s before stating the ALD cycles. Each cycle consisted of a $H_2O$/purge/TMA/purge with a pulse durations of 0.075/6/0.033/2 seconds, respectively.

**8.3.2 Nanocrystal Materials:** CdSe/ZnS DiDs stabilized with octadecylamine ligands were purchased from Sigma Aldrich (product number 790192) and dispersed in toluene with a concentration of 5mg/mL. TEM, PL and absorbance of CdSe/ZnS DiDs (in toluene) are shown in figure 8.1.

*Film preparation:* The DID films were spin-coated on glass substrates at 3000 rpm for 1 minute, which resulted in a thickness of 25±2 nm. The film thickness was measured with a Dektak profilometer.

### 8.3.3 Ellipsometry on MIM and MIMIM with an Embedded QD layer

The characterization of the optical properties of all the fabricated multilayer structures has been conducted by spectroscopic Ellipsometry with a Vertical Vase ellipsometer by Woollam, in the range from 300-900 nm. We analyzed both delta and psi step by step, after each layer is formed in MIM and MIMIM, which will give information about the thickness of each layer and hence the whole cavity in order to match with resonance of the cavity with fluorophore emission band. Spectroscopic analysis has been carried out at three different angles (50°, 60° and 70°) with a step of 3 nm. P-Polarized reflectance and transmittance measurements have been performed via ellipsometry, in a broad range of angles, which comprises the case of 40° discussed in this work. The resolution for recording the spectra was 3 nm, and all spectra have been normalized to the intensity of the Xe lamp.

### 8.3.4 Fluorescence Spectroscopy

PL and PLE measures on MIM and MIMIM with an embedded QD layer were taken with an Edinburgh Instruments fluorescence spectrometer (FLS920), which included a Xenon lamp with monochromator for steady-state PL excitation. The PL spectra recorded from MIM and MIMIM structures were obtained with an excitation wavelength of 400 nm by keeping excitation and emission slit width fixed at 2 nm and 1 nm, respectively. The spectra were recorded with 2 nm resolution and 0.5 second dwell time. PLE spectra were recorded keeping the emission at 620 nm and the excitation range from 400 to 600 nm. All the measurements were carried out on substrate of dimensions 1.6×1.3 $cm^2$ at an excitation wavelength of 400 nm.

## 8.4 Results and Discussions:

### 8.4.1 Spectroscopic Ellipsometry on MIM and MIMIM with an Embedded QD Layer

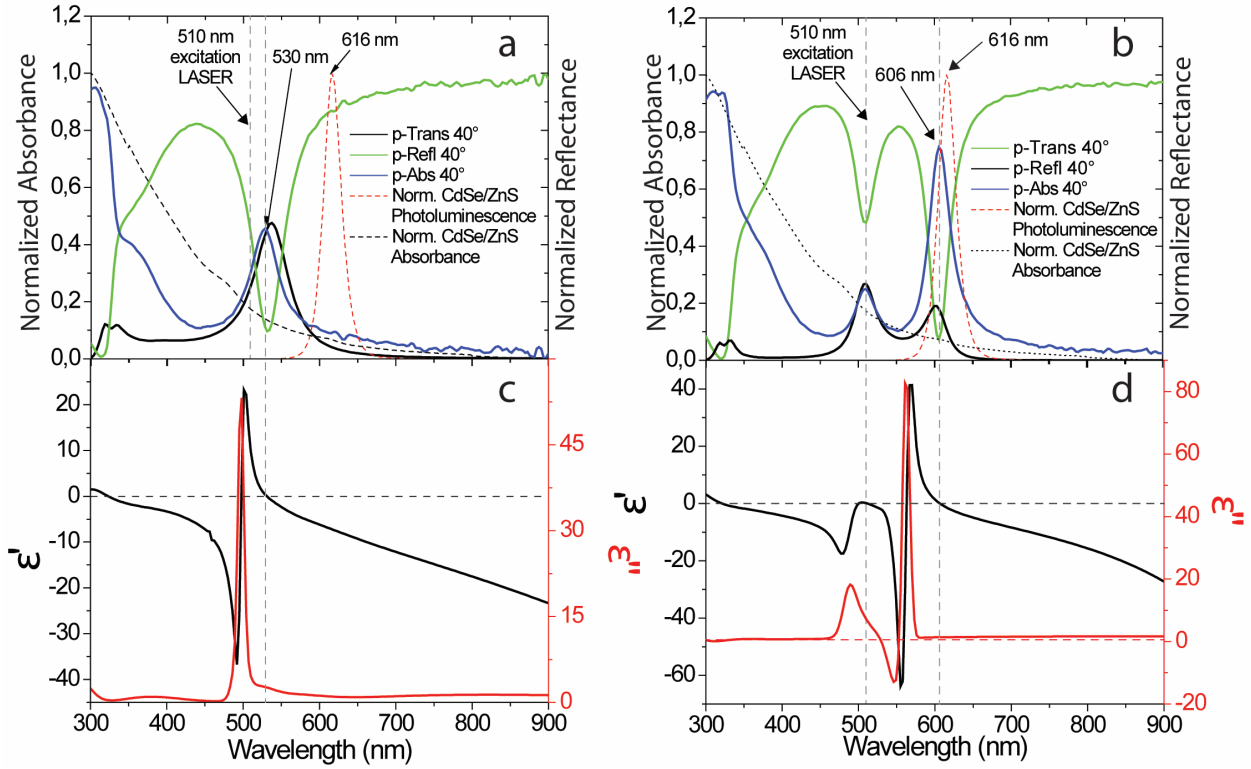


Figure 8.1 (a,b) Shows p-polarized transmittance, reflectance, absorbance at 40º for MIM (a) and MIMIM (b) nanocavities with an embedded DID layer in the insulator layer, compared to the normalized PL and absorbance of the CdSe/ZnS DID nanocrystal layers. (c,d) Real and imaginary of dielectric constant over a spectral range from 300 to 900 nm for MIM (c) and MIMIM (D) structures with NC films embedded inside.

Figures 8.1a and 8.1b show the p-polarized reflectance (R) and transmittance (T) measured via ellipsometry at a grazing angle of 40° for the MIM and MIMIM nanocavities. The absorbance (A) was then calculated as A=1-(T+R). For the MIM structure, a maximum in absorbance is detected very close to the dip in reflection (Figure 8.1a) which corresponds to the even ENZ mode at 530 nm. For the MIMIM system, two ENZ modes are observed (Figure 8.1b) at 510nm (odd mode) and at 606nm (even mode). Both MIM and MIMIM show a peak in absorbance at 327nm which is attributed to the well-known Ferrel-Berreman mode of silver. By embedding a layer of QDs, the MIM and MIMIM systems are no more like passive as described in chapter 5 and 6. In order to demonstrate the ENZ behavior of the resonance, a direct measurement of real and imaginary dielectric permittivity has been performed with the help of spectroscopic ellipsometer as shown in Figure 8.1c and d. The ellipsometric investigation of optical response of MIM and MIMIM with the DID layer embedded inside allows for homogenization of their dielectric permitivities, which means that the optical properties of the multilayer of metal/dielectric/DID layer can be described by homogenized permittivity function. For the MIM with DID layer embedded inside, the low-

loss ENZ mode is at $\lambda = 530nm$, called the $ENZ_1$ mode, where the maximum in absorbance was found. For the MIMIM with two DID layers sandwiched in each dielectric layer, two low-loss ENZ modes (absorbance maxima) are detected apart from the low loss Ferrel-Berreman mode at 327, which are called $ENZ_1$ and $ENZ_2$ mode at 510 nm and 606 nm, respectively.

## 8.5 Chapter Summary:

In this chapter, we introduced simple realization of effective coupling between ENZ mode of MIM and MIMIM planar nanocavities with excitons of semiconductor QDs. A simple fabrication steps involving several deposition techniques are highlighted. The cavity resonances of MIM and MIMIM system are successfully tuned to QDs absorption and emission band in order to achieve maximum coupling between them. This paves the way of complicated nanostructuring processes, which has been a conventional technique to achieve strong coupling in light matter interaction. However, detail analysis related to fluorescent spectroscopic measurement are yet to be monitored. Understanding novel optical properties of such hybrid structure and simultaneously uncovering the hidden novelty of ENZ coupling with exciton will be the future direction of the work.

# Chapter 9

## Summary and Outlook:

In this thesis we have shown that MIM nanocavities can be used to tune the electromagnetic waves at frequencies in the visible, in a broad spectral range. We demonstrated that the resonant modes of MIM structures are low loss ENZ resonances. Thereby we circumvented the difficulty involved in realization of ENZ material in the visible. Moreover, the low loss ENZ mode are radiative by nature, and lead to a strong enhancement of the photonic density of states (PDOS). Coupling and hybridization of ENZ modes has been demonstrated in a more complicated system where one MIM cavity is placed above the other. These novel properties are further explored by coupling ENZ modes in MIM and MIMIM structures to fluorophores both placed above and inside the cavity. The planar and more straight forward fabrication technique involved in MIM and MIMIM hybrid system are promising for 'flatland photonics' devices.

We investigated and discussed the resonant tunneling of photons in a layered metal/insulator/metal (MIM) quantum well system comprising of silver as metal layer and alumina as dielectric layer (chapter 6). An analogy between tunneling of electrons and photons has been discussed. The tunneling of a photon in a metal/insulator/metal system is analogous to the tunneling phenomena ocurring for electrons in a tunnel diode. Here, for photons, the square of the imaginary part of the refractive index of the metal layer behaves like an optical barrier potential. We experimentally verified that these resonant tunneling modes coincide with low loss ENZ modes and they can be tuned in the whole visible range by changing the dielectric layer thickness. Further investigation in this direction revealed that asymmetric MIM structures with a thick bottom metal layer acts as a superabsorber, and can be used as a versatile refractive index sensor. Moreover, strong hybridization of ENZ resonances has been demonstrated for coupled MIMIM systems, evidenced by mode anticrossing. We demonstrated how the strong interaction of the two MIM nano-resonators composing the MIMIM takes place via the shared central Ag layer, which leads to a strong hybridization of the resonant modes, experimentally found in the order of 6 times the linewidth of the resonances, optimizable up to 20 times, as demonstrated theoretically. The narrow mode linewidth, together with the high versatility of the MIMIM that allows fine positioning of the ENZ modes in the entire visible range, makes such systems an ideal platform for exploring the weak and strong coupling between ENZ modes and excitons. The plasmonic nature of ENZ resonances is further exploited in chapter 6, where spontaneous emission of perovskites nanocrystals is enhanced by coupling to the planar nanocavities of MIM and MIMIM. We noticed a 1.5 times enhancement in PLQY and 3 times enhancement in radiative decay rate in perovskites nanocrystal by coupling to MIMIM nanocavities.

Further, COMSOL simulation infer that the highest field enhancement is within the dielectric layers in the MIM and MIMIM nanocavities. This encouraged us to embed the emitter inside these

layers. However, the optical properties of colloidal NCs are strongly modified when surrounded by a different medium, which was the prime concern before embedding such emitters inside the cavity. Hence, in chapter 7 we demonstrated the fabrication of a composite film of alumina and nanocrystals, which is a necessary requisite for embedding it inside MIM and MIMIM nanocavities, and retaining the nanocrystal optical properties. We noticed a full recovery of photoluminescence properties of alumina/NCs composite films that were obtained by coating the NC film with few nanometers of alumina layer. Coating with alumina slightly enhances the refractive index of the composite layer and hence, which can be advantageous for lasing and other optical devices. Moreover, long term stability has been demonstrated for alumina/NCs composite systems both in ambient and after heating processes up to 200°C, which increases their compatibility with fabrication processes and enables wide application in solid state optical and plasmonic devices. This allows us to make hybrid MIM and MIMIM nanocavities with quantum dot layers embedded inside, as shown in chapter 8. We achieved low loss resonance matching conditions between ENZ modes of the MIM and MIMIM structures to the absorbance and emission of NCs.

Looking towards the future, epsilon near zero materials hold a great promise for future application in the field of quantum communication. There has been recent development of optical analogues of a lumped circuit element, where optical elements act as effective optical inductors, capacitors and resistors. Such optical circuitry requires the photonic equivalent of electrical wires that can carry optical frequency signals to and from the lumped circuit elements, with signal carrier wavelengths much larger than the size of the lumped elements. In this regard, metal/insulator/metal systems set an ideal platform. Together with their ENZ behavior, nanostructured MIM systems can be coupled easily to the free space radiation without any momentum matching, which gives immense advantages for transmission of optical signals both inside and outside of the nanocavity. Metal/insulator/metal systems have the potential to provide a key component and a realistic framework for designing optical circuitry. Moreover, epsilon-near-zero materials have become quite important for controlling the propagation of the light and it's enhancement by several order of magnitude. Given this advance, it is very important to look for various quantum electrodynamic processes and information tasks near the ENZ materials. It is shown that with ENZ materials, a significant entanglement can be achieved over larger distances than for simple metallic films. MIM and MIMIM structures as planar systems provide an ideal platform for such quantum information processes. For example, one can study the entanglement between two two-level systems near the MIM and MIMIM ENZ cavities. Further, MIM and MIMIM hybrid systems with nanocrystals layer embedded inside hold great promise for efficient light matter coupling. In this thesis we established a method on how to integrate light emitting nanocrystal layers into MIM and MIMIM cavities. The next objective is to investigate if strong coupling, i.e. mode anticrossing, between the ENZ resonance and the emission of the nanocrystals can be achieved. We already have some promising, preliminary results on new peaks in the absorbance of such a composite structure that we obtained by PL excitation spectroscopy, and where we discerned additional peaks. These

observations need more detailed investigation. Furthermore, lateral structuring of the MIM and MIMIM systems will be highly interesting, and should provide novel properties and possibilities for light matter coupling.

# Appendix A

## Polarization Dependent Plasmon Enhanced Fluorescence of Nanocrystals on Anisotropic Gold Nanostructures

### A.1 Fabrication of Gold Nanostructure:

The gold nanostructures obtained by shadow evaporation on etched glass substrates were provided by the group of Prof. Buatier. Detailed information about the sample fabrication can be found in the work of Repetto et. al. [207] The substrates are cut in to pieces of size 5×5 $mm^2$ and cleaned with gentle flow of nitrogen gas. They are further analyzed by SEM to rule out any possible damage during cutting. Figure A.2a shows SEM micrograph of the nanostructured substrate.

### A.2 CdSe/ZnS Nanocrystal Material:

CdSe/ZnS DiDs stabilized with octadecylamine ligands were purchased from Sigma Aldrich (product number 790192) and dispersed in toluene with a concentration of 5mg/mL. TEM, PL and absorbance of CdSe/ZnS DiDs (in toluene) are shown in figure 8.1.

### A.3 Monolayer Film Deposition on Nanostructured Substrate:

Langmuir Blodgett troughs made from teflon with a volume capacity of 15 mL were filled with 8 mL of diethylene glycol. 20 $\mu$L of DiD NCs solution in hexane (1 mg/mL) were drop-cast on the top of diethylene glycol and the wells were covered for 10 minutes to ensure slow evaporation of hexane. Then the cover was removed, and the residual hexane was left to evaporate. After this, a yellow-colored floating film was formed over diethylene glycol. The film was fished from the solution with a nanostructured substrate of size 5×5 $mm^2$, and dried on a hot plate at 80 °C to remove any remaining glycol.

### A.4 Fluorescence Spectroscopy on Monolayer of DID Deposited over Nanostructured Gold Substrate

PL on nanocrystals in solution and in films were carried out with an Edinburgh Instruments fluorescence spectrometer (FLS920), which included a Xenon lamp with monochromator for steady-state PL excitation. The PL spectra recorded from films on nanostructured surface were obtained with an excitation wavelength of 405 nm diode laser by keeping excitation slit full and emission slit width fixed at 10 nm. The spectra were recorded with 2 nm resolution and 0.5 second dwell time. Time resolved PL decay was studied with a time-correlated single-photon-counting unit coupled to a pulsed diode laser. The PL decay traces were recorded by exciting the sample at 405 nm with a 50 ps pulse at a repetition rate of 0.05 – 1 MHz. The signal was collected at PL peak wavelength with a bandwidth of 10 nm. All the measurements were carried out on monolayer DID

films on nanostructured gold substrate deposited by Langmuir Blodgett approach and with dimensions of 5×5 $mm^2$ at an excitation wavelength of 405 nm.

## A.5 Results and Discussions:

Here we used anisotropic gold nanostructure of thickness 22 nm and pitch 80 nm. LSPRs of such nanostructure are tuned to 620 nm in a substrate size of 5×5 $mm^2$ as shown by reflectance spectra in figure A.1b. This overlap in frequency enables to couple to fluorophores whose emission maximum tuned to LSPRs of our gold nanostructure. However, the roughness and fragile nature of the gold nanostructures hinders the possibility of surface coating by means of spin coating. In order to overcome this issue, we adopted a Langmuir-Blodgett approach as explained in detail above. Figures A.1c,d show SEM micrographs of monolayer CdSe/ZnS DID film over nanostructure gold substrate coated by 5nm of alumina layer deposited by atomic layer deposition (ALD). The thin layer of alumina helps to avoid possible quenching due to metal. The nanostructured gold wires are known to have polarization dependent LSPRs response.

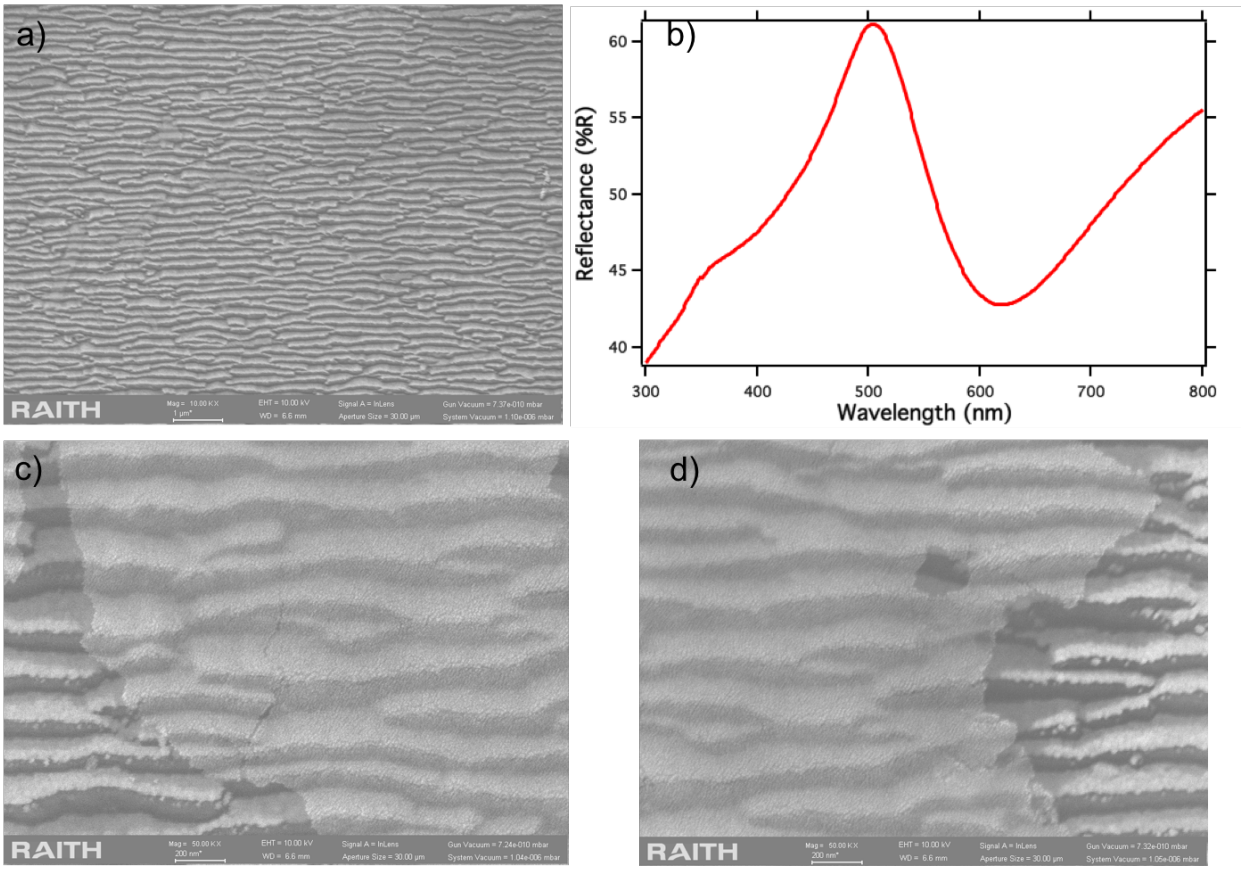


Figure A.1 a) Scanning electron micrograph of nanostructured gold substrate b) Reflectance spectra taken at normal incidence with Cary 5000 spectrometer c,d) Scanning electron micrograph of monolayer CdSe/ZnS Dots-in-Dots deposited on nanostructured gold substrate

We probe both photoluminescence and lifetime of the DiD film by analyzing the polarization dependence of the emission. Figure A.2 shows experimental set up for the measurement of PL and lifetime. The set up includes a diode laser at 405 nm passing through a quarter wave plate (QWP) oriented at 45° with its fast axis to the linear polarization of the laser. This gives a circular polarized beam which further passed through a lens before it is incident on the sample. Circular polarized light in the incidence was chosen in order to avoid any linear polarization influence from the excitation source.

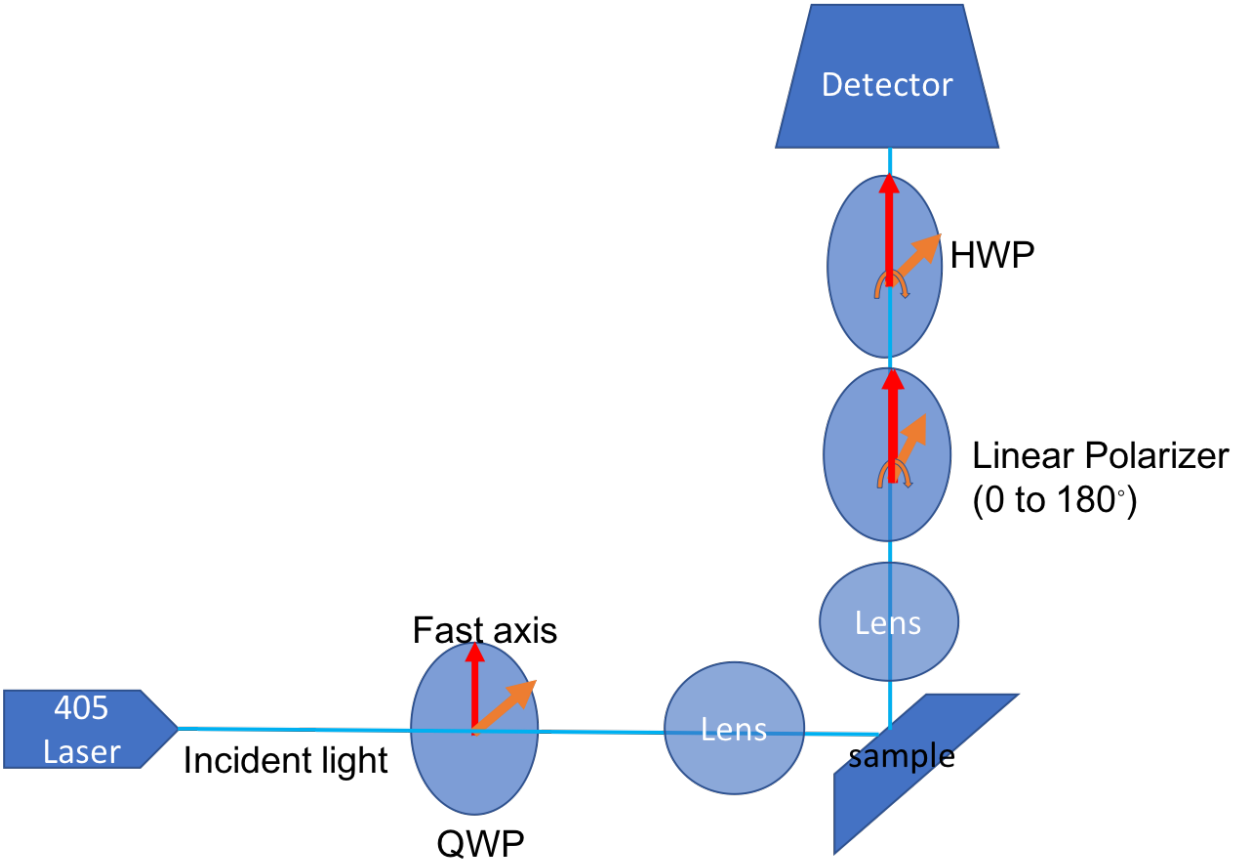


Figure A.2 Experimental setup for polarization dependent photoluminescence and lifetime measurements of DiD films on a nanostructured gold surface.

The emission was detected in reflection mode using a lens, linear polarizer and a half wave plate (HWP) before it reaches to the detector. The linear polarizer is used to analyze the polarization of the emitted light, and the half wave plate (HWP) was used to restore the polarization alignment with respect to the detector, i.e. the linear grating of the spectrometer.

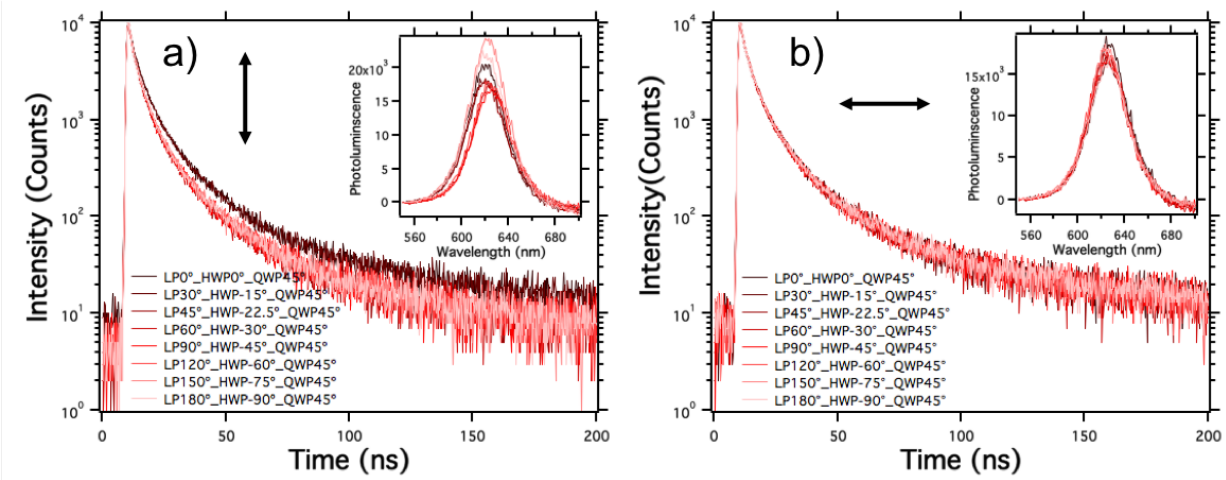


Figure A.3 Experimentally measured photoluminescence and decay lifetime with a circular polarized light (405nm) at excitation and by analyzing the linear polarization in detection a) NW axis perpendicular b) NW axis parallel to the 0° axis.

Although we would have expected and increased PL intensity and decreased lifetime when the polarizer was oriented perpendicular to the gold nanowire axis, i.e. when the emission polarization is in resonance with the LSPR of the nanowire structure, we did not observe any distinct polarization dependence. This was verified by rotating the sample by 90° with respect to the optics (as in Fig. A.3 (b)), which revealed that discrepancies in the signal were not systematic with the polarization angle.

# Appendix B
## Tunneling of photons through a potential barrier

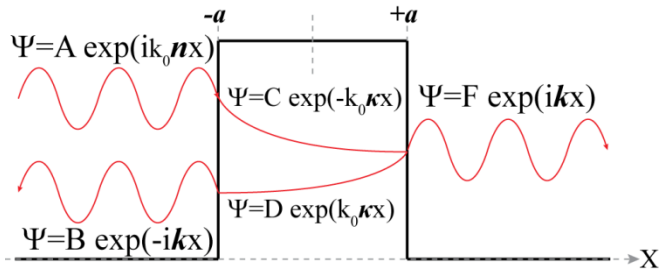


Figure B1. Sketch of the photonic tunneling configuration. The thin metal layer represents the optical potential barrier. Since the real part of the refractive index of the metal is negligible with respect to the imaginary one, the propagation through the metal is purely evanescent. The thickness of barrier is given by the physical thickness of the metal layer.

The Schrödinger equation outside the barrier, i.e. in the dielectric, is the one of a free particle:

$$\frac{d^2\Psi}{dx^2} + \boldsymbol{k}_d^2\Psi = 0 \qquad \text{(B1)}$$

$\boldsymbol{k}_d = k_0 n$ , where $k_0 = 2\pi/\lambda$ and $n$ is the refractive index of the dielectric in which the propagation takes place. Since $n$ is a real number, the solutions of Equation B1 assume the form of a complex exponential, representing an harmonic propagating wave. The wavefunction outside the barrier results, therefore, equal to:

Region I:

$$A\exp(ik_0 nx) + B\exp(-ik_0 nx) \qquad \text{(B2)}$$

Region III:

$$F\exp(ik_0 nx) \qquad \text{(B3)}$$

The Schrödinger equation in Region II, in the barrier, is can be written as:

$$\frac{d^2\Psi}{dx^2} - \boldsymbol{k}_M^2\Psi = 0 \qquad \text{(B4)}$$

being $k_M = ik_0\kappa$, it follows that $(k_M)^2 = -(k_0\kappa)^2$ , such that solutions of Equation B4 are decaying exponentials in Region II, i.e. inside the barrier:

Region II:

$$B\exp(-k_0\kappa x) + C\exp(k_0\kappa x) \qquad \text{(B5)}$$

By applying suitable boundary conditions to the wavefunctions and their derivatives at the interfaces, we obtain the following set of equations, as depicted in Figure B1:

$$\begin{cases} A + B = C + D; \\ ik_D(A + B) = -k_0\kappa(C - D); \\ C\exp(-k_0\kappa a) + D\exp(k_0\kappa a) = F\exp(ik_D a) \\ -k_M(C\exp(-k_0\kappa a) - D\exp(k_0\kappa a)) = ik_D F\exp(ik_D a) \end{cases} \quad \text{(B6)}$$

where $k_D = k_0 n$. This system can be solved for the quantity F/A that represents the transmissivity of the system. The tunneling probability through the barrier is then equal to $|F/A|^2$ :

$$\left|\frac{F}{A}\right|^2 = \frac{4(k_0\kappa)^2 k_D^2}{((k_0\kappa)^2 + k_D^2)^2 \sinh^2(k_0\kappa a) + 4(k_0\kappa)^2 k_D^2} \quad \text{(B7)}$$

Even though Equation B7 provides the exact solution for the *tunneling probability* through the barrier, it is usually approximated by the more convenient expression:

$$\left|\frac{F}{A}\right|^2 \cong \exp(-2k_0\kappa a) \quad \text{(B8)}$$

Equation B8 expresses the approximated tunneling probability of a photon through a metallic barrier.

# Appendix C
## Bound Modes and Quasi-bound Modes of Metal-Insulator-Metal (MIM) System

### C.1 Bound Modes for a Thick Metal Barriers Potential Well

A MIM cavity composed by a dielectric core of thickness $t_D$ and real refractive index $n_D$ , and two metal layers with thickness $t_M$ (that is much higher than their skin depth) and an imaginary refractive index $k_M$ can be modeled as a finite potential well with infinitely thick barriers as depicted in Figure C1a:

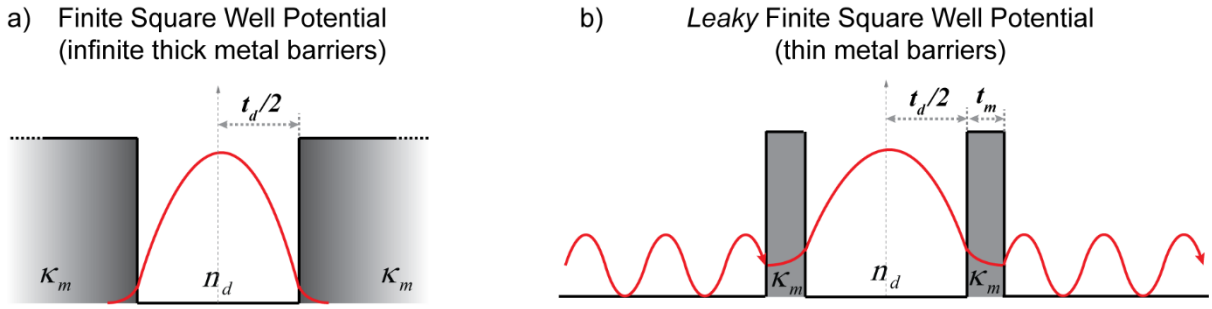


Figure C1. Sketch of the Finite Square Potential Well (FSPW) configuration with infinite thickness of the metal layers that reproduces with high accuracy the resonance frequencies of a MIM with thick metallic layers. The exact dispersion relation for these modes is given in Equation C6 and Equation C7. The even mode confined in the MIM has the shape sketched in red. (b) Sketch of the Leaky MIM that can be modeled by a double barrier potential well. In this case, the two potential barriers are too thin to lead to truly bound modes, such that quasi-bound modes with a dispersion relation described in Equation C10 and Equation C11 have to be used. This case models with very high accuracy the resonances of the Leaky MIM, in which the thickness of the metal layers is comparable to their skin depth.

The Schrödinger equation in the dielectric medium is expressed in Equation B1 and returns harmonic propagating waves, while in the metallic claddings the wavefunction decays exponentially, since the Schrödinger equation in this region is the one reported in Equation B4. The particular symmetry of the geometry of the problem as modeled in Figure C1a allows to look for symmetric and antisymmetric modes, considering only one half of the cavity. Therefore, in the dielectric core, the wavefunction is equal to:

$$\Psi(x)_{even} = A\cos(k_D x); \tag{C1}$$

$$\Psi(x)_{odd} = A\sin(k_D x); \tag{C2}$$

while in the metallic layers the wavefunction decays exponentially:

$$B\exp(-k_0 \kappa x), \tag{C3}$$

An intrinsic expression for the dispersion relation of the even modes of the MIM cavity can be found by setting the equivalence between Equation C10 and C11 and of their derivatives at the interface of the two domains:

$$\begin{cases} A\cos(k_D\frac{t_D}{2}) = B\exp(-k_0\kappa\frac{t_D}{2}) & \text{(C4)} \\ A\,k_D\sin(k_D\frac{t_D}{2}) = -k_M\,B\exp(-k_0\kappa\frac{t_D}{2}) & \text{(C5)} \end{cases}$$

Dividing Equation C5 by Equation C4:

$$\tan(k_0 n_D\frac{t_D}{2}) = \frac{\kappa}{n_D}, \quad \text{(C6)}$$

Equation C6 equals Equation (6.3) of the main text, and can be solved graphically so that the crossing points between the two curves are the even modes of the MIM nano-cavity with very thick metal layers. When looking for odd modes, Equation C2 has to be considered instead of Equation C1, leading to:

$$-\cot(k_0 n_D\frac{t_D}{2}) = \frac{\kappa}{n_D}, \quad \text{(C7)}$$

Equation C7 is equal to Equation (6.4) of the main text, and represents the dispersion relation for the antisymmetric modes of the MIM cavity with thick metal walls.

## C.2 Bound Modes for a Thin Metal Barriers Potential Well

When the thickness of the metal layers approaches the skin depth of the metal, a new scenario opens, in which the MIM can be modeled as a leaky cavity. Indeed, since photons can escape the quantum well, the modes are quasi-bound. It is still possible to find eigenstates of the leaky MIM. Since the wavefunction does not go to zero in the metal layers, an additional phase component has to be added. This phase delay is equal to the tunneling probability of the photon through the metal barrier as expressed in Equation B8. The most convenient way to take this contribution into account is by directly adding the tunneling phase component to the wavefunctions in Equation C1 and C2:

$$\Psi(x)_{even} = A\cos(k_D x + \exp(-2k_0\kappa_M t_M)); \quad \text{(C8)}$$

$$\Psi(x)_{odd} = A\sin(k_D x + \exp(-2k_0\kappa_M t_M)); \quad \text{(C9)}$$

Such approximation leads to the modified dispersion relation for the quasi-bound symmetric, Equation 6.5, and antisymmetric, Equation 6.6, modes of the *leaky* MIM cavity discussed in the main text:

$$\tan(k_D\frac{t_D}{2} + \exp(-2\,k_0\kappa_M t_M)) = \frac{\kappa_M}{n_D}, \quad \text{(C10)}$$

$$-\cot(k_D \frac{t_D}{2} + \exp(-2k_0\kappa_M t_M)) = \frac{\kappa_M}{n_D}, \tag{C11}$$

# Bibliography:


1. Shvartsburg, A.; Kuzmiak, V.; Petite, G., Optics of subwavelength gradient nanofilms. *Physics Reports* **2007,** *452* (2-3), 33-88.
2. Fornel, F., Evanescent waves from Newtonian optics to atomic optics, 2001. Springer-Verlag, Berlin). Google Scholar.
3. De Abajo, F. G.; Gomez-Santos, G.; Blanco, L.; Borisov, A.; Shabanov, S., Tunneling mechanism of light transmission through metallic films. *Physical review letters* **2005,** *95* (6), 067403.
4. Shelby, R. A.; Smith, D. R.; Schultz, S., Experimental verification of a negative index of refraction. *science* **2001,** *292* (5514), 77-79.
5. Zhou, X.; Hu, G., Total transmission condition for photon tunnelling in a layered structure with metamaterials. *Journal of Optics A: Pure and Applied Optics* **2006,** *9* (1), 60.
6. Yeh, P., *Optical waves in layered media*. Wiley-Interscience: 2005; Vol. 61.
7. Griffiths, P.; De Haseth, J., Fourier transform infrared spectroscopy, 671 p. Wiley, New York: 1986.
8. Reddick, R. C.; Warmack, R.; Chilcott, D.; Sharp, S.; Ferrell, T., Photon scanning tunneling microscopy. *Review of scientific instruments* **1990,** *61* (12), 3669-3677.
9. Zhang, Z.; Fu, C., Unusual photon tunneling in the presence of a layer with a negative refractive index. *Applied Physics Letters* **2002,** *80* (6), 1097-1099.
10. Silveirinha, M. G.; Engheta, N., Theory of supercoupling, squeezing wave energy, and field confinement in narrow channels and tight bends using ε near-zero metamaterials. *Phys Rev B* **2007,** *76* (24), 245109.
11. Silveirinha, M.; Engheta, N., Tunneling of electromagnetic energy through subwavelength channels and bends using ε-near-zero materials. *Physical review letters* **2006,** *97* (15), 157403.
12. Maas, R.; Parsons, J.; Engheta, N.; Polman, A., Experimental realization of an epsilon-near-zero metamaterial at visible wavelengths. *Nat Photonics* **2013,** *7* (11), nphoton. 2013.256.
13. Colvin, V.; Schlamp, M.; Alivisatos, A. P., Light-emitting diodes made from cadmium selenide nanocrystals and a semiconducting polymer. *Nature* **1994,** *370* (6488), 354.
14. Fan, F.; Voznyy, O.; Sabatini, R. P.; Bicanic, K. T.; Adachi, M. M.; McBride, J. R.; Reid, K. R.; Park, Y.-S.; Li, X.; Jain, A., Continuous-wave lasing in colloidal quantum dot solids enabled by facet-selective epitaxy. *Nature* **2017,** *544* (7648), 75.
15. Sargent, E. H., Colloidal quantum dot solar cells. *Nat Photonics* **2012,** *6* (3), 133.
16. Klimov, V. I., *Nanocrystal quantum dots*. CRC Press: 2010.
17. Osterloh, F. E., Inorganic materials as catalysts for photochemical splitting of water. *Chem Mater* **2007,** *20* (1), 35-54.
18. Huxter, V. M.; Scholes, G. D., Photophysics of colloidal semiconductor nanocrystals: A review. *Journal of Nanophotonics* **2009,** *3* (1), 032504.
19. Klimov, V. I.; McBranch, D. W., Femtosecond 1 P-to-1 S electron relaxation in strongly confined semiconductor nanocrystals. *Physical Review Letters* **1998,** *80* (18), 4028.

20. Hendry, E.; Koeberg, M.; Wang, F.; Zhang, H.; de Mello Donega, C.; Vanmaekelbergh, D.; Bonn, M., Direct observation of electron-to-hole energy transfer in CdSe quantum dots. *Physical review letters* **2006,** *96* (5), 057408.
21. Bawendi, M. G.; Carroll, P.; Wilson, W. L.; Brus, L., Luminescence properties of CdSe quantum crystallites: Resonance between interior and surface localized states. *The Journal of Chemical Physics* **1992,** *96* (2), 946-954.
22. Klimov, V. I., Spectral and dynamical properties of multiexcitons in semiconductor nanocrystals. *Annu. Rev. Phys. Chem.* **2007,** *58*, 635-673.
23. Zhao, H.; Chaker, M.; Wu, N.; Ma, D., Towards controlled synthesis and better understanding of highly luminescent PbS/CdS core/shell quantum dots. *Journal of Materials Chemistry* **2011,** *21* (24), 8898-8904.
24. Peng, X.; Schlamp, M. C.; Kadavanich, A. V.; Alivisatos, A. P., Epitaxial growth of highly luminescent CdSe/CdS core/shell nanocrystals with photostability and electronic accessibility. *Journal of the American Chemical Society* **1997,** *119* (30), 7019-7029.
25. Sambur, J. B.; Parkinson, B. A., CdSe/ZnS core/shell quantum dot sensitization of low index TiO2 single crystal surfaces. *Journal of the American Chemical Society* **2010,** *132* (7), 2130-2131.
26. Dabbousi, B. O.; Rodriguez-Viejo, J.; Mikulec, F. V.; Heine, J. R.; Mattoussi, H.; Ober, R.; Jensen, K. F.; Bawendi, M. G., (CdSe) ZnS core− shell quantum dots: synthesis and characterization of a size series of highly luminescent nanocrystallites. *The Journal of Physical Chemistry B* **1997,** *101* (46), 9463-9475.
27. Hines, M. A.; Guyot-Sionnest, P., Synthesis and characterization of strongly luminescing ZnS-capped CdSe nanocrystals. *The Journal of Physical Chemistry* **1996,** *100* (2), 468-471.
28. Liu, G.; Liu, Z.; Huang, K.; Chen, Y.; Li, L.; Tang, F.; Gong, L., Modified spontaneous emission from CdSe/ZnS core–shell quantum dots in plasmonic–photonic crystals. *Materials Letters* **2013,** *93*, 42-44.
29. Li, M.; Cushing, S. K.; Wang, Q.; Shi, X.; Hornak, L. A.; Hong, Z.; Wu, N., Size-dependent energy transfer between CdSe/ZnS quantum dots and gold nanoparticles. *The Journal of Physical Chemistry Letters* **2011,** *2* (17), 2125-2129.
30. Rabouw, F. T.; de Mello Donega, C., Excited-State Dynamics in Colloidal Semiconductor Nanocrystals. In *Photoactive Semiconductor Nanocrystal Quantum Dots*, Springer: 2017; pp 1-30.
31. Carbone, L.; Nobile, C.; De Giorgi, M.; Sala, F. D.; Morello, G.; Pompa, P.; Hytch, M.; Snoeck, E.; Fiore, A.; Franchini, I. R., Synthesis and micrometer-scale assembly of colloidal CdSe/CdS nanorods prepared by a seeded growth approach. *Nano Lett* **2007,** *7* (10), 2942-2950.
32. Sitt, A.; Salant, A.; Menagen, G.; Banin, U., Highly emissive nano rod-in-rod heterostructures with strong linear polarization. *Nano Lett* **2011,** *11* (5), 2054-2060.
33. Hadar, I.; Hitin, G. B.; Sitt, A.; Faust, A.; Banin, U., Polarization properties of semiconductor nanorod heterostructures: From single particles to the ensemble. *The journal of physical chemistry letters* **2013,** *4* (3), 502-507.
34. Rainò, G.; Stöferle, T.; Moreels, I.; Gomes, R.; Kamal, J. S.; Hens, Z.; Mahrt, R. F., Probing the wave function delocalization in CdSe/CdS dot-in-rod nanocrystals by time-and temperature-resolved spectroscopy. *ACS nano* **2011,** *5* (5), 4031-4036.
35. Saparov, B.; Mitzi, D. B., Organic–inorganic perovskites: structural versatility for functional materials design. *Chemical Reviews* **2016,** *116* (7), 4558-4596.

36. Kovalenko, M. V.; Protesescu, L.; Bodnarchuk, M. I., Properties and potential optoelectronic applications of lead halide perovskite nanocrystals. *Science* **2017,** *358* (6364), 745-750.
37. Imran, M.; Caligiuri, V.; Wang, M.; Goldoni, L.; Prato, M.; Krahne, R.; De Trizio, L.; Manna, L., Benzoyl Halides as Alternative Precursors for the Colloidal Synthesis of Lead-Based Halide Perovskite Nanocrystals. *Journal of the American Chemical Society* **2018,** *140* (7), 2656-2664.
38. Raether, H., Surface plasmons on smooth surfaces. In *Surface plasmons on smooth and rough surfaces and on gratings*, Springer: 1988; pp 4-39.
39. Kelly, K. L.; Coronado, E.; Zhao, L. L.; Schatz, G. C., The optical properties of metal nanoparticles: the influence of size, shape, and dielectric environment. ACS Publications: 2003.
40. Kneipp, K.; Wang, Y.; Kneipp, H.; Perelman, L. T.; Itzkan, I.; Dasari, R. R.; Feld, M. S., Single molecule detection using surface-enhanced Raman scattering (SERS). *Physical review letters* **1997,** *78* (9), 1667.
41. Willets, K. A.; Van Duyne, R. P., Localized surface plasmon resonance spectroscopy and sensing. *Annu. Rev. Phys. Chem.* **2007,** *58*, 267-297.
42. Huang, X.; El-Sayed, M. A., Plasmonic photo-thermal therapy (PPTT). *Alexandria journal of medicine* **2011,** *47* (1).
43. Pillai, S.; Catchpole, K.; Trupke, T.; Green, M., Surface plasmon enhanced silicon solar cells. *J Appl Phys* **2007,** *101* (9), 093105.
44. Debasu, M. L.; Ananias, D.; Pastoriza-Santos, I.; Liz-Marzán, L. M.; Rocha, J.; Carlos, L. D., All-in-one optical heater-thermometer nanoplatform operative from 300 to 2000 K based on Er3+ emission and blackbody radiation. *Advanced Materials* **2013,** *25* (35), 4868-4874.
45. Maier, S. A., *Plasmonics: fundamentals and applications*. Springer Science & Business Media: 2007.
46. Yariv, A., *Optical electronics*. Saunders College Publ.: 1991.
47. Maier, J., Nanoionics: ion transport and electrochemical storage in confined systems. *Nature materials* **2005,** *4* (11), 805.
48. Prade, B.; Vinet, J.; Mysyrowicz, A., Guided optical waves in planar heterostructures with negative dielectric constant. *Phys Rev B* **1991,** *44* (24), 13556.
49. Dionne, J.; Sweatlock, L.; Atwater, H.; Polman, A., Plasmon slot waveguides: Towards chip-scale propagation with subwavelength-scale localization. *Phys Rev B* **2006,** *73* (3), 035407.
50. Campione, S.; Brener, I.; Marquier, F., Theory of epsilon-near-zero modes in ultrathin films. *Phys Rev B* **2015,** *91* (12), 121408.
51. Vinogradov, A.; Dorofeenko, A.; Pukhov, A.; Lisyansky, A., Exciting surface plasmon polaritons in the Kretschmann configuration by a light beam. *Phys Rev B* **2018,** *97* (23), 235407.
52. Vassant, S.; Archambault, A.; Marquier, F.; Pardo, F.; Gennser, U.; Cavanna, A.; Pelouard, J.-L.; Greffet, J.-J., Epsilon-near-zero mode for active optoelectronic devices. *Physical review letters* **2012,** *109* (23), 237401.
53. Newman, W. D.; Cortes, C. L.; Atkinson, J.; Pramanik, S.; DeCorby, R. G.; Jacob, Z., Ferrell–Berreman modes in plasmonic epsilon-near-zero media. *Acs Photonics* **2014,** *2* (1), 2-7.
54. Caligiuri, V.; Palei, M.; Imran, M.; Manna, L.; Krahne, R., Planar Double-Epsilon-Near-Zero Cavities for Spontaneous Emission and Purcell Effect Enhancement. *ACS Photonics* **2018**.
55. Yablonovitch, E., Inhibited spontaneous emission in solid-state physics and electronics. *Physical review letters* **1987,** *58* (20), 2059.

56. Liu, G.-B.; Xiao, D.; Yao, Y.; Xu, X.; Yao, W., Electronic structures and theoretical modelling of two-dimensional group-VIB transition metal dichalcogenides. *Chemical Society Reviews* **2015,** *44* (9), 2643-2663.
57. Manjavacas, A.; Abajo, F. G. a. d.; Nordlander, P., Quantum plexcitonics: strongly interacting plasmons and excitons. *Nano Lett* **2011,** *11* (6), 2318-2323.
58. Chang, D.; Sørensen, A. S.; Hemmer, P.; Lukin, M., Quantum optics with surface plasmons. *Physical review letters* **2006,** *97* (5), 053002.
59. Cao, E.; Lin, W.; Sun, M.; Liang, W.; Song, Y., Exciton-plasmon coupling interactions: from principle to applications. *Nanophotonics* **2018,** *7* (1), 145-167.
60. Jun, Y. C.; Reno, J.; Ribaudo, T.; Shaner, E.; Greffet, J.-J.; Vassant, S.; Marquier, F.; Sinclair, M.; Brener, I., Epsilon-near-zero strong coupling in metamaterial-semiconductor hybrid structures. *Nano Lett* **2013,** *13* (11), 5391-5396.
61. Stokes, G. G., XXX. On the change of refrangibility of light. *Philosophical transactions of the Royal Society of London* **1852,** *142*, 463-562.
62. Abbyad, P.; Childs, W.; Shi, X.; Boxer, S. G., Dynamic Stokes shift in green fluorescent protein variants. *Proceedings of the National Academy of Sciences* **2007,** *104* (51), 20189-20194.
63. Akey, A. J.; Lu, C.; Wu, L.; Zhu, Y.; Herman, I. P., Anomalous photoluminescence Stokes shift in CdSe nanoparticle and carbon nanotube hybrids. *Phys Rev B* **2012,** *85* (4), 045404.
64. George, S. M., Atomic layer deposition: an overview. *Chem Rev* **2010,** *110* (1), 111-31.
65. Niinistö, J., Atomic layer deposition of high-k dielectrics from novel cyclopentadienyl-type precursors. **2006**.
66. Ritala, M.; Leskelä, M.; Nykänen, E.; Soininen, P.; Niinistö, L., Growth of titanium dioxide thin films by atomic layer epitaxy. *Thin Solid Films* **1993,** *225* (1-2), 288-295.
67. Yamada, A.; Sang, B.; Konagai, M., Atomic layer deposition of ZnO transparent conducting oxides. *Applied Surface Science* **1997,** *112*, 216-222.
68. Yousfi, E. B.; Fouache, J.; Lincot, D., Study of atomic layer epitaxy of zinc oxide by in-situ quartz crystal microgravimetry. *Applied surface science* **2000,** *153* (4), 223-234.
69. Kim, H., Atomic layer deposition of metal and nitride thin films: Current research efforts and applications for semiconductor device processing. *Journal of Vacuum Science & Technology B: Microelectronics and Nanometer Structures Processing, Measurement, and Phenomena* **2003,** *21* (6), 2231-2261.
70. Rossnagel, S.; Sherman, A.; Turner, F., Plasma-enhanced atomic layer deposition of Ta and Ti for interconnect diffusion barriers. *Journal of Vacuum Science & Technology B: Microelectronics and Nanometer Structures Processing, Measurement, and Phenomena* **2000,** *18* (4), 2016-2020.
71. Kim, H.; Cabral Jr, C.; Lavoie, C.; Rossnagel, S., Diffusion barrier properties of transition metal thin films grown by plasma-enhanced atomic-layer deposition. *Journal of Vacuum Science & Technology B: Microelectronics and Nanometer Structures Processing, Measurement, and Phenomena* **2002,** *20* (4), 1321-1326.
72. Coon, P.; Gupta, P.; Wise, M. L.; George, S., Adsorption and desorption kinetics for SiH2Cl2 on Si (111) 7× 7. *Journal of Vacuum Science & Technology A: Vacuum, Surfaces, and Films* **1992,** *10* (2), 324-333.
73. Sugahara, S.; Kadoshima, M.; Kitamura, T.; Imai, S.; Matsumura, M., Atomic hydrogen-assisted ALE of germanium. *Applied surface science* **1995,** *90* (3), 349-356.

74. Sugahara, S.; Uchida, Y.; Kitamura, T.; Nagai, T.; Matsuyama, M.; Hattori, T.; Matsumura, M., A proposed atomic-layer-deposition of germanium on Si surface. *Japanese journal of applied physics* **1997,** *36* (3S), 1609.
75. Puurunen, R. L., Surface chemistry of atomic layer deposition: A case study for the trimethylaluminum/water process. *J Appl Phys* **2005,** *97* (12), 9.
76. George, S.; Ott, A.; Klaus, J., Surface chemistry for atomic layer growth. *The Journal of Physical Chemistry* **1996,** *100* (31), 13121-13131.
77. Knoops, H. C.; Potts, S. E.; Bol, A. A.; Kessels, W., Atomic layer deposition. In *Handbook of crystal growth: thin films and epitaxy (second edition)*, Elsevier: 2015; pp 1101-1134.
78. Resch-Genger, U.; Grabolle, M.; Cavaliere-Jaricot, S.; Nitschke, R.; Nann, T., Quantum dots versus organic dyes as fluorescent labels. *Nat Methods* **2008,** *5* (9), 763-75.
79. Bruchez, M., Jr.; Moronne, M.; Gin, P.; Weiss, S.; Alivisatos, A. P., Semiconductor nanocrystals as fluorescent biological labels. *Science* **1998,** *281* (5385), 2013-6.
80. Yin, Y.; Alivisatos, A. P., Colloidal nanocrystal synthesis and the organic-inorganic interface. *Nature* **2005,** *437* (7059), 664-70.
81. Shirasaki, Y.; Supran, G. J.; Bawendi, M. G.; Bulovic, V., Emergence of colloidal quantum-dot light-emitting technologies. *Nat Photonics* **2013,** *7* (1), 13-23.
82. Qu, Q.; Zhang, P.; Wang, B.; Chen, Y.; Tian, S.; Wu, Y.; Holze, R., Electrochemical performance of MnO2 nanorods in neutral aqueous electrolytes as a cathode for asymmetric supercapacitors. *The Journal of Physical Chemistry C* **2009,** *113* (31), 14020-14027.
83. Shaw, S.; Colaux, J. L.; Hay, J. L.; Peiris, F. C.; Cademartiri, L., Building Materials from Colloidal Nanocrystal Arrays: Evolution of Structure, Composition, and Mechanical Properties upon the Removal of Ligands by O2 Plasma. *Advanced Materials* **2016,** *28* (40), 8900-8905.
84. De Wolf, S.; Holovsky, J.; Moon, S.-J.; Löper, P.; Niesen, B.; Ledinsky, M.; Haug, F.-J.; Yum, J.-H.; Ballif, C., Organometallic halide perovskites: sharp optical absorption edge and its relation to photovoltaic performance. *The journal of physical chemistry letters* **2014,** *5* (6), 1035-1039.
85. Irene, E., Applications of spectroscopic ellipsometry to microelectronics. *Thin Solid Films* **1993,** *233* (1-2), 96-111.
86. Li, K.; Wang, S.; Wang, L.; Yu, H.; Jing, N.; Xue, R.; Wang, Z., Fast and Sensitive Ellipsometry-Based Biosensing. *Sensors* **2018,** *18* (1), 15.
87. Morton, D. E.; Johs, B.; Hale, J. In *Optical monitoring of thin films using spectroscopic ellipsometry*, PROCEEDINGS OF THE ANNUAL TECHNICAL CONFERENCE-SOCIETY OF VACUUM COATERS, 2002; pp 299-305.
88. Azzam, R.; Bashara, N.; Burns, D. T., Ellipsometry and polarized light: North Holland, Amsterdam, 1987 (ISBN 0-444-87016-4). xvii+ 539 pp. Price Dfl. 75.00. Elsevier: 1987.
89. Silveirinha, M.; Engheta, N., Design of matched zero-index metamaterials using nonmagnetic inclusions in epsilon-near-zero media. *Phys Rev B* **2007,** *75* (7), 075119.
90. Alu, A.; Silveirinha, M. G.; Salandrino, A.; Engheta, N., Epsilon-near-zero metamaterials and electromagnetic sources: Tailoring the radiation phase pattern. *Phys Rev B* **2007,** *75* (15), 155410.
91. Li, Y.; Engheta, N., Supercoupling of surface waves with ε-near-zero metastructures. *Phys Rev B* **2014,** *90* (20), 201107.
92. Hajian, H.; Ozbay, E.; Caglayan, H., Beaming and enhanced transmission through a subwavelength aperture via epsilon-near-zero media. *Scientific Reports* **2017,** *7* (1), 4741.

93. Abbasi, F.; Engheta, N., Roles of epsilon-near-zero (ENZ) and mu-near-zero (MNZ) materials in optical metatronic circuit networks. *Optics Express* **2014,** *22* (21), 25109-25119.
94. Guo, Q.; Cui, Y.; Yao, Y.; Ye, Y.; Yang, Y.; Liu, X.; Zhang, S.; Liu, X.; Qiu, J.; Hosono, H., A Solution-Processed Ultrafast Optical Switch Based on a Nanostructured Epsilon-Near-Zero Medium. *Advanced Materials* **2017,** *29* (27), 1700754.
95. Pollard, R.; Murphy, A.; Hendren, W.; Evans, P.; Atkinson, R.; Wurtz, G.; Zayats, A.; Podolskiy, V. A., Optical nonlocalities and additional waves in epsilon-near-zero metamaterials. *Physical review letters* **2009,** *102* (12), 127405.
96. Caspani, L.; Kaipurath, R.; Clerici, M.; Ferrera, M.; Roger, T.; Kim, J.; Kinsey, N.; Pietrzyk, M.; Di Falco, A.; Shalaev, V. M., Enhanced nonlinear refractive index in ε-near-zero materials. *Physical review letters* **2016,** *116* (23), 233901.
97. Argyropoulos, C.; Chen, P.-Y.; D'Aguanno, G.; Engheta, N.; Alu, A., Boosting optical nonlinearities in ε-near-zero plasmonic channels. *Phys Rev B* **2012,** *85* (4), 045129.
98. Alam, M. Z.; De Leon, I.; Boyd, R. W., Large optical nonlinearity of indium tin oxide in its epsilon-near-zero region. *Science* **2016**, aae0330.
99. Rüter, C. E.; Makris, K. G.; El-Ganainy, R.; Christodoulides, D. N.; Segev, M.; Kip, D., Observation of parity–time symmetry in optics. *Nature physics* **2010,** *6* (3), 192.
100. Makris, K. G.; El-Ganainy, R.; Christodoulides, D.; Musslimani, Z. H., Beam dynamics in P T symmetric optical lattices. *Physical Review Letters* **2008,** *100* (10), 103904.
101. Marte, M. A.; Stenholm, S., Paraxial light and atom optics: the optical Schrödinger equation and beyond. *Physical Review A* **1997,** *56* (4), 2940.
102. Johnson, P. B.; Christy, R.-W., Optical constants of the noble metals. *Phys Rev B* **1972,** *6* (12), 4370.
103. Schwabl, F., *Advanced quantum mechanics*. Springer Science & Business Media: 2005.
104. Griffiths, D. J.; Schroeter, D. F., *Introduction to quantum mechanics*. Cambridge University Press: 2018.
105. Avrutsky, I.; Salakhutdinov, I.; Elser, J.; Podolskiy, V., Highly confined optical modes in nanoscale metal-dielectric multilayers. *Phys Rev B* **2007,** *75* (24), 241402.
106. Weil, T.; Vinter, B., Equivalence between resonant tunneling and sequential tunneling in double-barrier diodes. *Applied physics letters* **1987,** *50* (18), 1281-1283.
107. Ricco, B.; Azbel, M. Y., Physics of resonant tunneling. The one-dimensional double-barrier case. *Phys Rev B* **1984,** *29* (4), 1970.
108. Sollner, T.; Goodhue, W.; Tannenwald, P.; Parker, C.; Peck, D., Resonant tunneling through quantum wells at frequencies up to 2.5 THz. *Applied Physics Letters* **1983,** *43* (6), 588-590.
109. Chang, L. L.; Esaki, L.; Tsu, R., Resonant tunneling in semiconductor double barriers. *Applied Physics Letters* **1974,** *24* (12), 593-595.
110. Kittel, C.; McEuen, P.; McEuen, P., *Introduction to solid state physics*. Wiley New York: 1996; Vol. 8.
111. Cai, W.; Shalaev, V., *Optical metamaterials: fundamentals and applications*. Springer Science & Business Media: 2009.
112. Gao, W.; Li, X.; Bamba, M.; Kono, J., Continuous transition between weak and ultrastrong coupling through exceptional points in carbon nanotube microcavity exciton-polaritons. *Nat Photonics* **2018,** *12*, 362-367.

113. Törmä, P.; Barnes, W. L., Strong coupling between surface plasmon polaritons and emitters: a review. *Reports on Progress in Physics* **2014,** *78* (1), 013901.
114. Thompson, R.; Rempe, G.; Kimble, H., Observation of normal-mode splitting for an atom in an optical cavity. *Physical Review Letters* **1992,** *68* (8), 1132.
115. Kimble, H. J., Strong interactions of single atoms and photons in cavity QED. *Physica Scripta* **1998,** *1998* (T76), 127.
116. Savasta, S.; Saija, R.; Ridolfo, A.; Di Stefano, O.; Denti, P.; Borghese, F., Nanopolaritons: vacuum Rabi splitting with a single quantum dot in the center of a dimer nanoantenna. *ACS nano* **2010,** *4* (11), 6369-6376.
117. Gao, B.; Li, X.; Ma, Y.; Cao, Y.; Hu, Z.; Zhang, X.; Fu, J.; Huo, K.; Chu, P. K., MnO2–TiO2/C nanocomposite arrays for high-performance supercapacitor electrodes. *Thin Solid Films* **2015,** *584*, 61-65.
118. Bosman, S. J.; Gely, M. F.; Singh, V.; Bruno, A.; Bothner, D.; Steele, G. A., Multi-mode ultra-strong coupling in circuit quantum electrodynamics. *npj Quantum Information* **2017,** *3* (1), 46.
119. George, J.; Wang, S.; Chervy, T.; Canaguier-Durand, A.; Schaeffer, G.; Lehn, J.-M.; Hutchison, J. A.; Genet, C.; Ebbesen, T. W., Ultra-strong coupling of molecular materials: spectroscopy and dynamics. *Faraday discussions* **2015,** *178*, 281-294.
120. Todorov, Y.; Andrews, A. M.; Colombelli, R.; De Liberato, S.; Ciuti, C.; Klang, P.; Strasser, G.; Sirtori, C., Ultrastrong light-matter coupling regime with polariton dots. *Physical review letters* **2010,** *105* (19), 196402.
121. Rosi, N. L.; Mirkin, C. A., Nanostructures in biodiagnostics. *Chemical reviews* **2005,** *105* (4), 1547-1562.
122. Noginov, M.; Zhu, G.; Belgrave, A.; Bakker, R.; Shalaev, V.; Narimanov, E.; Stout, S.; Herz, E.; Suteewong, T.; Wiesner, U., Demonstration of a spaser-based nanolaser. *Nature* **2009,** *460* (7259), 1110.
123. Zhang, Q.; Li, G.; Liu, X.; Qian, F.; Li, Y.; Sum, T. C.; Lieber, C. M.; Xiong, Q., A room temperature low-threshold ultraviolet plasmonic nanolaser. *Nature communications* **2014,** *5*, 4953.
124. Jeantet, A.; Chassagneux, Y.; Raynaud, C.; Roussignol, P.; Lauret, J.-S.; Besga, B.; Estève, J.; Reichel, J.; Voisin, C., Widely tunable single-photon source from a carbon nanotube in the Purcell regime. *Physical review letters* **2016,** *116* (24), 247402.
125. Claudon, J.; Bleuse, J.; Malik, N. S.; Bazin, M.; Jaffrennou, P.; Gregersen, N.; Sauvan, C.; Lalanne, P.; Gérard, J.-M., A highly efficient single-photon source based on a quantum dot in a photonic nanowire. *Nat Photonics* **2010,** *4* (3), 174.
126. Somaschi, N.; Giesz, V.; De Santis, L.; Loredo, J.; Almeida, M. P.; Hornecker, G.; Portalupi, S. L.; Grange, T.; Antón, C.; Demory, J., Near-optimal single-photon sources in the solid state. *Nat Photonics* **2016,** *10* (5), 340.
127. Jacob, Z.; Smolyaninov, I. I.; Narimanov, E. E., Broadband Purcell effect: Radiative decay engineering with metamaterials. *Applied Physics Letters* **2012,** *100* (18), 181105.
128. Badolato, A.; Hennessy, K.; Atatüre, M.; Dreiser, J.; Hu, E.; Petroff, P. M.; Imamoğlu, A., Deterministic coupling of single quantum dots to single nanocavity modes. *Science* **2005,** *308* (5725), 1158-1161.

129. Wu, S.; Buckley, S.; Schaibley, J. R.; Feng, L.; Yan, J.; Mandrus, D. G.; Hatami, F.; Yao, W.; Vučković, J.; Majumdar, A., Monolayer semiconductor nanocavity lasers with ultralow thresholds. *Nature* **2015,** *520* (7545), 69.
130. Russell, K. J.; Liu, T.-L.; Cui, S.; Hu, E. L., Large spontaneous emission enhancement in plasmonic nanocavities. *Nat Photonics* **2012,** *6* (7), 459.
131. Lakowicz, J. R., Radiative decay engineering 3. Surface plasmon-coupled directional emission. *Analytical biochemistry* **2004,** *324* (2), 153-169.
132. Iorsh, I.; Poddubny, A.; Orlov, A.; Belov, P.; Kivshar, Y. S., Spontaneous emission enhancement in metal–dielectric metamaterials. *Physics Letters A* **2012,** *376* (3), 185-187.
133. Li, J.-F.; Li, C.-Y.; Aroca, R. F., Plasmon-enhanced fluorescence spectroscopy. *Chemical Society Reviews* **2017,** *46* (13), 3962-3979.
134. Li, L.; Wang, W.; Luk, T. S.; Yang, X.; Gao, J., Enhanced quantum dot spontaneous emission with multilayer metamaterial nanostructures. *ACS Photonics* **2017,** *4* (3), 501-508.
135. Nikitin, A. Y.; Guinea, F.; Garcia-Vidal, F. J.; Martin-Moreno, L., Surface plasmon enhanced absorption and suppressed transmission in periodic arrays of graphene ribbons. *Phys Rev B* **2012,** *85* (8), 081405.
136. Jin, Y.; Feng, J.; Zhang, X.-L.; Xu, M.; Bi, Y.-G.; Chen, Q.-D.; Wang, H.-Y.; Sun, H.-B., Surface-plasmon enhanced absorption in organic solar cells by employing a periodically corrugated metallic electrode. *Applied Physics Letters* **2012,** *101* (16), 163303.
137. Jiang, Y.; Wang, H.-Y.; Wang, H.; Gao, B.-R.; Hao, Y.-w.; Jin, Y.; Chen, Q.-D.; Sun, H.-B., Surface plasmon enhanced fluorescence of dye molecules on metal grating films. *The Journal of Physical Chemistry C* **2011,** *115* (25), 12636-12642.
138. Gryczynski, I.; Malicka, J.; Gryczynski, Z.; Lakowicz, J. R., Surface plasmon-coupled emission with gold films. *The Journal of Physical Chemistry B* **2004,** *108* (33), 12568-12574.
139. Bauch, M.; Toma, K.; Toma, M.; Zhang, Q.; Dostalek, J., Plasmon-enhanced fluorescence biosensors: a review. *Plasmonics* **2014,** *9* (4), 781-799.
140. Hsu, L.-Y.; Ding, W.; Schatz, G. C., Plasmon-coupled resonance energy transfer. *The journal of physical chemistry letters* **2017,** *8* (10), 2357-2367.
141. Liu, R.; Cheng, Q.; Hand, T.; Mock, J. J.; Cui, T. J.; Cummer, S. A.; Smith, D. R., Experimental demonstration of electromagnetic tunneling through an epsilon-near-zero metamaterial at microwave frequencies. *Physical review letters* **2008,** *100* (2), 023903.
142. Edwards, B.; Alù, A.; Young, M. E.; Silveirinha, M.; Engheta, N., Experimental verification of epsilon-near-zero metamaterial coupling and energy squeezing using a microwave waveguide. *Physical review letters* **2008,** *100* (3), 033903.
143. Engheta, N., Pursuing near-zero response. *Science* **2013,** *340* (6130), 286-287.
144. Protesescu, L.; Yakunin, S.; Bodnarchuk, M. I.; Krieg, F.; Caputo, R.; Hendon, C. H.; Yang, R. X.; Walsh, A.; Kovalenko, M. V., Nanocrystals of cesium lead halide perovskites (CsPbX3, X= Cl, Br, and I): novel optoelectronic materials showing bright emission with wide color gamut. *Nano Lett* **2015,** *15* (6), 3692-3696.
145. Akkerman, Q. A.; Motti, S. G.; Srimath Kandada, A. R.; Mosconi, E.; D'Innocenzo, V.; Bertoni, G.; Marras, S.; Kamino, B. A.; Miranda, L.; De Angelis, F., Solution synthesis approach to colloidal cesium lead halide perovskite nanoplatelets with monolayer-level thickness control. *Journal of the American Chemical Society* **2016,** *138* (3), 1010-1016.

146. Akkerman, Q. A.; D'Innocenzo, V.; Accornero, S.; Scarpellini, A.; Petrozza, A.; Prato, M.; Manna, L., Tuning the optical properties of cesium lead halide perovskite nanocrystals by anion exchange reactions. *Journal of the American Chemical Society* **2015,** *137* (32), 10276-10281.
147. Shamsi, J.; Rastogi, P.; Caligiuri, V.; Abdelhady, A. L.; Spirito, D.; Manna, L.; Krahne, R., Bright-Emitting Perovskite Films by Large-Scale Synthesis and Photoinduced Solid-State Transformation of CsPbBr3 Nanoplatelets. *ACS nano* **2017,** *11* (10), 10206-10213.
148. Du, X.; Wu, G.; Cheng, J.; Dang, H.; Ma, K.; Zhang, Y.-W.; Tan, P.-F.; Chen, S., High-quality CsPbBr 3 perovskite nanocrystals for quantum dot light-emitting diodes. *RSC Advances* **2017,** *7* (17), 10391-10396.
149. He, X.; Qiu, Y.; Yang, S., Fully-Inorganic Trihalide Perovskite Nanocrystals: A New Research Frontier of Optoelectronic Materials. *Advanced Materials* **2017,** *29* (32), 1700775.
150. West, P. R.; Kinsey, N.; Ferrera, M.; Kildishev, A. V.; Shalaev, V. M.; Boltasseva, A., Adiabatically tapered hyperbolic metamaterials for dispersion control of high-k waves. *Nano Lett* **2014,** *15* (1), 498-505.
151. Sreekanth, K. V.; De Luca, A.; Strangi, G., Experimental demonstration of surface and bulk plasmon polaritons in hypergratings. *Scientific reports* **2013,** *3*, 3291.
152. Poddubny, A.; Iorsh, I.; Belov, P.; Kivshar, Y., Hyperbolic metamaterials. *Nat Photonics* **2013,** *7* (12), 948.
153. Shekhar, P.; Atkinson, J.; Jacob, Z., Hyperbolic metamaterials: fundamentals and applications. *Nano convergence* **2014,** *1* (1), 14.
154. Drachev, V. P.; Podolskiy, V. A.; Kildishev, A. V., Hyperbolic metamaterials: new physics behind a classical problem. *Optics express* **2013,** *21* (12), 15048-15064.
155. Ferrari, L.; Wu, C.; Lepage, D.; Zhang, X.; Liu, Z., Hyperbolic metamaterials and their applications. *Progress in Quantum Electronics* **2015,** *40*, 1-40.
156. Chandrasekar, R.; Wang, Z.; Meng, X.; Azzam, S. I.; Shalaginov, M. Y.; Lagutchev, A.; Kim, Y. L.; Wei, A.; Kildishev, A. V.; Boltasseva, A., Lasing action with gold nanorod hyperbolic metamaterials. *ACS Photonics* **2017,** *4* (3), 674-680.
157. Shi, J.; Liu, B.; Li, P.; Ng, L. Y.; Shen, S., Near-field energy extraction with hyperbolic metamaterials. *Nano Lett* **2015,** *15* (2), 1217-1221.
158. Cortes, C.; Newman, W.; Molesky, S.; Jacob, Z., Quantum nanophotonics using hyperbolic metamaterials. *Journal of Optics* **2012,** *14* (6), 063001.
159. Caligiuri, V.; De Luca, A., Metal-semiconductor-oxide extreme hyperbolic metamaterials for selectable canalization wavelength. *Journal of Physics D: Applied Physics* **2016,** *49* (8), 08LT01.
160. Caligiuri, V.; Dhama, R.; Sreekanth, K.; Strangi, G.; De Luca, A., Dielectric singularity in hyperbolic metamaterials: the inversion point of coexisting anisotropies. *Scientific reports* **2016,** *6*, 20002.
161. Caligiuri, V.; Pezzi, L.; Veltri, A.; De Luca, A., Resonant gain singularities in 1D and 3D metal/dielectric multilayered nanostructures. *ACS nano* **2016,** *11* (1), 1012-1025.
162. Prodan, E.; Nordlander, P., Structural tunability of the plasmon resonances in metallic nanoshells. *Nano Lett* **2003,** *3* (4), 543-547.
163. Prodan, E.; Nordlander, P., Plasmon hybridization in spherical nanoparticles. *The Journal of chemical physics* **2004,** *120* (11), 5444-5454.
164. Prodan, E.; Radloff, C.; Halas, N. J.; Nordlander, P., A hybridization model for the plasmon response of complex nanostructures. *science* **2003,** *302* (5644), 419-422.

165. Javani, M. H.; Stockman, M. I., Real and imaginary properties of epsilon-near-zero materials. *Physical review letters* **2016,** *117* (10), 107404.
166. Fleury, R.; Alu, A., Enhanced superradiance in epsilon-near-zero plasmonic channels. *Phys Rev B* **2013,** *87* (20), 201101.
167. Krishnamoorthy, H. N.; Jacob, Z.; Narimanov, E.; Kretzschmar, I.; Menon, V. M., Topological transitions in metamaterials. *Science* **2012,** *336* (6078), 205-209.
168. Hoang, T. B.; Akselrod, G. M.; Argyropoulos, C.; Huang, J.; Smith, D. R.; Mikkelsen, M. H., Ultrafast spontaneous emission source using plasmonic nanoantennas. *Nature communications* **2015,** *6*, 7788.
169. Akselrod, G. M.; Argyropoulos, C.; Hoang, T. B.; Ciracì, C.; Fang, C.; Huang, J.; Smith, D. R.; Mikkelsen, M. H., Probing the mechanisms of large Purcell enhancement in plasmonic nanoantennas. *Nat Photonics* **2014,** *8* (11), 835.
170. Reiss, P.; Protiere, M.; Li, L., Core/Shell Semiconductor Nanocrystats. *Small* **2009,** *5* (2), 154-168.
171. Dabbousi, B. O.; RodriguezViejo, J.; Mikulec, F. V.; Heine, J. R.; Mattoussi, H.; Ober, R.; Jensen, K. F.; Bawendi, M. G., (CdSe)ZnS core-shell quantum dots: Synthesis and characterization of a size series of highly luminescent nanocrystallites. *J. Phys. Chem. B* **1997,** *101* (46), 9463-9475.
172. Peng, X. G.; Schlamp, M. C.; Kadavanich, A. V.; Alivisatos, A. P., Epitaxial growth of highly luminescent CdSe/CdS core/shell nanocrystals with photostability and electronic accessibility. *J. Am. Chem. Soc.* **1997,** *119* (30), 7019-7029.
173. Talapin, D. V.; Koeppe, R.; Gotzinger, S.; Kornowski, A.; Lupton, J. M.; Rogach, A. L.; Benson, O.; Feldmann, J.; Weller, H., Highly emissive colloidal CdSe/CdS heterostructures of mixed dimensionality. *Nano Lett.* **2003,** *3* (12), 1677-1681.
174. Carbone, L.; Nobile, C.; De Giorgi, M.; Sala, F. D.; Morello, G.; Pompa, P.; Hytch, M.; Snoeck, E.; Fiore, A.; Franchini, I. R.; Nadasan, M.; Silvestre, A. F.; Chiodo, L.; Kudera, S.; Cingolani, R.; Krahne, R.; Manna, L., Synthesis and micrometer-scale assembly of colloidal CdSe/CdS nanorods prepared by a seeded growth approach. *Nano Lett.* **2007,** *7* (10), 2942-2950.
175. Jain, A.; Voznyy, O.; Hoogland, S.; Korkusinski, M.; Hawrylak, P.; Sargent, E. H., Atomistic Design of CdSe/CdS Core–Shell Quantum Dots with Suppressed Auger Recombination. *Nano Lett.* **2016,** *16* (10), 6491-6496.
176. Stouwdam, J. W.; Shan, J.; van Veggel, F. C. J. M.; Pattantyus-Abraham, A. G.; Young, J. F.; Raudsepp, M., Photostability of colloidal PbSe and PbSe/PbS core/shell nanocrystals in solution and in the solid state. *J Phys Chem C* **2007,** *111* (3), 1086-1092.
177. Talapin, D. V.; Lee, J. S.; Kovalenko, M. V.; Shevchenko, E. V., Prospects of colloidal nanocrystals for electronic and optoelectronic applications. *Chem Rev* **2010,** *110* (1), 389-458.
178. Solomeshch, O.; Tessler, N., Research Update: Preserving the photoluminescence efficiency of near infrared emitting nanocrystals when embedded in a polymer matrix. *Apl Mater* **2016,** *4* (4).
179. Ma, Y. S.; Zhang, B. B.; Gu, M.; Huang, S. M.; Liu, X. L.; Liu, B.; Ni, C., Bulk synthesis of homogeneous and transparent bulk core/multishell quantum dots/PMMA nanocomposites with bright luminescence. *J Appl Polym Sci* **2013,** *130* (3), 1548-1553.
180. Pang, L.; Shen, Y.; Tetz, K.; Fainman, Y., PMMA quantum dots composites fabricated via use of pre-polymerization. *Opt Express* **2005,** *13* (1), 44-9.

181. Puurunen, R. L., Reply to "Comment on 'Analysis of hydroxyl group controlled atomic layer deposition of hafnium oxide from hafnium tetrachloride and water" ' [J. Appl. Phys. 95, 4777 (2004)]. *J Appl Phys* **2005,** *98* (1).
182. Liu, Y.; Gibbs, M.; Perkins, C. L.; Tolentino, J.; Zarghami, M. H.; Bustamante, J.; Law, M., Robust, Functional Nanocrystal Solids by Infilling with Atomic Layer Deposition. *Nano Lett* **2011,** *11* (12), 5349-5355.
183. Lambert, K.; Dendooven, J.; Detavernier, C.; Hens, Z., Embedding quantum dot monolayers in Al2O3 using atomic layer deposition. *Chem. Mater.* **2010,** *23* (2), 126-128.
184. Thimsen, E.; Johnson, M.; Zhang, X.; Wagner, A. J.; Mkhoyan, K. A.; Kortshagen, U. R.; Aydil, E. S., High electron mobility in thin films formed via supersonic impact deposition of nanocrystals synthesized in nonthermal plasmas. *Nat Commun* **2014,** *5*, 5822.
185. Cheng, C. Y.; Mao, M. H., Photo-stability and time-resolved photoluminescence study of colloidal CdSe/ZnS quantum dots passivated in Al2O3 using atomic layer deposition. *J Appl Phys* **2016,** *120* (8).
186. Pourret, A.; Guyot-Sionnest, P.; Elam, J. W., Atomic Layer Deposition of ZnO in Quantum Dot Thin Films. *Advanced Materials* **2009,** *21* (2), 232-235.
187. Chanyawadee, S.; Lagoudakis, P. G.; Harley, R. T.; Charlton, M. D. B.; Talapin, D. V.; Huang, H. W.; Lin, C. H., Increased color-conversion efficiency in hybrid light-emitting diodes utilizing non-radiative energy transfer. *Advanced Materials* **2010,** *22* (5), 602-606.
188. Di Stasio, F.; Grim, J. Q.; Lesnyak, V.; Rastogi, P.; Manna, L.; Moreels, I.; Krahne, R., Single-Mode Lasing from Colloidal Water-Soluble CdSe/CdS Quantum Dot-in-Rods. *Small* **2015,** *11* (11), 1328-1334.
189. Di Stasio, F.; Polovitsyn, A.; Angeloni, I.; Moreels, I.; Krahne, R., Broadband Amplified Spontaneous Emission and Random Lasing from Wurtzite CdSe/CdS “Giant-Shell” Nanocrystals. *ACS Photonics* **2016,** *3* (11), 2083-2088.
190. Zavelani-Rossi, M.; Krahne, R.; Della Valle, G.; Longhi, S.; Franchini, I. R.; Girardo, S.; Scotognella, F.; Pisignano, D.; Manna, L.; Lanzani, G.; Tassone, F., Self-assembled CdSe/CdS nanorod micro-lasers fabricated from solution by capillary jet deposition. *Laser & Photonics Reviews* **2012,** *6* (5), 678-683.
191. Pal, B. N.; Ghosh, Y.; Brovelli, S.; Laocharoensuk, R.; Klimov, V. I.; Hollingsworth, J. A.; Htoon, H., ‘Giant’ CdSe/CdS Core/Shell Nanocrystal Quantum Dots As Efficient Electroluminescent Materials: Strong Influence of Shell Thickness on Light-Emitting Diode Performance. *Nano Lett.* **2012,** *12* (1), 331-336.
192. Rastogi, P.; Palazon, F.; Prato, M.; Di Stasio, F.; Krahne, R., Enhancing the Performance of CdSe/CdS Dot-in-Rod Light-Emitting Diodes via Surface Ligand Modification. *ACS Appl. Mater. Interfaces* **2018,** *10* (6), 5665-5672.
193. Castelli, A.; Meinardi, F.; Pasini, M.; Galeotti, F.; Pinchetti, V.; Lorenzon, M.; Manna, L.; Moreels, I.; Giovanella, U.; Brovelli, S., High-Efficiency All-Solution-Processed Light-Emitting Diodes Based on Anisotropic Colloidal Heterostructures with Polar Polymer Injecting Layers. *Nano Lett.* **2015,** *15* (8), 5455-5464.
194. Donega, C. d. M., Synthesis and properties of colloidal heteronanocrystals. *Chem. Soc. Rev.* **2011,** *40* (3), 1512-1546.
195. Krahne, R.; Morello, G.; Figuerola, A.; George, C.; Deka, S.; Manna, L., Physical properties of elongated inorganic nanoparticles. *Phys. Rep.* **2011,** *501* (3), 75-221.

196. Jellison Jr, G.; Modine, F., Parameterization of the optical functions of amorphous materials in the interband region. *Applied Physics Letters* **1996,** *69* (3), 371-373.
197. Lakowicz, J. R., *Principles of Fluorescence Spectroscopy*. Springer: US, 2006.
198. Coropceanu, I.; Rossinelli, A.; Caram, J. R.; Freyria, F. S.; Bawendi, M. G., Slow-Injection Growth of Seeded CdSe/CdS Nanorods with Unity Fluorescence Quantum Yield and Complete Shell to Core Energy Transfer. *ACS Nano* **2016,** *10* (3), 3295-3301.
199. Zhao, Y.; Riemersma, C.; Pietra, F.; Koole, R.; de Mello Donegá, C.; Meijerink, A., High-temperature luminescence quenching of colloidal quantum dots. *ACS Nano* **2012,** *6* (10), 9058-9067.
200. Diroll, B. T.; Murray, C. B., High-temperature photoluminescence of CdSe/CdS core/shell nanoheterostructures. *ACS Nano* **2014,** *8* (6), 6466-6474.
201. Rowland, C. E.; Liu, W.; Hannah, D. C.; Chan, M. K.; Talapin, D. V.; Schaller, R. D., Thermal stability of colloidal InP nanocrystals: small inorganic ligands boost high-temperature photoluminescence. *ACS Nano* **2013,** *8* (1), 977-985.
202. Howder, C. R.; Long, B. A.; Bell, D. M.; Furakawa, K. H.; Johnson, R. C.; Fang, Z.; Anderson, S. L., Photoluminescence of charged CdSe/ZnS quantum dots in the gas phase: Effects of charge and heating on absorption and emission probabilities. *ACS Nano* **2014,** *8* (12), 12534-12548.
203. Cai, X.; Martin, J. E.; Shea-Rohwer, L. E.; Gong, K.; Kelley, D. F., Thermal quenching mechanisms in II–VI semiconductor nanocrystals. *The Journal of Physical Chemistry C* **2013,** *117* (15), 7902-7913.
204. Gruber, C.; Trügler, A.; Hohenau, A.; Hohenester, U.; Krenn, J. R., Spectral modifications and polarization dependent coupling in tailored assemblies of quantum dots and plasmonic nanowires. *Nano Lett* **2013,** *13* (9), 4257-4262.
205. Zhou, N.; Yuan, M.; Gao, Y.; Li, D.; Yang, D., Silver nanoshell plasmonically controlled emission of semiconductor quantum dots in the strong coupling regime. *ACS nano* **2016,** *10* (4), 4154-4163.
206. Wersäll, M.; Cuadra, J.; Antosiewicz, T. J.; Balci, S.; Shegai, T., Observation of mode splitting in photoluminescence of individual plasmonic nanoparticles strongly coupled to molecular excitons. *Nano Lett* **2016,** *17* (1), 551-558.
207. Repetto, D.; Giordano, M. C.; Foti, A.; Gucciardi, P. G.; Mennucci, C.; de Mongeot, F. B., SERS amplification by ultra-dense plasmonic arrays on self-organized PDMS templates. *Applied Surface Science* **2018,** *446*, 83-91.